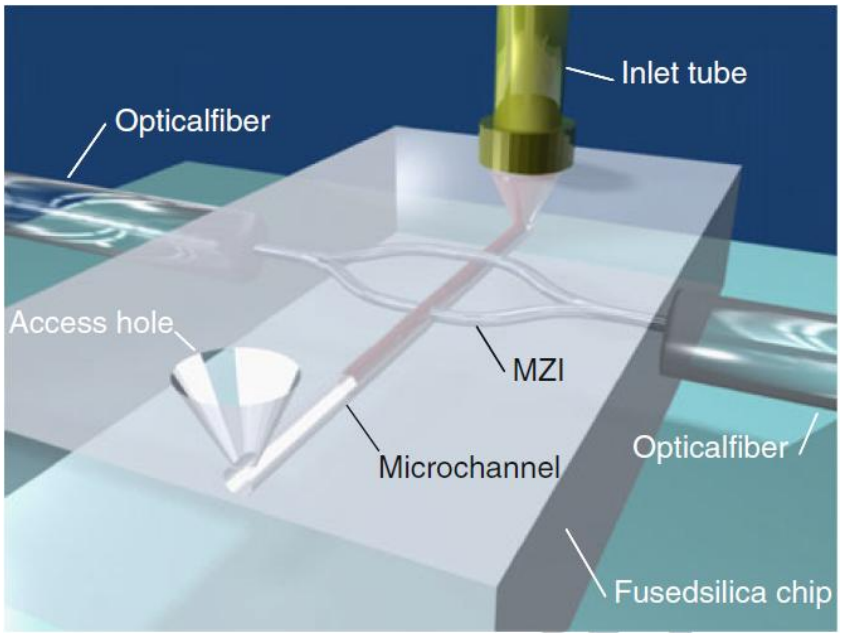

FemtoEtch – Femtosecond Laser Micromachining and Applications in Microfluidics and Optofluidics

João Miguel Mendes da Silva Maia
Mestrado em Engenharia Física
Departamento de Física e Astronomia
2016

Orientador
Paulo Vicente da Silva Marques, Professor Auxiliar
Departamento de Física e Astronomia
Faculdade de Ciências da Universidade do Porto

Todas as correções determinadas pelo júri, e só essas, foram efetuadas.

O Presidente do Júri,

Porto, _____/_____/_____

Acknowledgments

I would like to express my sincere thanks to all who somehow helped me pursuing a Master's Degree in Physics Engineering, in particular:

To my supervisor Dr. Paulo Marques for the opportunity given to carry out this project and for all the support and guidance during this past year.

To Dr. Daniel Alexandre for sharing his experience in femtosecond laser microfabrication and for his help in writing the software.

To Dr. António Pereira Leite for his lectures in electromagnetism and in optics that motivated me to pursue research in this area, and for all the wise advices given throughout this project.

To my professors at University of Porto for sharing their scientifical knowledge and experience with me.

To all my colleagues and friends for the great moments throughout these five years.

To the most important people in my life, my parents and my brother, for always being there for me.

Abstract

Lab-on-a-chip systems integrate microfluidic channels to transport, mix, make react and analyze small volumes of samples. These devices are usually manufactured by soft lithography, however femtosecond laser direct writing adds new advantages such as three-dimensional fabrication and on-chip optical detection. Therefore, this fabrication technique allows the implementation of monolithic optofluidic devices.

The laser interaction with glass materials alters the material properties around the focal volume by increasing the refractive index and etching selectivity in hydrofluoric acid. The first effect allows fabrication of low-loss waveguides, Bragg grating waveguides and directional couplers, among other devices. Irradiation of the sample also promotes an anisotropic etching reaction that is exploited to fabricate channels inside the glass.

The former regime was employed to fabricate microfluidic channels in fused silica. During the thesis the fabrication procedure was optimized in order to obtain centimeter long channels with uniform aspect ratio and with crack-free smooth walls.

From this study, we were able to demonstrate integration of optical and fluidic components and test two optical detection schemes. The first consists of a Bragg grating waveguide placed a few microns from the microfluidic channel, enabling evanescent coupling and measurement of refractive index and temperature. In the second reported scheme, low-loss waveguides cross the microfluidic channel enabling manipulation and detection of particles present in the fluid.

The presented fabrication technique was also employed to micromachine fibers, aiming to obtain fiber-based sensors.

The results obtained during this project set the foundations for the development of new optofluidic devices.

Resumo

Sistemas *lab-on-a-chip* são compostos por canais de microfluídica que permitem transportar, misturar, fazer reagir e analisar pequenos volumes de reagentes. Estes dispositivos são fabricados tipicamente por *soft lithography*, contudo escrita direta com laser femtosegundo traz novas vantagens como fabricação tridimensional e integração de sistemas de deteção ótica no chip. Assim, esta técnica de fabricação permite implementação monolítica de dispositivos de optofluídica.

A interação entre o feixe laser e o vidro altera as propriedades do material em torno do volume focal, através do aumento do índice de refração e da seletividade para *etching* em ácido hidrofluorídrico. O primeiro efeito permite fabricação de guias óticos, redes de Bragg e acopladores direcionais, entre outros. A irradiação da amostra também promove uma reação de *etching* anisotrópica que permite a fabricação de canais no interior do substrato.

O efeito anterior foi utilizado para fabricar de canais de microfluídica em sílica fundida. Durante este projeto, o processo de fabricação foi optimizado para obter canais longos com vários centímetros de comprimento, com *aspect ratio* uniforme e com paredes suaves e sem fraturas.

A partir deste estudo, foi possível integrar componentes óticos com sistemas de fluídica e testar dois esquemas de deteção ótica. O primeiro esquema consiste na fabricação de redes de Bragg colocadas a poucos micrómetros do canal de microfluídica, permitindo acoplamento evanescente e medição do índice de refração e da temperatura. No segundo esquema, guias óticos são desenhados de forma a cruzarem o canal de microfluídica, o que permite manipulação e deteção de partículas presentes no canal.

A técnica de fabricação apresentada foi também empregue na micromaquinação de fibras óticas, com o objetivo de produzir sensores em fibra.

Os resultados obtidos neste projeto constituem o primeiro passo para o desenvolvimento de novos dispositivos de optofluídica.

Keywords

Microfluidics, Optofluidics, Biosensors, Femtosecond Laser Direct Writing, Micromachining, Chemical Etching, Fused Silica, Etch Rate, Surface Roughness.

Contents

List of Figures

List of Tables

Acronyms

2D – Two-dimensional
2PP – Two-photon Polymerization
3D – Three-dimensional
AFM – Atomic Force Microscopy
BGW – Bragg Grating Waveguide
CCD – Charge-coupled Device
CPA – Chirped Pulse Amplification
CW – Continuous Wave
FLICE – Femtosecond Laser Irradiation followed by Chemical Etching
HF – Hydrofluoric Acid
KOH – Potassium Hydroxide
LOC – Lab-on-a-chip
OSA – Optical Spectrum Analyzer
PCF – Photonic Crystal Fiber
PDMS – Polydimethylsiloxane
PMMA – Polymethylmethacrylate
SEM – Scanning Electron Microscopy
SERS – Surface Enhanced Raman Spectroscopy
SMF – Single Mode Fiber
TPA – Two-photon Absorption
UV – Ultraviolet

Chapter 1

Introduction

The concept of lab-on-a-chip (LOC) revolves around the idea of miniaturizing a complete laboratory into a hand-sized chip, that allows preparation, transport, reaction and analysis of reagents [1]. Compared to commonly employed analysis schemes, where sample handling, long analysis time and high consumption of samples is still a problem, LOC technology promises to alleviate these issues while maintaining high efficiency, accuracy and performance [2]. Therefore, these devices are rapidly becoming fundamental tools in many applications, ranging from industrial processing to medical and biochemical analysis [3].

Currently, fabrication of microfluidic devices is accomplished by conventional fabrication techniques, such as photolithography and soft lithography [4, 5]. These devices may still be integrated with mechanical elements (valves and mixers for control of reagent flow and reaction [6, 7]) and optical elements (mirrors, lenses and waveguides for in situ analysis of reactants [8]), increasing device functionalities and enhancing its performance towards point-of-care, portable and multianalyte sensing systems [9].

Despite the success photolithography and soft lithography have achieved, both techniques come short in two key aspects. First, both techniques are planar, hindering fabrication of three-dimensional (3D) microstructures in a single step [10]. Second, optical detection schemes used with existent LOC systems require bulk elements such as lenses, mirrors and microscope objectives to focus and collect light [11]. These schemes frustrate most of the LOC advantages by increasing alignment demands, limiting device portability and preventing point-of-care applications. Hence much of the success of the LOC concept depends on the ability of integrating optical detection schemes in the chip device. Conventional fabrication techniques hamper this integration and thus, the pursuit for a technology that enables combination of fluidic, mechanical and optical components in the same platform is still an active research area.

Recently, femtosecond laser direct writing has become a promising approach for fabrication of embedded 3D microstructures, since the femtosecond laser can internally modify transparent materials by a multiphoton absorption process, with submicron resolution [12]. Laser direct writing has been shown to induce two different kinds of modification in materials transparent to the laser wavelength, which are important for LOC device fabrication [13]. First, it induces a refractive index modification enabling fabrication of waveguides, gratings and couplers [14, 15]. Second, it allows for selective etching as demonstrated by Marcinkevicius et al [16], enabling production of microfluidic channels. These two effects may be combined to produce optofluidic

devices [17, 18], where the flexibility of this technology brings significant advantages in terms of rapid prototyping and customization.

Although the previous method allows integration of both optical and fluidic elements, some issues regarding sample/reagent detection still stand. As the size of the microfluidic systems decrease, so does the detection volume, usually in the range of 10^{-9} to 10^{-12} liters [11]. In addition the devices present a high surface-to-volume ratio, where surface forces (surface tension, van der Waals and surface roughness) become dominant [19, 20]. Thus, to produce an highly sensitive optofluidic system, fine and accurate control of the fabrication process is needed.

The microfluidic channel is the backbone of many applications, including sample injection, flow control, mixing, reaction and analysis. Therefore, the main goal of this thesis is to study the fabrication process of microfluidic channels using femtosecond laser micromachining, so that the produced channels can be used in optofluidic applications. This study is done by optimizing two parameters (etch rate and surface roughness) as a function of the exposure conditions. The etch rate defines the maximum aspect ratio (length vs cross-section dimension) and length of the microfluidic channels, while surface roughness disturbs fluid flow and light coupling to the channel. From this study it is expected to produce channels with smooth sidewalls and uniform aspect ratio so that they can be integrated with single waveguides or Bragg grating waveguides, thus enabling optical sensing.

This thesis is divided in five chapters, which are summarized here. After this introduction, chapter 2 presents a background review of commonly used materials and the most widely used technologies for fabricating LOC devices. The majority of the chapter focuses on femtosecond laser based techniques, therefore it is also discussed the generation of ultrashort pulses and their interaction with matter.

Chapter 3 presents the femtosecond laser writing system, discussing in full detail the function of each component and the system alignment procedure. The writing and etching techniques employed to produce optical components and microfluidic channels are also reviewed. Lastly, we present the characterization set-up of optical components and the optimum conditions to fabricate low-loss waveguides and Bragg grating waveguides.

Chapter 4 focuses on the results obtained during the thesis regarding optimization of the fabrication process of microfluidic channels. Preliminary work on the integration of optical layers with fluidic channels and on the fabrication of cavities in optical fibers is also presented. The main results achieved are summarized in chapter 5, where future work based on the presented conclusions is also proposed.

Chapter 2

Theoretical Review

This chapter provides a bibliographic review about the most commonly employed materials and fabrication techniques of microfluidic and optofluidic devices.

In choosing the material, one has to consider its surface chemistry and its optical transparency. Surface modification and fluid handling is controlled by the surface properties, while the detection scheme is determined by its optical properties. The most widely used materials are silicon, polymers and glass. Silicon and polymers are associated with two well-established planar techniques, photolithography and soft lithography (molding), respectively; while glass is associated with etching processes and laser micromachining. In short, the lithography techniques are mostly employed for fabrication of pure microfluidic devices, while femtosecond laser technologies allow for integration of optical functionalities in the microfluidic chip and fabrication of 3D embedded structures.

A review on the generation of ultrashort pulses and on its interaction with matter is also presented: femtosecond laser can internally modify the glass local properties due to multiphoton absorption or even ablate glass, and can polymerize photosensitive polymers/resins. Based on these interactions, three different technologies are introduced: Femtosecond Laser Irradiation followed by Chemical Etching (FLICE), two-photon polymerization (2PP) and ablation.

2.1 Materials

2.1.1 Silicon

Silicon was the first material used for microfluidic applications due to its central role in integrated circuit technology, where device fabrication is done by photolithography. The existent technology enables integration of different components such as microelectrodes, photodetectors and ion-sensitive field effect transistors in silicon [21].

This material, however, is electrically semiconducting and optically opaque in the visible and ultraviolet spectrum which is the detection wavelength range used in bioanalysis; hence disabling many on-chip detection and analysis schemes [2]. In addition, it is bio- and chemically incompatible, making it unsuitable for many applications.

These issues have been surpassed by researching new materials, like polymers and glasses, as platforms for LOC devices [2].

2.1.2 Polymers

The most common used polymers for LOC fabrication are polymethylmethacrylate (PMMA), photoresist SU8 and polydimethylsiloxane (PDMS) [22]. Techniques based on replication, such as soft lithography, are used to fabricate devices in these materials, which are cheaper and faster than the techniques used when processing glass and silicon and are highly reproducible.

In general, polymers are low cost and compatible for biological and chemical applications [19]. They are also less fragile than glass and silicon and enable a larger fabrication yield, which is an important factor for mass production. Polymers are also attractive due to the ease with which dopants can be incorporated into them. However, they have poor thermal conductivity which can lead to Joule heating, are often difficult to clean, are not reusable due to their porous nature, and are incompatible with several organic solvents, particularly non-polar solvents. In addition, polymers have higher optical transmission losses and inferior chemical durability than glass.

PDMS

Microfluidic networks can be fabricated by soft-lithography in PDMS, which possesses several properties that are instrumental in the formation of high-quality structures [19].

First, PDMS is a durable elastomer with tunable Young modulus and low surface energy, which deforms and conforms, with minimal applied pressure, to the surface of non-planar substrates over a relatively large area [23]. The elastic characteristic of PDMS also allow it to be released easily and to be replicated. Second, PDMS is chemically inert and compatible with the majority of organic polar solvents. Third, it is homogeneous, isotropic, and optically transparent from 240nm to 1100nm with low birefringence, therefore highly attractive for optofluidic applications. It is also a thermal and electrical insulator. Fourth, the surface properties of PDMS can be readily modified by treatment with plasma to give appropriate interfacial interactions with materials [19]. In particular treatment with oxygen plasma turns its surface hydrophilic and reactive, such that it forms strong bonds with the sealing substrate.

However, this polymer swells in the presence of organic non-polar solvents, requiring surface treatment to avoid such effect. Its elastomeric character is also the origin of some technical problems: gravity, adhesion and capillary forces exert stress on the elastomeric features and cause them to collapse and generate defects in the pattern that is formed [23]. In addition, PDMS shrinks by a factor of about 1% upon curing, thus it is not the best material for production of high aspect-ratio structures. Commercially available PDMS also contains nanoparticles of silica that introduce unwanted scattering of light, hampering fabrication of low-loss waveguides.

PMMA and photoresist SU8

PMMA based devices may be fabricated either by replication of a 3D image engraved on a silicon wafer or by laser direct writing. PMMA is one of the few polymers that can be processed by laser writing, which brings some advantages over glass, in particular it is machined at lower intensities [24]. Ring-mode and single-waveguides have been laser written in PMMA, but the transmission losses are higher than those achieved in glass.

Photoresist SU8 has been used to create multilayered structures based on photolithography and successive bonding and releasing steps. This material may also serve as a platform for stereolithography and/or polymerization, enabling formation of 3D structures.

2.1.3 Glasses

LOC systems may also be made in silica and other photosensitive glasses, such as Foturan. Other glasses such as borosilicate glass BK7 or rare-earth doped glasses have also been studied for fabrication of optical components.

Glasses are more difficult to process compared with polymers, but have some advantages over these materials [25].

First, they are non-porous, stable in time, amorphous and have a high Young modulus. They are chemically inert to most solvents and are biocompatible. Their surface has high wettability and its chemistry is hydrophilic and appropriate for electro-osmotic flow. Optically, they are transparent in the visible and ultraviolet spectrum, have low fluorescence and low non-linearity. These properties enable detection and analysis of biological samples. Glasses also have low thermal expansion and high thermal conductivity, making them suitable for electrokinetics. They also maintain high performance from less than -100°C to over 500°C [21].

Fabrication of devices in these materials is usually carried by either photolithography and etching and, more recently, by femtosecond laser micromachining. They may also be used in processes such as selective metallization. Selectively metalized structures can be used for applications such as optical modulation and electrofluidics, surface enhanced Raman spectroscopy (SERS) and plasmonics [26]. In addition, glass may serve as a platform for two-photon polymerization, where functional 3D polymeric microcomponents are formed at the glass surface.

Fused Silica

Fused silica glass has an additional advantage: it has been used extensively in the optoelectronic industry, due to its optical characteristics. This material has high transmission from ultraviolet to infrared and low optical non-linearity, low background fluorescence and dispersion.

Well established microfabrication processes based on photolithography and wet/dry etching are also available for this glass. Fused silica is also transparent to the laser wavelengths typically available from ultrafast lasers and thus meets the criteria for nonlinear absorption process [10]. Therefore, LOC devices may also be fabricated in this material by laser direct writing.

Fused silica is also chemically and thermally stable and durable, and can be doped with other materials such as germanium, boron and rare earths. Although it is dissolved by hydrofluoric acid and hot potassium hydroxide, this feature provides an opportunity for the fabrication of microfluidic systems.

Foturan Glass

One of the most successful photosensitive glasses for the fabrication of LOC systems is Foturan glass. It is a lithium aluminosilicate glass doped with trace amounts of silver and cerium ions [10]. This glass has a large Young modulus, a low absorption coefficient in the visible range, and good chemical stability and biocompatibility, which are attractive for fabrication of biosensors.

Usually, Foturan based systems are fabricated by ultraviolet (UV) exposure. However, the production of 3D devices is only achieved by femtosecond laser writing, in a technique similar to the one used in fused silica, as shown by Kondo et al [27].

Borosilicate and Rare-earth doped glass

Other kinds of glasses have also been used to produce photonic components by laser direct writing [28].

Borosilicate glass, for example, has shown great potential for the production of low-loss waveguides by exhibiting thermal accumulation effects with moderate repetition rates of hundreds of kilohertz. Such heat accumulation effects have not been advantageously demonstrated in femtosecond laser writing of waveguides in fused silica. This material has been tested as platform for microfluidic channels, however etching selectivity still is not high enough to make this material more attractive than fused silica [29].

Rare earth doped glasses have been explored for direct fabrication of cavities.

2.1.4 Optical Fibers

Fabrication of sensors may also be conducted in optical fibers [30], where their availability and flexibility provides the perfect platform for distributed sensing. Optical fibers are also immune to electromagnetic fields, are biocompatible and chemically inert.

Standard single mode fibers (SMF) have a silica core doped with germanium, which increases the refractive index relatively to the background fused silica cladding. These fibers are commonly used on optical communication systems [31]. Their doped core is photosensitive to UV radiation and femtosecond laser wavelengths, which has been used to fabricate Bragg gratings and cavities for sensing applications.

Besides SMF, photonic crystal fibers (PCF) may also be exposed to a femtosecond laser, allowing fabrication of lab-on-a-fiber systems [32].

2.2 Traditional fabrication techniques

2.2.1 Photolithography

These technologies – photolithography and wet/dry etching – evolved from microelectronics and semiconductor industries, having been used to fabricate the first LOC systems [21].

Photolithography is a multi-step technique involving pattern transfer from a mask onto a layer of photoresist followed by wet or dry etching [33].

In short, a glass substrate – usually silicon – is spin-coated with a positive or negative photoresist. After pre-baking, the substrate is exposed to ultraviolet radiation through a photomask; and by development the photomask pattern is transferred to the sample surface. Given that fabrication of photomasks is expensive, recently some groups have designed the features on AutoCAD and printed it directly on polymeric transparent sheets. Despite being fabricated faster, these photomasks are not as durable and stable as standard photomasks. Direct laser writing may also be employed to polymerize the photoresist and produce relief structures.

The sample is then immersed in a developer which removes the soluble photoresist. Next, the glass substrate is immersed in an etchant solution. Depending on the feature depth, wet or dry etching may be employed.

This technique allows fabrication of structures only at the substrate surface. Therefore, in case of fabricating microchannels buried in the sample, an additional bonding step is necessary. Glass bonding is commonly achieved by adhesive, anodic or thermal bonding which requires application of high pressures, temperatures and voltages. These processes may damage the device structure and can also cause leakage of liquid samples and clogging of thin channels.

Photolithography also allows fabrication of optical components. However, monolithic integration of multiple functionalities has been proven difficult given that photolithography is a planar technique. Three-dimensional fabrication has been achieved by stacking multiple two-dimensional (2D) structures, making the entire process time consuming and complex, since a failure in one layer will affect the performance of the entire device [10].

In addition, spatial resolution is affected by the diffraction criterion and the resolution limit is around 250nm. To achieve lower resolutions, one can perform deep UV exposure or electron-beam lithography which allows obtaining submicron (100nm) features, but at the expense of increasing fabrication time.

Photolithography is also poorly suited for introducing specific chemical functionalities, for patterning non-planar surfaces and for integration of silicon with other materials (glass, polymers, carbon) besides semiconductors [2].

This technique is also expensive, requiring access to specialized cleanroom facilities. Therefore it is only marginally useful in applications requiring rapid evaluation of prototypes, suggesting the need for alternative microfabrication techniques [19].

2.2.2 Soft Lithography

Soft lithography is a replication technique, which enables fabrication of devices on polymers, in particular PDMS. This technology encompasses many techniques, being replica molding the usually used to fabricate structures in PDMS. Replica molding requires two components: a master, bearing topographic features, and a stamp on which the features are molded. In the following, we review this fabrication procedure, which is represented in figure 2.1. Further details regarding this technology can be found elsewhere [34].

The master is usually fabricated by photolithography, by producing the features in photoresist SU8 spin-coated on a silicon wafer. Conventional photolithography seems to be the best method to generate complex patterns, achieving a minimum feature size of 1μm [35].

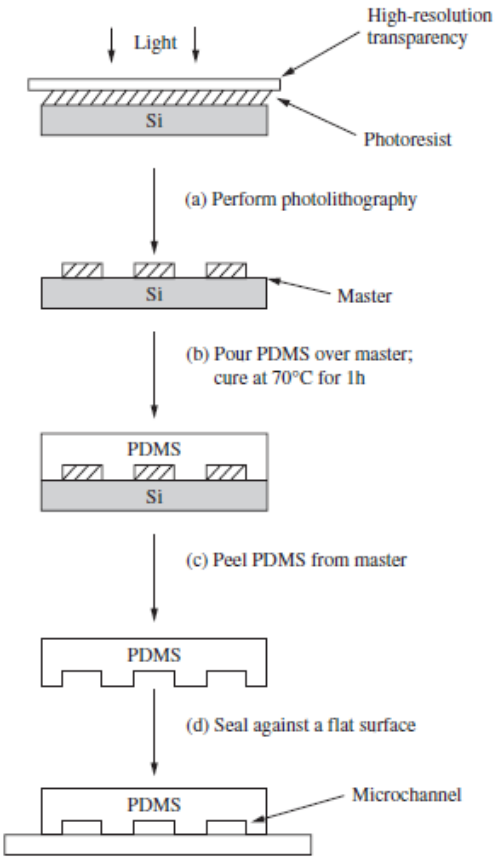

Figure 2.1: Soft lithography fabrication procedure [19].

The PDMS used as stamp is supplied in two components, a base and a curing agent. Silicon hydride groups present in the curing agent react with vinyl groups present in the base and form a cross-linked elastomeric solid. The two agents are usually mixed in a 10:1 ratio (base:curing agent), depending on the desired viscosity and on the final application. The pre-polymer is then poured over the master and cured for 1-2 hours at around 70°C. The liquid PDMS conforms to the shape of the master and replicates the features with high fidelity. Due to its elasticity it is released easily from the master.

The structures are produced at the surface, which requires an additional sealing process [19]. The PDMS may be sealed reversible or irreversible against a PDMS, silicon, silicon nitride or glass slab or against other polymers (polystyerene, polyethylene).

The reversible sealing may be performed in ambient laboratory conditions and is achieved by conformal contact (van der Waals contact) of the PDMS and the sealing layer. Given that PDMS is hydrophobic, the resulting device does not support electro-osmotic flow [36]. It can also be dismantled by washing it in water, in a releasing process that can occur multiple times without degradation of the PDMS layer, and it can not withstand pressures greater than 5psi.

To form an irreversible seal, the PDMS and the sealing surface are exposed to an air/oxygen plasma for 1 minute, generating silanol groups on the surface of each layer [36]. To avoid reconstruction of the oxidized PDMS, the two surfaces must be brought in contact quickly. Contact with water or polar organic solvents maintain the surfaces hydrophilic indefinitely. This property may be used to produce optofluidic devices where a PDMS slab (containing the

microfluidic channel) and a silica slab (containing the optical system) are irreversibly sealed [18].

Replication Techniques

As described before, soft lithography is a replication technique in which an elastomeric stamp/mold transfers a pattern to a substrate. The replication may be achieved by contact printing, replica molding, embossing, phase-shift optical lithography and nanoskiving, figure 2.2 [23]. All these techniques rely on physical contact of the stamp. The stamp is usually a PDMS layer produced with the technique described previously.

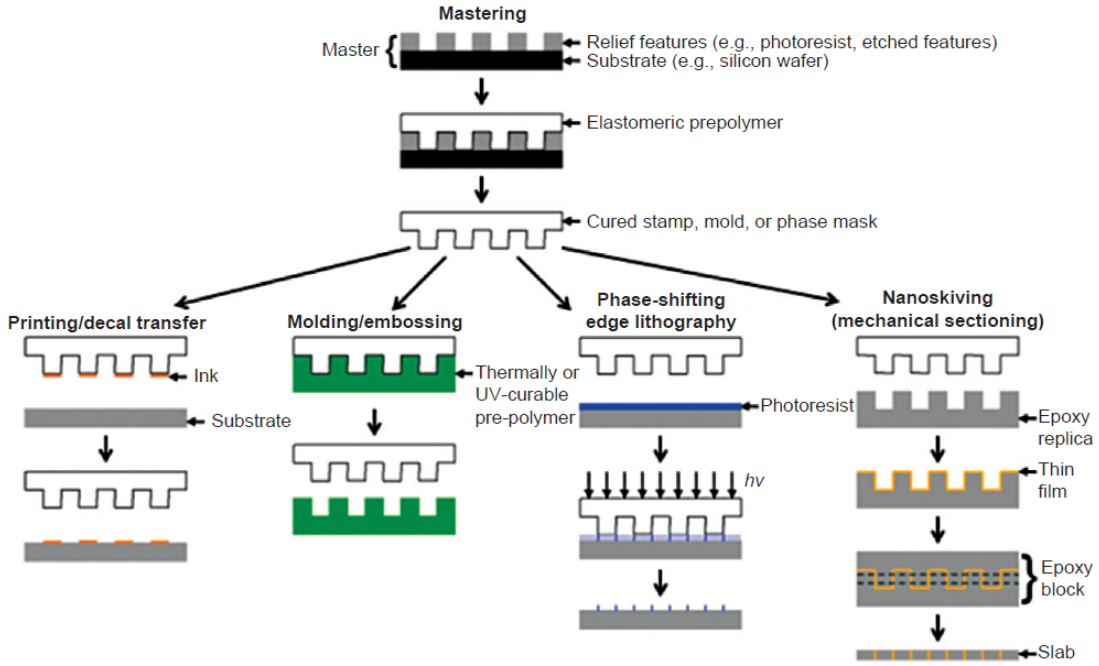

Figure 2.2: Schematic of most commonly used replication techniques based on PDMS [23].

Contact printing is an efficient method for pattern transfer that relies on replicating nanoscale features directly [35]. In this technique an ink material is deposited over the stamp surface which is transferred to a slab material when the slab and stamp are put in contact. This technique is simple, inexpensive and convenient, enabling use of the same stamp multiple times and allowing formation of patterns over large areas. However it is a 2D fabrication process.

In replica molding there is a one-to-one correspondence between the dimensions of the stamp and the final pattern. Here, a liquid polymer placed on top of a cast is cured and then removed from the cast, in a process similar to the one described in the previous section. This technology accommodates a wider range of materials than photolithography.

Embossing is another cost-effective, high-throughput manufacturing technique that imprints microstructures in thermoplastic materials [35]. In this process a polymer is deposited over a slab which is then put in contact with the cast. By applying pressure or heat over the entire system, the polymer adapts itself to the cast surface.

Phase-shifting edge lithography and nanoskiving form patterns with nanoscale linewidths indirectly, by using the edges of the topographic features [23]. The master for these techniques

can thus have features that are larger than the dimensions of the desired structures. In phase-shifting edge lithography the stamp behaves as a conformal optical mask, where the edges of the features are transferred to a film of photoresist. In nanoskiving, the stamp molds an epoxy prepolymer, which is coated with a thin metallic, semiconducting, dielectric, or polymeric film, embedded and sectioned with an ultramicrotome.

All these techniques can be repeated multiple times with resolutions of around tenths of micrometers, which is one of the key advantages of soft lithography. Soft lithography may also be employed in ambient laboratory conditions. Being a contact technique, it is not subject to optical diffraction and optical transparency. This technique also offers access to new types of surfaces and systems that can be difficult to fabricate by photolithographic procedures. The biggest challenge, and the one which demands more resources, is the fabrication of the master structure.

Disadvantages

Soft lithography, however as some disadvantages [35]. For instance, releasing the stamp from the master may generate cracks on the stamp. In addition, the stamp quality is damaged after replication.

Although the replication has high resolution, when fabricating the stamp, the PDMS shrinks [35]. Also, the stamp presents additional roughness due to the worse resolution of the master production process [36].

The replication may be performed on ambient laboratory conditions. However, given that soft lithography is a planar technique, the structures may be contaminated. To solve this problem, the entire process may be done in cleanroom facilities which are expensive and not available for all researchers.

As mentioned this technique is planar, hampering 3D fabrication. Three-dimensional structures may however be produced by pilling thin 2D layers, resulting in a more complex process [34]. In particular, integration of optical layers with microfluidic channels has proved to be challenging [37].

2.3 Laser Theory

A laser is a device that generates light by means of stimulated emission of radiation [13]. The two components necessary for laser operation are a laser cavity and a gain medium. The laser cavity only allows propagation of certain cavity modes in which the photons can propagate. Build-up of laser radiation within the cavity is achieved initially via spontaneous emission and then is amplified by stimulated emission from the gain medium.

The lasers may operate in two different regimes: continuous wave (CW) and pulsed mode. For production of three-dimensional LOC devices by laser micromachining, femtosecond laser pulses are usually employed. These exhibit major advantages over CW lasers and long pulses: (i) the ultra-short pulse duration enables a measurement with extremely short temporal resolution and (ii) the focused pulses can generate extremely high intensities (TW/cm^2) and induce non-linear absorption on a transparent material [28].

From the various types of femtosecond laser systems, Ti:sapphire and Ytterbium based fiber lasers are the commonly used for micromachining [13].

Regeneratively amplified Ti:sapphire lasers are solid state lasers that emit radiation at 800-1000 nm (other wavelengths may be generated by optical parametric amplification and second or third order harmonic processes) with 1–500 kHz repetition rate, a few μJ pulse energy and 50–200 fs pulse duration [28].

Doped fiber laser systems usually operate at 1044nm, but other wavelengths can be produced by second or third order harmonic generation. These lasers can provide various combinations of repetition rates and pulse energies, and have the advantage of being more stable than their solid state counterparts, a critical factor for the design of photonic devices [38].

Ultrashort pulses are usually fitted by a Gaussian or squared secant envelope, where the full-width half-maximum of the intensity curve describes the pulse duration. The interaction between laser and matter is influenced by many parameters: beam polarization, laser wavelength, pulse energy, pulse duration, repetition rate. All these quantities affect the laser fluence – energy delivered per unit area – which is described by the following equation $F = \frac{E_p R}{\pi \nu \omega}$, where E_p is the pulse energy, R the repetition rate, ν the emission laser frequency and ω the beam spot size. This parameter is perhaps the most important in describing the laser-matter interaction. Other factors also influence this interaction: for example in order to reach an intensity capable of inducing optical breakdown of the sample, the pulses are focused with an objective lens. Thus the numerical aperture is also an important parameter one should keep an eye on.

2.3.1 Generation of ultrashort laser pulses

Femtosecond pulses are produced by a method called mode locking [13]. Without frequency selective elements inside the laser resonator, the laser generally oscillates simultaneously on many resonator modes within the spectral gain profile of the active medium. The laser output is the sum of the intensities of all oscillating modes, but because there is not a phase relation between the different oscillating modes the output is incoherent. If coupling between the phases of these simultaneously oscillating modes is established, a coherent superposition of the mode amplitudes may be reached, leading to the generation of short output pulses in the picosecond to femtosecond range. Hence, the laser can be mode-locked by inserting elements into the cavity, which lock the modes of the cavity by periodically changing the gain/loss inside the cavity resonator. There are three ways for mode-locking: (a) active, by using optical modulators; (b) passive, by adding a saturable absorber; or (c) a combination of the previous methods.

This technique however produces pulses with low energy. The amplification can not be done directly because the high peak powers generated can damage the optical elements used for amplification. Thus a method called chirped pulse amplification (CPA) is usually employed, figure 2.3. The original pulse is temporally stretched from femtosecond to picosecond duration by passing through a highly dispersive medium, usually a grating pair. This process decreases the laser peak power, so that the pulse can be amplified directly without damaging the amplification system. The laser beam then passes several times through an amplification medium increasing the pulse energy by 6 to 9 orders of magnitude. Finally, the pulse is

recompressed using a grating compressor, so that the pulse has the original temporal duration. CPA requires high accuracy in the design and manufacture of the system to avoid amplitude and phase distortions.

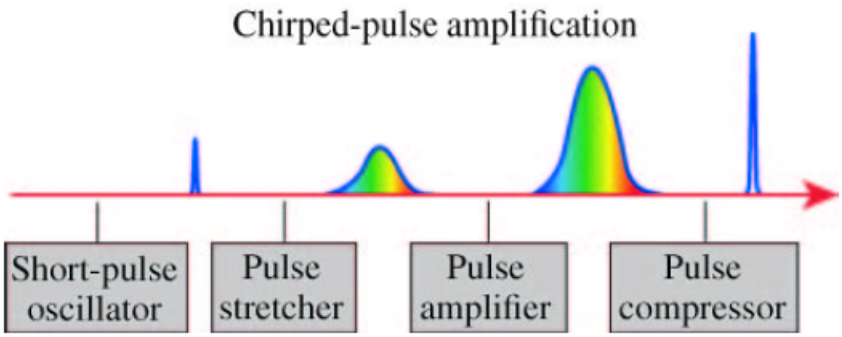

Figure 2.3: Schematic of CPA process [38].

2.3.2 Linear and non-linear effects

The femtosecond laser pulse propagation is affected by both linear (dispersion, diffraction, aberration) and non-linear (self-focusing, self-phase modulation) optical effects altering the energy distribution and the machining process [10]. Here we analyze the influence these effects have on the pulsed beam and how these effects can be corrected [13].

Chromatic aberration is the result of dispersion in the lens and is corrected by employing chromatic aberration-corrected microscope objectives for the wavelength spectrum of interest.

Spherical aberration occurs because after passing through the objective, the light rays fail to converge to the same point [29]. This problem is enhanced when micromachining glass, due to the mismatch at the air-glass interface. This problem may be solved by using aspherical lenses or index-matched lenses.

Dispersion effects broaden the laser pulse reducing its peak intensity. However, in micromachining systems where the pulse duration is around 200fs this effect is negligible [38].

Considering a femtosecond laser beam focused inside a glass sample, the glass refractive index may change as shown by the formula $n = n_0 + n_2 I$, where n_0 is the linear refractive index, n_2 is the nonlinear refractive index and I is the beam intensity. Since the power at the axis of the beam is greater than on its wings, and given that fused silica has a positive n_2 (equal to $3 \times 10^{-16} cm^2/W$), there is a redistribution of the refractive index and thus the medium acts as a focused lens. This self-focusing effect only occurs when the laser peak power exceeds a critical power, given by the following equation $P_c = \frac{3.77\lambda^2}{8\pi n_0 n_2}$, where λ is the wavelength, n_0 the linear refractive index and n_2 the non linear refractive index. This effect leads to the pulse collapse. However as the beam self-focuses, the intensity is high enough so that it ionizes the material producing a plasma that acts as a diverging lens, countering the self-focusing effect. A balance between these two processes leads to filamentary propagation, generating axially elongated refractive index structures, which are undesirable in waveguide fabrication [10]. In femtosecond laser direct writing systems that use low numerical aperture lenses to focus the beam, the beam intensity may surpass the critical power enabling self-focusing.

The refractive index may also vary because the beam intensity has a Gaussian profile in time. Thus the refractive index quickly changes in time, in an effect denominated self-phase modulation. This effect produces a chirped pulse, generating new frequencies and broadening the pulse. This process however is not relevant in our laser direct writing system.

2.4 Laser-matter interaction

Traditional machining techniques, such as photolithography and soft lithography, involve direct contact with the substrate, which can damage and contaminate its surface. In addition most applications require 3D microstructures which are difficult to produce using these methods. Also while many different fluidic applications have already been implemented with the former technologies, a key unsolved problem is the integration of optical functionalities for on-chip optical detection. Given these issues, femtosecond laser processing, although time consuming, offers new advantages to the design of LOC devices.

First, it is a non-contact technology with minimal contamination and machine wear.

Second, it allows for custom fabrication of 3D structures, due to its ability to internally modify the material – usually glass – properties by non-linear absorption processes. The non-linear nature of the optical absorption confines the induced changes to the focal volume thus sub-micron resolution is attainable. The absorption process is also independent of the materials, as long as they are transparent to the laser beam wavelength [21].

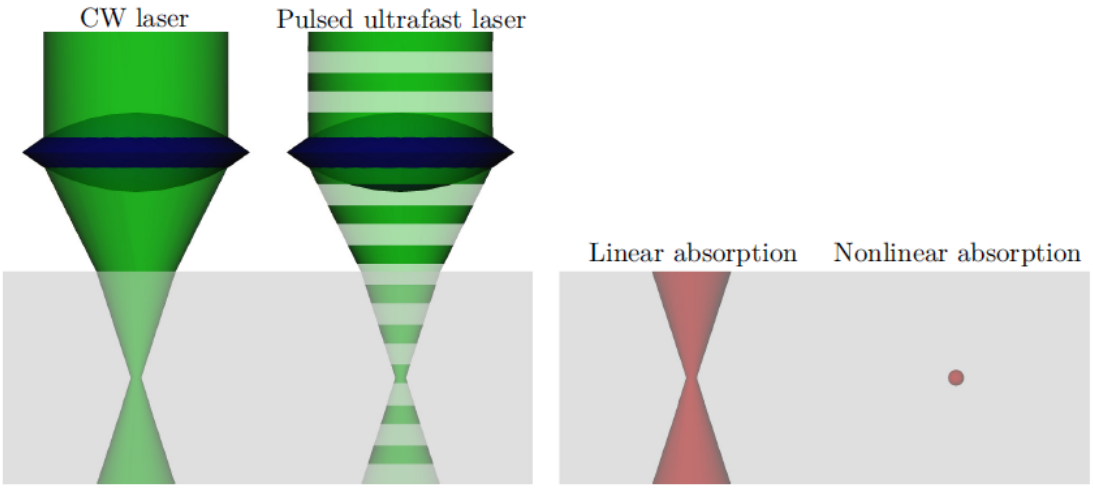

Figure 2.4: Comparison of the modified regions in processes ruled by linear absorption (associated with CW pulses and with longer pulses) and by non-linear absorption (associated with ultra-short pulses) [28].

Third, comparing it to CW lasers, the interaction with matter is a deterministic process, thus the optical response can be predicted. Even with picosecond pulse lasers non-linear absorption is not allowed and the results obtained are erratic and unpredictable.

Fourth, it minimizes thermal diffusion effects and formation of heat affected zones which enhances spatial resolution [21]. This is due to the fact that the pulse duration is shorter than the electron-phonon coupling time and so the energy associated with the pulse can be deposited

into the electrons before being transferred to the lattice, figure 2.5.

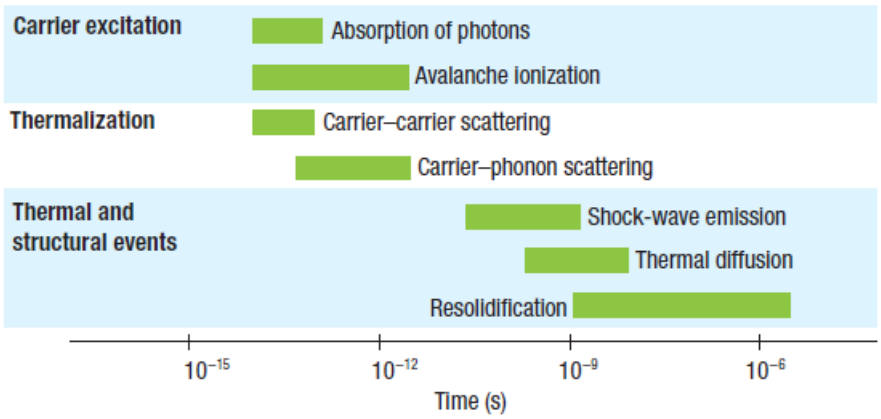

Figure 2.5: Timescale of the physical phenomena resulting from the interaction of an ultrashort pulse with transparent materials. Although light absorption occurs at the femtosecond timescale, the material can undergo changes microseconds later [24].

Fifth, it allows multifunctional integration. Optical, fluidic and mechanical components can be fabricated in the same sample and in the same writing procedure.

Fundamental investigations into laser processing of materials have revealed that the time dependence of electron and lattice dynamics is different for long and for ultrashort laser pulses [26]. For ultrashort pulses, the laser-matter interaction can be described qualitatively in three steps: (i) generation of free electron plasma, (ii) followed by energy relaxation and (iii) modification of the material properties, which will be discussed in detail in the following sections.

Currently there are three technologies for fabricating microfluidic and optofluidic devices that use femtosecond laser direct writing: FLICE (Femtosecond Laser Irradiation followed by Chemical Etching), 2PP (two-photon polymerization) and ablation.

2.4.1 Laser induced structural changes

When a femtosecond laser beam with very high intensity is focused inside a substrate, transparent to the beam wavelength, non-linear absorption occurs. Unlike in linear absorption, where the absorbed photon has an energy higher than the bandgap energy of the material, thus exciting an electron from the valence band to the conduction band, in non-linear absorption a single photon can not excite an electron, figure 2.6. However, when an extremely high density of photons (with electric field intensities of the same order of magnitude as the electric field of the material's valence electrons bond) is incident on the material an electron can be excited by two different mechanisms: multiphoton absorption and Zener/tunneling ionization [24].

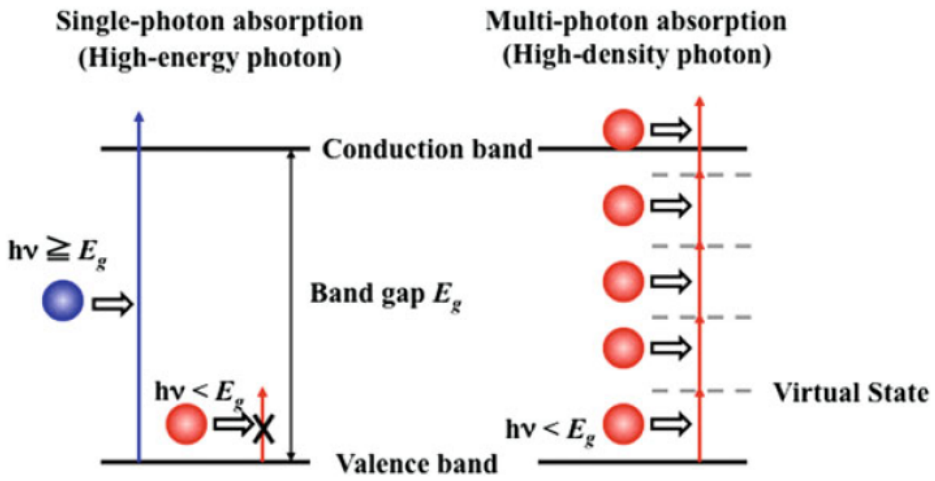

Figure 2.6: Comparison between single (left) and multi-photon (right) absorption [21].

In multiphoton absorption, figure 2.7a, multiple photons (each with energy lower than the bandgap energy) with total energy higher than the bandgap energy are simultaneously absorbed, exciting the electron to the conduction band. This process usually happens at high frequencies and low laser intensities [39].

At high laser intensities and low frequencies, electron excitation is commonly induced by tunneling ionization, figure 2.7b. Here, the potential barrier formed by the valence and conduction band is deformed by the intense electric field, reducing the bandgap energy. Therefore, the electron can tunnel into the conduction band [10].

The absorption is only confined to the focal volume, where the intensity is above a threshold value that depends on both the irradiation conditions and on the material. The absorbed energy distribution has a Gaussian profile with narrow width (that decreases with increasing absorption order), so that absorption occurs in a volume smaller than the spot size, therefore overcoming spatial limitations due to the limit of diffraction and further improving spatial resolution.

The occurring absorption mechanism can be predicted by the Keldysh parameter $\gamma = \frac{\omega}{e}\sqrt{\frac{m_e c n \epsilon_0 E_g}{I}}$, where m_e and e are the effective mass and charge of the electron, I is the laser intensity at the focus, E_g is the material bandgap energy, ω is the laser frequency, n is the linear refractive index, c is the speed of light in vacuum and ϵ_0 is the permittivity of free space [39]. If γ is lower than 1.5 then tunneling ionization is favoured. If it is bigger than 1.5 the absorption occurs by multiphoton absorption. If it is around 1.5, the absorption is a combination of the two mechanisms that occur simultaneously.

The electron at the conduction band, while exposed to an intense laser field, is accelerated and acquires kinetic energy. The electron then releases its excess energy (energy higher than the conduction band minimum energy) to excite another valence band electron to the conduction band, in a process called collisional ionization. This process acts repeatedly leading to avalanche ionization, shown in figure 2.7c, where the electron population in the conduction band (N) grows exponentially according to the equation $\frac{dN}{dt} = \alpha I N$, where I is the laser beam intensity and α is the avalanche ionization coefficient. A minimum number of electrons present in the conduction band is necessary to initiate this process, so the absorption mechanisms act as seed for the avalanche ionization [10].

Avalanche ionization leads to the formation of a highly absorptive and dense plasma inside the focal volume which oscillates at frequency $\omega_p = \sqrt{\frac{e^2 N}{\epsilon_0 m_e}}$, where m_e and e are the mass and charge of the electron respectively, ϵ_0 is the vacuum permittivity and N is the density of free electrons. The plasma frequency increases as the density of free electrons in the conduction band increase. When the plasma frequency matches the laser frequency, the wave field and the plasma enter in resonance with each other. The plasma then transfer energy to the lattice by electron-phonon coupling over a picosecond timescale, long after the laser pulse is gone avoiding thermally excitation of any ion. Within a couple of nanoseconds, a pressure or a shock wave separates from the dense, hot focal volume. On the microsecond timescale, the thermal energy diffuses out of the focal volume. If the deposited energy is above a threshold level these processes cause melting or non-thermal ionic motion, altering permanently the material structure [24].

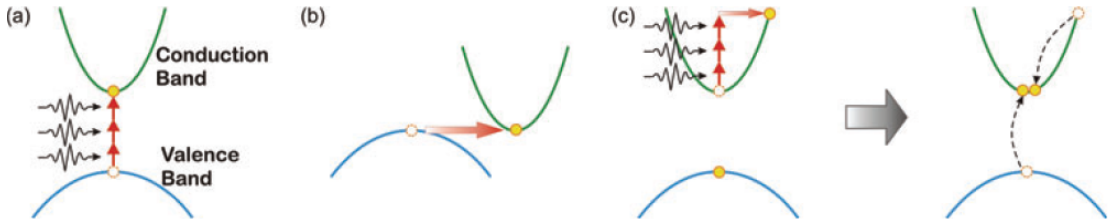

Figure 2.7: Non-linear absorption processes: (a) multiphoton absorption, (b) tunneling ionization and (c) avalanche ionization [39].

The induced structural changes depend on the exposure parameters (pulse energy, pulse duration, repetition rate, wavelength, beam polarization, focusing numerical aperture, scanning speed) and on the material properties (bandgap energy, thermal diffusivity coefficient) [10]. Being fused silica glass the focus of the majority of this work, the effect of femtosecond laser irradiation on this material will be discussed in further detail. The laser induced modification on fused silica glass can be classified in three regimes based on the observed morphology: (i) smooth refractive index change, (ii) formation of self ordered nanogratings and (iii) disruptive modification and formation of voids [13].

2.4.2 Regime I

The first regime, which occurs at low laser fluence, is associated with a smooth and uniform refractive index modification suitable for producing low-loss optical waveguides. The physical mechanisms underlying this modification are not yet fully understood, however the following effects take part in the index modification: stress-induced changes, changes in effective fictive temperature and colour centre formation [24]. The influence of these processes depends on the material and on the machining conditions. Although the process behind the index modification is out of the scope of this thesis, in the following paragraphs we provide the basics of each process [13].

The densification approach is a non thermal explanation. When the energy is transferred to the material, it heats it to a very high temperature. As the heated volume cools down, the

volume density is modified due to stress redistribution in the glass matrix thus changing the refractive index.

Colour centres (defects in the regular spacing of atoms) are induced upon exposure and absorb in the ultraviolet, which leads to a change in refractive index through the Kramers-Kronig mechanism.

The fictive temperature model is a thermal mechanism associated with non-uniform cooling. After irradiation, the material melts out to a radius where the temperature equals the melting temperature of the glass. Molten material just inside this radius then quickly quenches and solidifies into a lower-density structural arrangement of the glass. This quenching continues radially inward as the glass continues to cool. Because there is no free surface that can expand to take up the extra volume occupied by the less dense glass formed by this quenching, the material near the focal region is put under pressure. As a result of this pressure, the material near the focal region solidifies into a higher density phase, leading to the higher refractive index at the core of the structures.

2.4.3 Regime II

The second regime produces organized birefringent sub-wavelength nanogratings. These structures consist of thin regions with refractive index n_1 characterized by a strong oxygen deficiency, surrounded by larger regions with refractive index n_2.

The mechanism for the formation of these nanogratings is not yet fully understood, however the nanoplasmonic model proposed by Hnatovsky et al [40] is the most successful in explaining the observed results. This model, represented in figure 2.8, involves the following steps: (a) in the focal volume, hot spots for multiphoton ionization are formed due to the presence of defects or colour centres; (b) the hot spots evolve into spherically shaped nanoplasma droplets over successive laser pulses due to a memory effect; (c) field enhancement at the boundaries of the droplets results in asymmetric growth of them in a direction perpendicular to the laser polarization, leading to the formation of nanoellipsoids, which eventually grow into nanoplanes; (d) the nanoplanes are initially randomly spaced, when the electron plasma density inside them exceeds the critical density, they become metallic and start influencing light propagation in such a way that they assemble in parallel nanoplanes spaced by $\lambda/2n$ where λ is the laser wavelength and n the material refractive index.

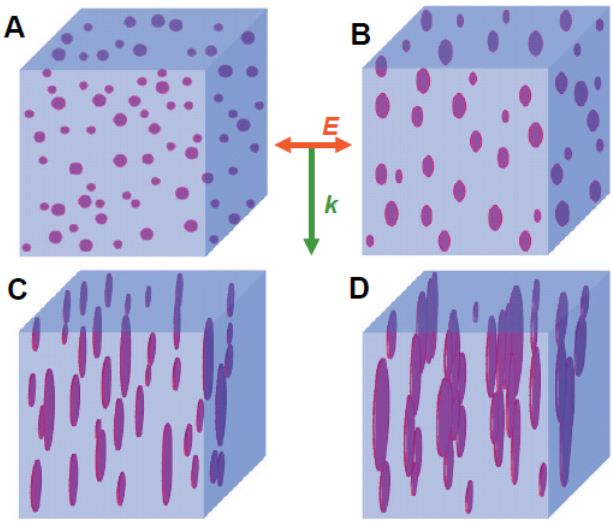

Figure 2.8: Nanograting formation model [40].

The nanograting formation relies on the cumulative action of multiple femtosecond laser pulses impinging on the same spot and depends on both the irradiation conditions (pulse energy, scanning speed and repetition rate) and on the alignment of the writing laser polarization.

This modification allows fabrication of microchannels (as it will be shown later when discussing the FLICE technique) and design of waveplates and polarization converters [13].

2.4.4 Regime III

In the third regime, increasing the pulse energy increases the size of the affected area and the average energy of the plasma. As the plasma energy grows, ionic shielding is reduced causing Coulomb repulsion between ions leading to disruptive modification. Pressures greater than the Young modulus are generated in the focal volume, creating a shock-wave that propagates radially outward producing a void surrounded by a region of densified material. This regime finds application in data storage and photonic crystals. It may also be exploited to design microfluidic channels, as it will be explained later [41].

Figure 2.9 summarizes the non-linear absorption processes and the laser-matter interaction regimes discussed above.

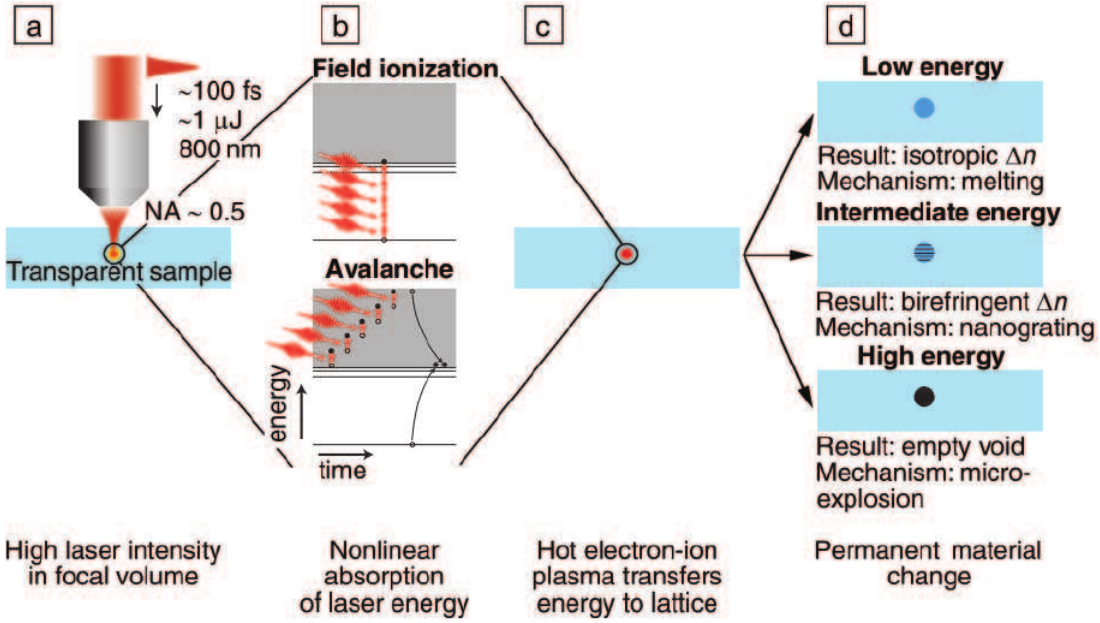

Figure 2.9: Summary of the interaction between femtosecond laser pulses and fused silica [10].

2.4.5 Effect of longer pulses

Another kind of modification is possible if the pulse duration is longer than the timescale for heat to diffuse away from the focal volume [42]. In this regime, heat builds up around the focal volume and the resulting structure is determined by cumulative thermal effects. In this case, avalanche ionization is seeded by impurities or defect states, resulting in a stochastic and irreproducible process. This regime however has been used to produce low-loss waveguides because the modified volume is bigger.

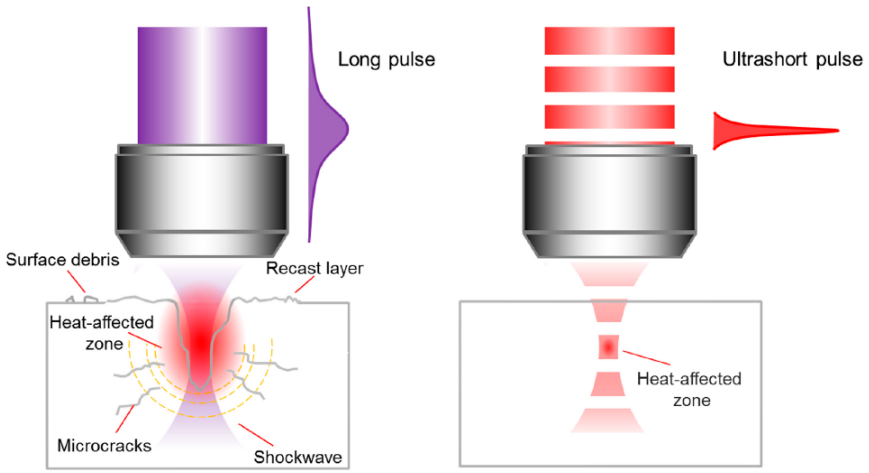

Figure 2.10: Comparison of the effect of longer pulses (left) and shorter pulses (right) on the irradiated material [26].

2.5 Femtosecond Laser Irradiation followed by Chemical Etching

The FLICE technique encompasses two steps for fabrication of microfluidic devices: laser direct writing and etching. In the first step, the beam is focused inside the sample changing its local properties depending on the irradiation conditions. Secondly, the sample is immersed in an etchant solution, selectively removing the irradiated zones. To this date only two different kinds of glasses have been used to produce microfluidic devices: fused silica (first shown by Marcinkevicius et al [16]) and Foturan glass (demonstrated by Kondo et al [27]), but recent tests show that this technology may also be applied to optical fibers. In the following we discuss the fabrication procedure for each glass.

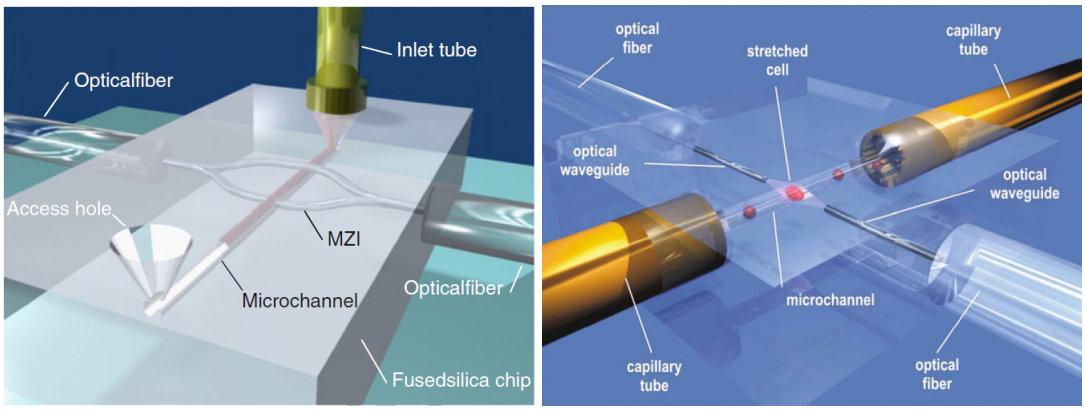

Figure 2.11: Example of lab-on-a-chip devices fabricated by femtosecond laser micromachining [10]. The two devices integrate fluidic channels with optical detection schemes: the left picture is an example of a Mach-Zender interferometer used for refractive index measurements; the right picture depicts a device that uses light for cell manipulation.

2.5.1 Fused Silica

When fused silica is exposed to a femtosecond laser, the modifications induced can be classified, as seen before, into three categories, depending on the laser processing conditions: (a) at low fluences, a smooth modification is achieved resulting in a refractive index change; (b) at moderate fluences, sub-wavelength nanogratings are produced, resulting in a high etching selectivity of the irradiated volume with respect to the pristine one; (c) at high fluences, disruptive modification occurs, which is accompanied by formation of voids [39]. Regime (b) is the one employed in the FLICE technique (see figure 2.12): when non-irradiated fused silica is immersed on hydrofluoric acid or hot potassium hydroxide (the only two known fused silica etchants) it is etched isotropically; however after laser direct writing the modified volume is etched at a higher rate. This etching selectivity is due to the combination of two mechanisms [10].

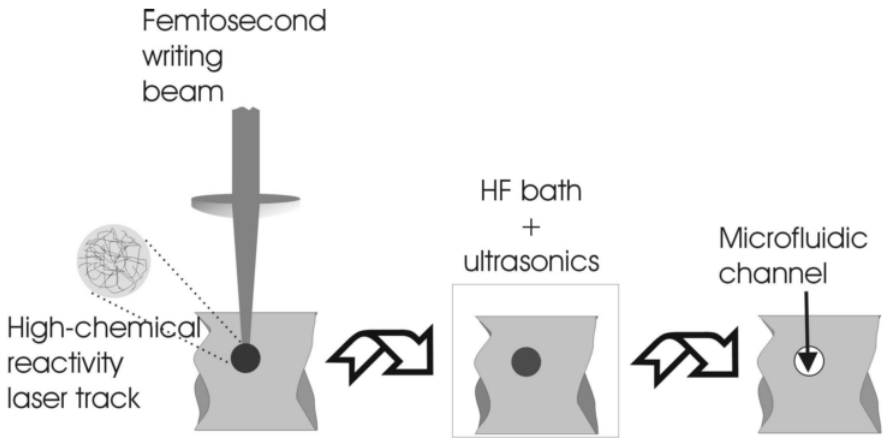

Figure 2.12: Illustration of the FLICE fabrication technique in fused silica [43].

First, it is related to the decrease of the Si-O-Si bond angle induced by the hydrostatic pressure or compressive stress created in the irradiated region. Agarwal et al [44] related the Si-O-Si bond angle change to various glass properties, namely etch rate, density, induced stress and refractive index. In particular, the decrease in the bond angle results in an increase in the etch rate and in the refractive index.

The second mechanism is related to the formation of self-ordered nanogratings structures. As proposed by Hnatovsky et al. [29], the formed nanogratings allow the etchant to diffuse inside the sample resulting in a etch rate bigger in the exposed zones than in the non-exposed zones.

The etch rate, among other factors, depends mainly on the etchant chosen and on the alignment between beam polarization and scanning direction [45]. In the nanograting structures with the planes perpendicular to the writing direction, the acid encounters alternate layers of nanoplanes and unmodified material (that etches slowly), thus reducing the cumulative etch rate, figure 2.13a [29]. However, when the nanocracks are aligned with the writing direction, the cumulative etch rate is very high as the acid flow is unobstructed and proceeds along large distances, figure 2.13b.

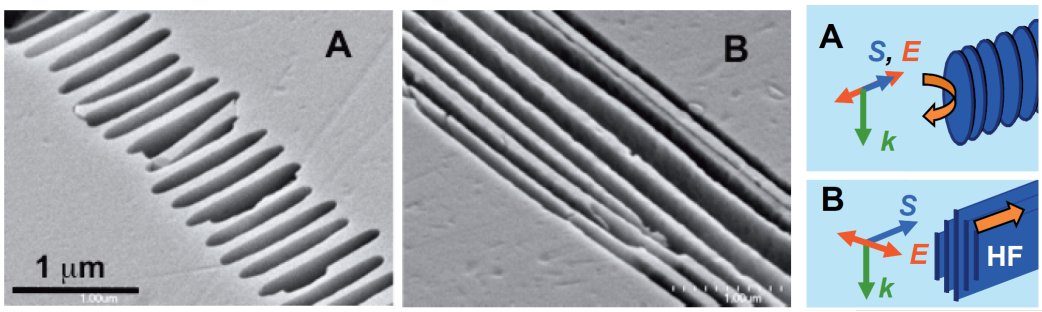

Figure 2.13: SEM images of formed nanogratings in fused silica and influence in the etching process: (a) writing with parallel polarization and (b) writing with perpendicular polarization [40].

Fused silica may be etched by hydrofluoric acid (HF) and potassium hydroxide (KOH) at 80°C. Analyzing the effect of etching with hydrofluoric acid [46], the chemical reaction is given

by the following equation

$$SiO_2 + 6HF \rightarrow H_2SiF_6(aq) + 2H_2O$$

Given that during etching the HF concentration decreases, which is followed by a decrease in the etch rate, buffered solutions may also be used. The chemical reaction with these solutions is given by

$$SiO_2 + 4HF + 2NH_4F \rightarrow (NH_4)_2SiF_6(aq) + 2H_2O$$

Highly concentrated HF solutions may also be used, where the presence of HF_2^- turns the etch rate 4.5 times higher than for a reaction with pure HF:

$$SiO_2 + 3HF_2^- + H^+ \rightarrow SiF_6^{2-} + 2H_2O$$

In choosing the HF concentration one must bear in mind that a higher etch rate is usually accompanied by a saturation effect that decreases the system aspect ratio. Thus there is a trade-off between aspect ratio and etch rate: higher HF concentration increases lateral etch rate decreasing aspect ratio; lower HF concentrations allow fabrication of uniform but short channels. Some solutions to prevent saturation are presented in the following chapters.

Recently, some groups have started to use hot potassium hydroxide which enables a higher etching selectivity without saturation, but at the expense of lower etch rates [47]. The reason for this enhanced selectivity is not yet fully understood, but it is attributed to the structural changes induced in fused silica by laser irradiation. The femtosecond laser produces silicon-rich structures (an excess of Si-Si bonds) that are minimally attacked by KOH.

The etch rate also depends on temperature, so this process must be done in a controlled environment. Etching may also be performed in ultrasonic bath which decreases the channel surface roughness, but may damage more delicate structures and change the etch rate, being hard to control its influence.

2.5.2 Foturan Glass

The process by which etching selectivity is generated in Foturan glass, shown in figure 2.14, is different than in fused silica: while for fused silica the etching selectivity is the result of a photophysical reaction, in Foturan glass it is due to a photochemical reaction.

When a femtosecond laser beam is focused inside the photosensitive glass, free electrons are generated by inter-band excitation, which reduce the silver ions to silver atoms. After writing there is not a visible change in the glass, which has to be subject to an annealing process, at temperatures between 500°C and 600°C.

During annealing, the silver atoms diffuse and agglomerate forming silver nanoclusters. The nanoclusters then act as seed for the formation of a crystalline lithium metasilicate phase that is etched faster than the amorphous material. However, according to the work developed by Fuqua et al [48], the etching selectivity only occurs if the crystalline phase density is above a threshold level [12].

The phase density is related to the laser dose, D , which is defined by the following formula

$D = F^m N$, where m is a constant, F is the laser fluence and N is the number of pulses. A critical dose is usually defined as the lowest necessary dose to obtain modification of the glass and depends only on the writing parameters and on the material composition. Above this value the glass undergoes structural change, while for doses below the critical there is no modification for selective etching.

The parameter m is a constant, usually equal to six, representing the number of photons involved in the absorption and free electron generation process [9]. The chemical reaction can thus be understood as follows: when the glass is exposed to a femtosecond laser beam, electrons are excited from the valence band to a defect level, resulting from impurities in the glass, by three-photon absorption; by absorbing three more photons the electrons transit to the conduction band. The absorption is thus a 6-order event, allowing internal fabrication with high spatial resolution, because the modified region is confined to a volume much smaller than the laser spot size [9].

After annealing the laser exposed regions become apparent, showing a dark color [9]. The sample is then etched in HF acid, in a similar procedure to the one employed in fused silica.

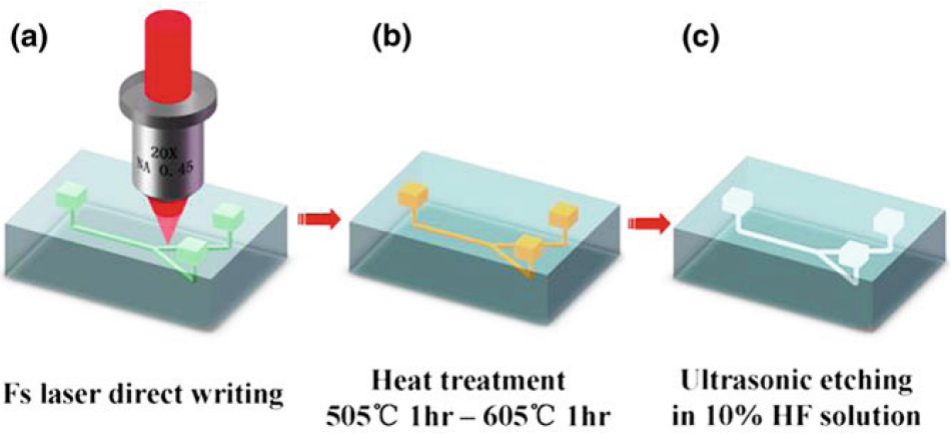

Figure 2.14: Illustration of the FLICE fabrication technique in Foturan glass [21].

There are some differences in the results obtained with fused silica and with Foturan glass: the etch rate is usually higher in Foturan but the etching selectivity is lower [10]. After etching, an additional annealing step may be performed in Foturan glass for surface smoothing, where the annealing temperature is around 500°C and 600°C, which is much lower and easier to achieve than for fused silica (1140°C). Photosensitive glass is also more attractive because it can be modified at much lower laser fluences, reducing fabrication costs and increasing throughput.

Etching selectivity may also be generated by exposing the Foturan glass to ultraviolet lighting, in a process different than the one that occurs for femtosecond exposure, in which the cerium ions reduce the silver [9]. However this methodology only allows 2D fabrication and the absorption is linear which decreases resolution.

2.6 Two-photon polymerization

The usual used materials for femtosecond laser induced polymerization are liquid resins and solid photoresists, that must include photoinitiators [13].

These materials are deposited on top of a flat glass substrate and exposed to a femtosecond pulse. When the laser beam is focused in these two materials, two-photon absorption (TPA) occurs [49]. There are two types of TPA processes: (i) degenerate, where the two photons absorbed have the same frequency; (ii) and non-degenerate, where the two photons have different frequency. Usually most TPA applications are due to degenerate processes. TPA is a non-linear effect, related to the third order susceptibility in the material polarization, where two photons induce an electron transition from the ground state to an excited state..

There are two different mechanisms for TPA: sequential TPA and simultaneous TPA [49]. In sequential TPA an electron is excited to an intermediate real state, whereas in simultaneous TPA, the intermediate state is a virtual level. This virtual level has a lifetime of a few femtoseconds, hence this approach is only possible when the material is exposed to a high-intensity femtosecond laser beam.

The excited electron then decays to the fundamental state emitting fluorescent light in the ultraviolet to visible range. The photoinitiators present in the resin/photoresist absorb the fluorescent light and generate free radicals. The radicals react with monomers, producing monomer radicals which propagate and react with other radicals, thus forming a polymeric chain. The entire procedure is summarized in figure 2.15 and can be described by the following reactions [50]:

initiation: $S \xrightarrow{hv,hv} S^* \cdots \xrightarrow{I} I^* \rightarrow R^{\cdot}$

propagation: $R^{\cdot} + M \rightarrow RM^{\cdot} \xrightarrow{M} RMM \cdots \rightarrow RM_n^{\cdot}$

termination: $RM_n^{\cdot} + RM_n^{\cdot} \rightarrow RM_{n+m}R$

where S is the photosensitizer, I the photoinitiator, $R^{\cdot}$ a radical, M a monomer and $*$ corresponds to an excited state.

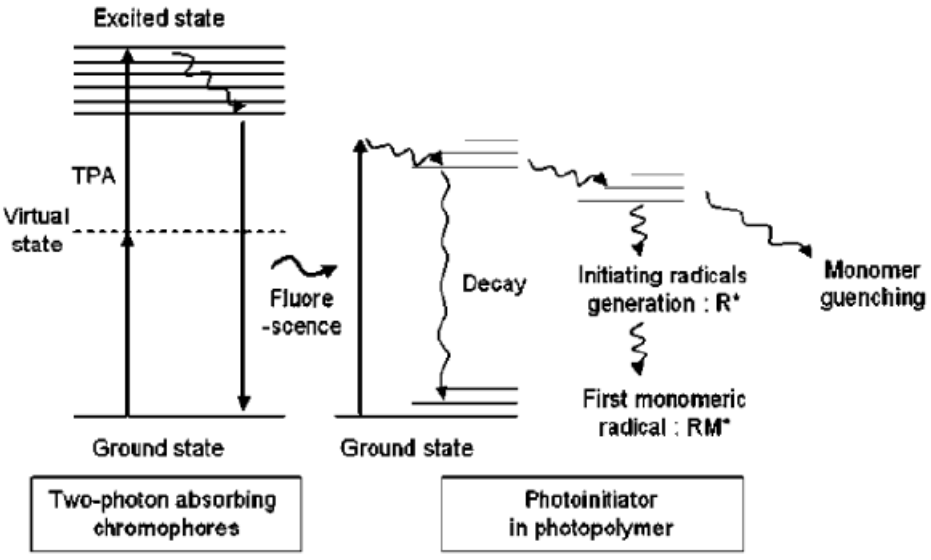

Figure 2.15: Schematic of laser induced 2PP reaction [49].

After femtosecond irradiation the resin/photoresist is developed in an appropriate solvent and rinsed to remove the unpolymerized regions [51].

2PP is an additive fabrication technique that only occurs above a threshold intensity of the laser beam. Ti:Sapphire lasers are commonly used with this fabrication method because their central wavelength is around 800nm, which is close to half the wavelength of polymerization for many ultraviolet photosensitive resins.

The two-photon transition rate is proportional to the square of the laser intensity and is extremely small. Therefore the polymeric chain reaction occurs only around the focal volume and the spatial resolution obtained is around 100-200nm, well beneath the diffraction limit [49]. This technique also avoids the use of photomasks, which can contaminate the material surface. The polymerization reaction can also be employed with UV exposure, where the absorption process is linear and the spatial resolution obtained is poorer.

This fabrication technique allows production of complex 3D structures by scanning the laser beam along the resin/photoresist. In addition, the produced structures may be replicated by soft lithography techniques. This method can also be employed in optical fibers to design light-guiding structures, as demonstrated in figure 2.16 [52, 53].

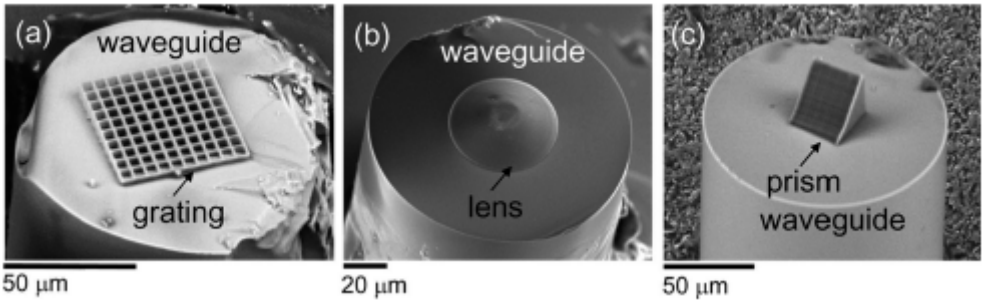

Figure 2.16: Structures produced at the tip of an optical fiber by 2PP for light guiding applications [26].

This technology also possesses some limitations. The produced structures can be deformed in the developing process, due to cohesive forces generated by surface tension of the rinsing material.

Two-photon polymerization is also a slow process. In order to speed up the fabrication process only the outer shells of the structure are polymerized, while the interior is polymerized in a post-fabrication UV treatment [52].

2.7 Ablation

2.7.1 Direct Ablation

As stated before, when a femtosecond laser pulse with high fluence is focused inside a transparent material, it induces optical breakdown and creates a void around the focal volume. This property has been applied to micromachine fused silica glass and to produce data storage devices and photonic crystals.

Although drilling is possible with longer laser pulses, femtosecond laser pulses are beneficial in that the ablation is tightly confined to the focal volume [41]. However some problems of this technique still stand. First, the holes produced have rougher surfaces, when compared to the roughness obtained by other techniques (FLICE and soft lithography). Second, the ablated debris starts depositing in the void, blocking it and impeding its growth [54]. Moreover, the ablated debris can cause laser beam scattering, which reduces the void diameter. Therefore, direct ablation does not allow fabrication of channels with long dimensions and with uniform aspect ratio [41].

2.7.2 Ablation with sample immersed in water

Due to the reasons mentioned above, a new technique has emerged in which the fused silica glass is immersed in distilled water during laser exposure [54]. Here, when the femtosecond laser is focused on the glass rear surface it creates a void and generates a shock wave and a high-speed jet that causes the water to etch the glass, thus removing the debris.

Given that the ablated void is formed only around the focal volume, this technique allows the design of longer microchannels and of more complex geometries. Comparing it to direct ablation, this methodology also allows fabrication of 3D channels. It also does not require post-fabrication processes, such as heat treatment or chemical etching. In comparison to FLICE technology, this technique does not rely on generating etch selectivity in materials, thus it can be applied to a wider range of materials transparent to the laser beam [21]. Also, because water is circulating in the channel upon its formation, the surface roughness is minimal.

However, channel length is still an issue, because the debris generated is not removed for lengths over 100μm and can clog the channel. A new strategy to increase the channel length is to fabricate the channels in porous glass [26]. After writing, the glass has to be subject to annealing to seal the pores which can damage the structures.

Chapter 3

Fabrication and Characterization Techniques

This chapter starts by reviewing the laser direct writing system and discussing its alignment. This procedure is critical for the fabrication of high quality photonic and microfluidic components. A review on the existent beam shaping and writing techniques is then presented. From this discussion we describe in detail the used protocol for fabrication of optical and fluidic components.

The characterization procedure of optical waveguides and Bragg gratings is also described. Although outside the scope of this thesis we present the optimum conditions to produce low-loss optical waveguides and Bragg gratings obtained by Vítor Amorim and with this experimental system; these results were important for integration of microfluidic channels with optical layers.

3.1 Laser direct writing unit

In the writing unit, it is used a fiber-amplified laser from Amplitude Systèmes. The emitted pulse has a duration of 250fs (full-width half-maximum (FWHM) with Lorentzian profile), the repetition rate can be changed between 500kHz and 2MHz and the maximum average power is 10.5W at the fundamental wavelength (1030.3nm). It is possible to generate second and third harmonic radiation with this laser system. The most important parameters, at repetition rate 500kHz, are summarized in table 3.1.

Parameters	Measured Value
Fundamental wavelength	1030.3nm
Bandwidth	8.4nm
Beam diameter	1.5mm
Polarization ratio	1200:1
Pulse duration	250fs
Maximum average power	10.5W
Maximum energy per pulse	23μJ

Table 3.1: Laser parameters.

In the laser direct writing system used, three different wavelengths can be chosen: 1030.3nm

(fundamental wavelength), 515nm (second harmonic generation) and 343nm (third harmonic generation). According to Dostovalov et al [55], the amount of energy absorbed by the fused silica substrate is higher for the second harmonic than for the fundamental harmonic, inducing a higher modification contrast and enabling fabrication of low-loss waveguides. In addition, the fundamental wavelength has been shown to produce irregular damage tracks. Furthermore, the beam waist radius depends on the wavelength; as a result the second harmonic also enhances the spatial resolution obtained. In the second harmonic, the maximum energy per pulse is 1.1μJ and the maximum average power is 5.5W, at a repetition rate of 500kHz.

The beam power is controlled by an external modulator Watt Pilot from Altechna, schematically shown in figure 3.1. This uses a half-wave plate that determines the power in each polarization state, by adjusting the angle between the plate axis and the direction of the beam's initial state of polarization. Using a thin film placed at the Brewster angle relative to the beam, the two polarization states are separated. In writing it is used the beam with s-polarization.

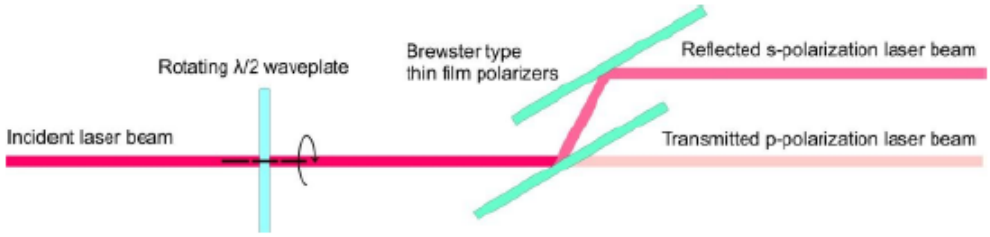

Figure 3.1: Schematic of the power control unit [38].

The repetition rate and beam power are defined in the laser control software.

Figure 3.2 shows a schematic of the writing unit [38]. After the power control unit, the beam crosses an expansion system, formed by two planar-convex lenses (L1 and L2) with focal lengths 35mm and 80mm respectively; the distance between lenses is equal to the sum of the respective focal lengths.

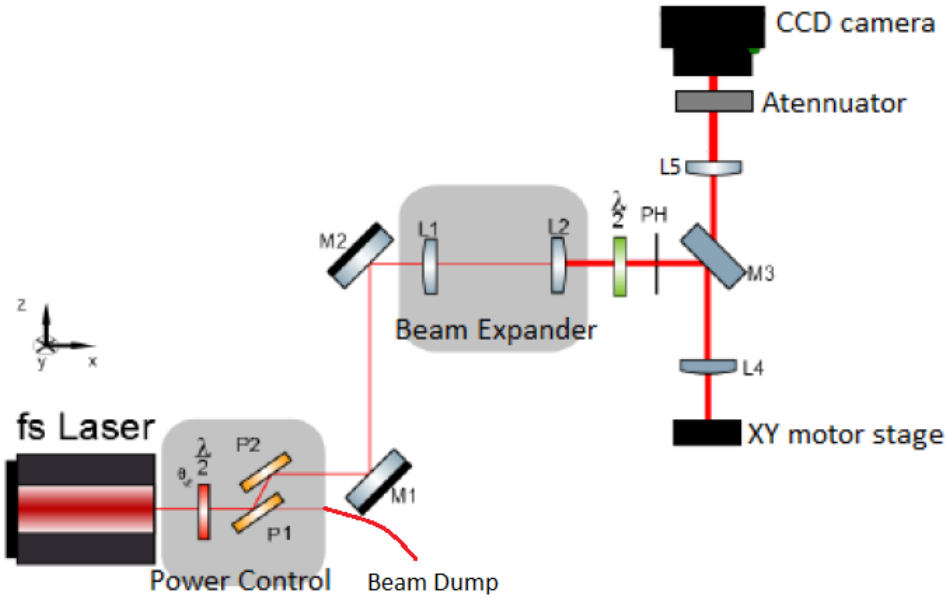

Figure 3.2: Laser direct writing unit.

The magnification is 2.3 and the beam exits the expansion system collimated. After, the beam propagates across a half-wave plate ($\lambda/2$) that determines the beam polarization, aligning it parallel or perpendicular to the writing direction. It is used a variable aperture (PH) to keep the beam diameter and the objective entrance diameter equal.

To choose the objective lens (L4) we first discuss the effects of the numerical aperture. This parameter determines the spot size and thus the spatial resolution achieved; thus high numerical apertures are desirable. However, this leads to low depth of field, so that structures have to be fabricated very close to the surface, and increases the fabrication time when designing structures with bigger dimensions (channels) [12]. On the other hand, at low numerical apertures two non-linear processes may occur: (i) self-focusing which may lead to pulse collapse and (ii) self-phase modulation that broadens the pulse [24]. The objective used has a numerical aperture of 0.55, working distance 2.9mm and entrance aperture 5mm. The lens is aspherical to correct spherical aberrations and to improve symmetry of the fabricated devices. The objective is held in a PI P-725 stage that moves in the Z direction, as defined in figure 3.2, a maximum of 400μm with a 3.3nm resolution.

The sample is held by two stages Aerotech ABL10100 BL assembled orthogonal to each other. The stages move in the XY plane, as defined in figure 3.2, and have a precision of 50nm in positioning and 20nm in reading. All of the stages are controlled by a software program, written in C by Professor Daniel Alexandre (Department of Physics of School of Sciences and Technology of University of Trás-os-Montes and Alto Douro). The same program controls an acousto-optic cell that determines the laser state ON/OFF. The sample is locked in the stages by a vacuum pump.

An image of the reflected light in the sample is recorded in a charge-coupled device (CCD) camera, which enables alignment with better precision.

3.2 Alignment procedure

Firstly, the objective lens is cleaned with acetone and the mirrors are cleaned with an aerosol spray. After, it is verified that the beam leaves the expansion system collimated by checking that the beam diameter does not change at long distances.

The XY stages and the objective holder have to be orthogonal to the beam propagation direction. Therefore, it is placed a mirror on top of the stages and by observing the path of the incident and the reflected beams, we actuate on mirror M3 until the two beams have the same path. We then place the mirror on top of the objective holder, and use the same procedure to align the holder.

With a flat mirror placed in the sample position, the distance between the lens L5 and the CCD camera is adjusted. Given that the beam is collimated, the distance lens-CCD is equal to the lens focal length. This situation corresponds to the observation of a small bright point in the CCD; to avoid image saturation and CCD danification a filter is placed in front of the camera.

The objective L4 is then placed in its holder and aligned along the XY plane, as defined in figure 3.2, so that the beam fills the entire entrance aperture. To that effect, the beam profile is observed after the objective lens and the beam is centered with the objective's optical axis. Plus, we actuate on the variable aperture PH until the beam has a circular distribution. It is important to maintain the same distribution for every experience, to avoid any difference in the power used. In this system it was measured the beam power after the power control unit and after the objective lens; this allowed to quantify the power loss across the writing system in 53%.

Beam power after lens (mW)	Beam power after power control unit (mW)
52.6	111.3
79.2	166.5
105.4	222.0
132.2	276.0
158.4	330.0

Table 3.2: Power calibration.

The polarization state of the beam is controlled manually by placing a polarizer after the half-wave plate and observing the beam profile. When the beam intensity is at maximum, the polarization state is the same as the polarizer axis.

This system may be used to machine slabs and fibers. To write in slabs, the sample is first placed on top of the XY stage and locked by a vacuum pump, so that it remains still during writing. Then, the beam is focused in the sample surface by observing a small bright point in the CCD camera (care has to be taken so the beam power is low enough to avoid damaging the sample surface). The beam may be focused in the top or bottom surface, however focusing in the bottom surface results in a lower intensity on the CCD camera. The sample must be normal to the beam propagation direction; for such we start by focusing the beam in one corner of the sample. By moving the sample along Y, for instance, we level the stage until the observed bright point has the same dimension across the entire length of the sample. Then, the same method is used to level along X.

To machine fibers, first they are cleaned in acetone and then cleaved, and after are

assembled in a home-made sample holder. The fiber core and the laser beam axial positions are aligned by connecting the other fiber end to a broadband source and scanning the fiber along the XY plane until a bright point is observed in the CCD camera. The laser spot is then focused at the fiber tip by scanning the objective lens along Z until the spot observed in the CCD has minimum size. Given the fiber cladding diameter (125μm) no further alignment regarding the orthogonality between fiber plane and laser beam is needed; this condition is assured during cleaving.

The alignment procedure is critical in order to avoid any defects in the produced structures. Common mistakes are illustrated in figure 3.3.

Figure 3.3: Alignment issues: the left picture depicts an optical waveguide placed a few microns from a microfluidic channel, where the waveguide presents a mismatch of 3μm. The right picture shows two curved waveguides with a microfluidic channel in the middle; due to lack of orthogonality between the laser beam and the fused silica slab, the channel is distorted along Z.

3.3 Writing and beam shaping techniques

The writing can be longitudinal, where the scanning direction is the same as the beam propagation direction, or transversal, where the two directions are normal to each other, as shown in figure 3.4 [39].

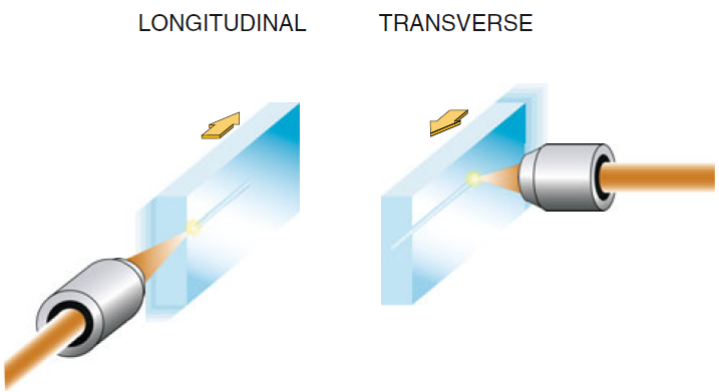

Figure 3.4: Longitudinal and transverse writing configurations [10].

In longitudinal writing, the sample is scanned parallel, either toward or away from the incident laser beam. In this configuration, the resulting structures have cylindrical symmetry, owing to the symmetry of the Gaussian intensity profile of the laser beam. The main disadvantage is that the scan length is limited by the working distance of the lens, which is 2.9mm.

In the transverse writing scheme, the sample is scanned orthogonally relative to the laser beam. The scan length is no longer limited by the lens working distance. This configuration also allows design of more flexible structures with variable shape. However, the scan cross-section is asymmetric (usually elliptical) due to different lateral and axial resolutions [10]. These are related to a difference between beam waist diameter ($2\omega_0$) and confocal parameter (b) given respectively by $\omega_0 = \frac{2\lambda}{NA\pi}$ and $b = \frac{2\pi n\omega_0^2}{\lambda}$, where λ is the wavelength, n the refractive index, NA the numerical aperture and ω_0 the beam waist radius. In typical systems, the ratio between the two varies between 1.8 and 6 (in our system, the ratio is of 4.8).

In this project all the produced structures were written in the transverse configuration. As the aspect ratio of the fabricated structures reflects the energy distribution near the laser focus, the key point in improving the aspect ratio is to modify the energy distribution [12]. Shaping of the focal volume may be achieved by different techniques [10].

The simplest method is by using a slit oriented parallel to the laser scanning direction and placed in front of the focusing lens [21]. The diffraction induced by the slit enlarges the focal spot in the transverse direction enabling design of channels with symmetric cross-section, but wasting most of the laser power. This approach hampers the fabrication of curved waveguides.

An alternative approach consists in scanning different lines with well-defined separation and stacking side by side different laser-affected zones [56]. This method allows obtaining cross-sections with different shapes depending on the application. This solution uses more efficiently the laser power but needs multiple scans and longer processing time. This method was employed for the fabrication of microfluidic channels.

Recently, a spatio-temporal focusing technique has been proposed [26]. The key idea is that by focusing a spatially disperse pulse, the pulse duration increases with distance from the focal plane, reducing the pulse width and maximizing the peak intensity at the focus. This way the peak intensity decreases rapidly when moving away from the focus reducing the confocal parameter of the beam and producing spherical structures. A grating pair is usually used to increase the pulse duration.

An alternative approach is shaping the focal volume by introducing a focusing geometry in which the beam is astigmatically shaped by changing the spot sizes in the parallel and perpendicular planes and the relative positions of the beam waists [11, 57]. The astigmatic beam shaping can be obtained by placing a cylindrical telescope before the focusing objective. This allows one to modify the focal volume in such a way that the cross-section of the laser-affected zone can be made circular and with arbitrary size, making use of all the available laser power.

Crossed-beam shaping may also be employed [12]. The system consists of two orthogonal objective lenses that are positioned so that they have the same focal point. If the two beams temporally overlap at the focus, the focal spot consists of a sphere. The major difficulty is in maintaining the spatial and temporal overlap of the two beams during irradiation.

3.4 Fabrication of optical components and microfluidic channels

The samples used in this work were of fused silica with 2.5mm width, 7.6mm length and 1mm thickness.

Optical waveguides

To produce optical waveguides we use an existent software written in C by Professor Daniel Alexandre (Department of Physics of School of Sciences and Technology of University of Trás-os-Montes and Alto Douro), whose window is shown in figure 3.5. First the sample has to be placed at the position which we want to start writing. The sample is positioned in the XY plane by clicking the arrows X and Y, accordingly. The sample position can be monitored in the 'Position Status' screen: the real coordinates correspond to the real position, while the virtual position give the position coordinates relative to a home position. The home position is defined by clicking the 'Set Home Position' button; this position is usually set as one of the sample edges. There are two ways to set the writing depth: it can be done manually by altering the depth position in the Z stage controller, or it can be done automatically in the 'Manual Focus' program. Because the fused silica sample has a different refractive index than air, the real focused depth z' is given by the sample refractive index times the introduced depth z. For instance, if we which to write at z'=100μm from the sample surface, then the introduced focused depth z is equal to 68.4μm (refractive index of fused silica is 1.45 at 515nm). It is recommended to monitor the depth in an oscilloscope, by connecting a cable from the Z-controller to the oscilloscope.

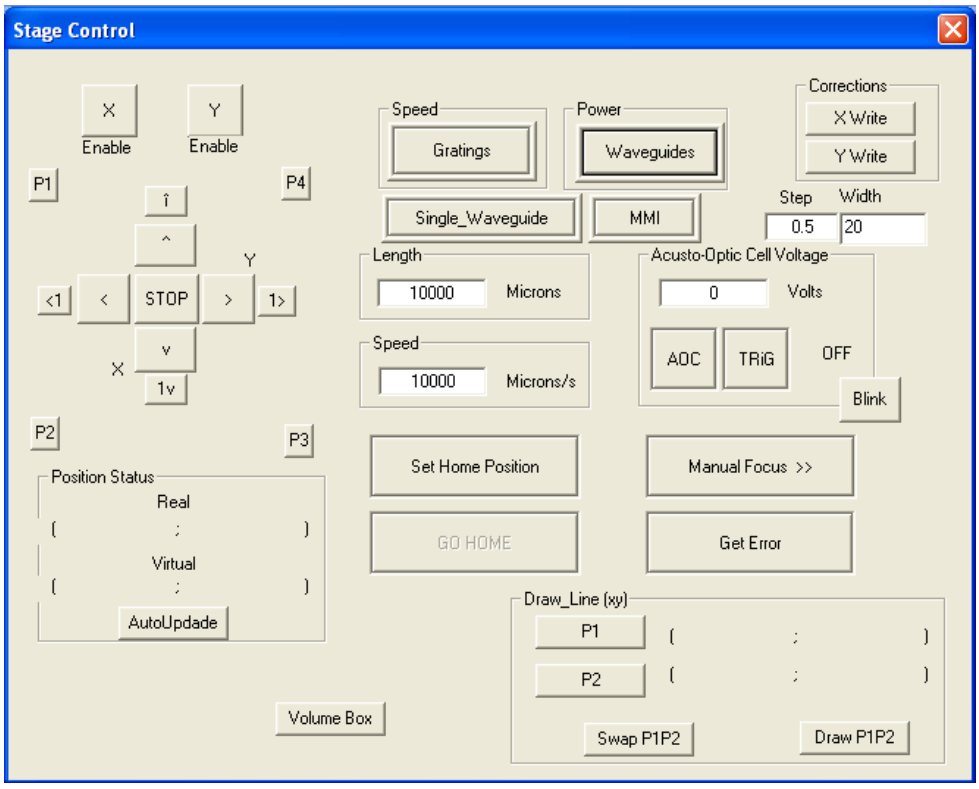

Figure 3.5: Software for writing waveguides.

The waveguide length and the scanning speed are defined in the window 'Length' and 'Speed' which are in units of μm and μm/s, respectively.

To turn the laser on we set the acousto-optic cell voltage to 5V and click in the button 'AOC'; a bright spot can then be seen in the CCD camera. Care has to be taken as the beam may already modify the material properties. Before writing the cell has to be turned off.

On clicking the 'Single_Waveguide' button the cell is automatically turned on and the stage X moves a distance 'Length' along the positive direction, as defined in figure 3.6, and at speed 'Speed'. After writing, the cell is automatically switched off and the stages remain in the final position. The single waveguide geometry is shown in figure 3.6.

An alternative to this latter part consists in closing the 'Stage Control' window and importing and executing a Gerber file that contains the device layout. In this approach, all the writing parameters (scanning speed, pulse energy and scanning depth) are defined as previously, but before closing this window the 'Set Home Position' button has to be pressed. This methodology also enables fabrication of more complex geometries, such as S-bend waveguides, Y-juntions or directional couplers.

Bragg grating waveguides

To write Bragg grating waveguides, the pulse energy has to switch ON/OFF quickly. To this end the laser gate is controlled externally by a function generated in a function generator DS345, from Stanford Research Systems. It is used a square function with a tunable duty cycle (percentage of the period in which the function is at its maximum), where the function amplitude is related to the acousto-optic cell voltage and thus to the pulse energy. According to the Bragg equation the modulation period is given by $\Lambda = v/f$, where v is the scanning speed and f is the square-function frequency. Hence the Bragg wavelength can be tuned by changing the square function frequency or duty cycle or by changing the scanning speed.

Apart from the acousto-optic cell voltage, that in this case is modulated externally, the writing protocol for Bragg grating waveguides is similar to the protocol used for optical waveguides.

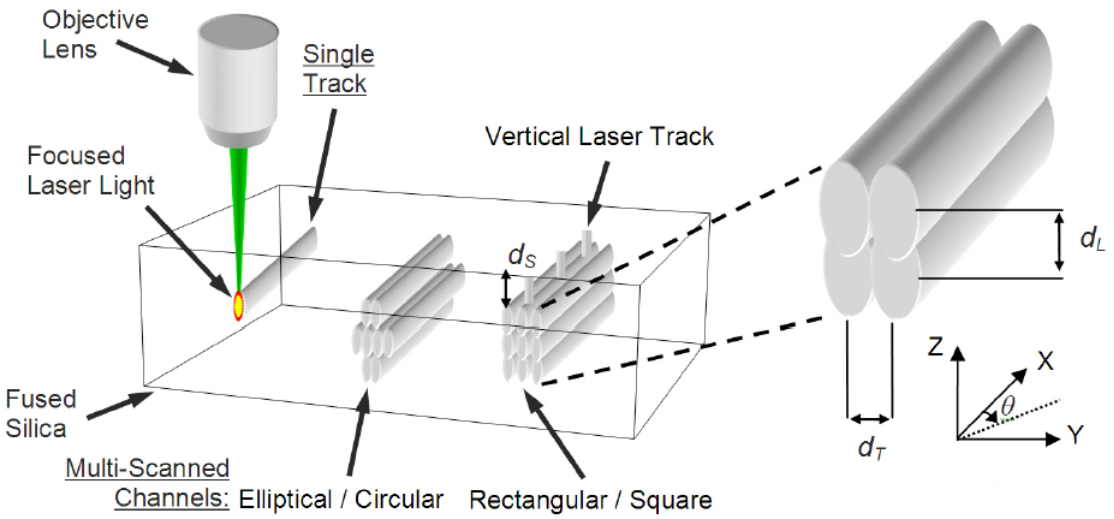

Figure 3.6: Writing technique adopted for fabrication of waveguides, Bragg grating waveguides and microfluidic channels [25].

Microfluidic channels

The multiscanning technique, demonstrated in figure 3.6, consists in stacking and arranging laser-affected zones to define the volume to be etched. This technique is preferred in the fabrication of microfluidic devices, because it allows shaping of the microchannel cross-section. This is important because the shape determines the fluid dynamics and biological function of the microchannel. For example, circular cross sections are preferable for mimicking the environment in blood vessels since rectangular cross sections induce non-physiological gradients in the fluid shear rate, velocity, and pressure [21]. However, they induce a lens effect that distorts cell imaging and damages analysis accuracy [58]. In this work we only produced channels with rectangular cross-section.

To fabricate microfluidic channels we adopted the multiscanning technique. It was necessary to develop a new software to produce such devices; a new program was written in C with the aid of Professor Daniel Alexandre (Department of Physics of School of Sciences and Technology of University of Trás-os-Montes and Alto Douro).

Initially the sample has to be positioned following the procedure described previously for optical waveguides. In this case, however, the Z stage has to be controlled automatically, so the 'Manual Focus' program is used to set the sample depth. Then, the function 'Volume Box' is called. A screenshot is shown in figure 3.7.

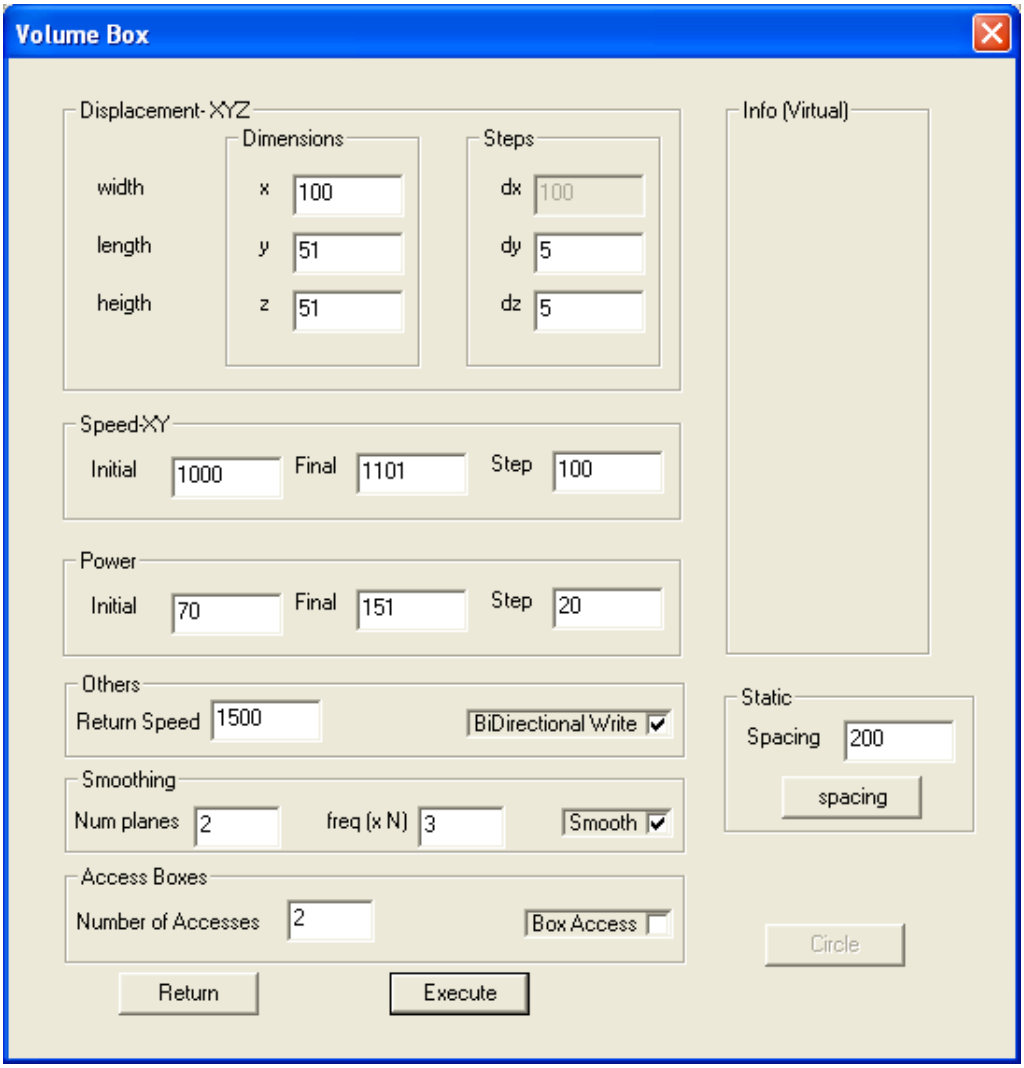

Figure 3.7: Software for writing microfluidic channels.

The 'Displacement-XYZ' panel is related to the channel dimensions (X, Y, Z). The dimensions along X and Y define length and width of the channel respectively, while the dimension along Z defines the channel height. With the technique adopted it is necessary to define the line-to-line separations. Because the scans are written along X, it is only necessary to define the separation dY and dZ. All the mentioned parameters are in units of microns.

Below, the panel 'Speed-XY' defines the scan speed. There are three parameters: initial speed, final speed and step. This approach was used to enable production of channels with similar irradiation conditions apart from the scanning speed. To produce only one channel the sum of the initial speed with the step has to be higher than the final speed value.

Likewise, the panel 'Power' has the same properties and allows to fabricate channels only varying the pulse energy. Because the energy can only be varied in the Altechna software, when passing to the next energy a window pops up asking to change the energy.

The writing procedure can thus be understood as follows: the first channel consists of multiple scans that are written with the initial values of speed and energy. The scans are always performed along the positive X axis, according to the referential of figure 3.6; after each scan the sample is automatically repositioned in the initial position of the first scan. Then, the

sample translates a distance dY along the positive Y axis, according to the referential system of figure 3.6, and the second scan is performed. After writing, the sample returns again to the initial position of the first scan and is then translated a distance 2$\times$dY and the third scan is produced, and so forth until all the scans along Y are made. Next, the sample moves up a distance dZ, as defined in figure 3.6, and another set of scans are made, all at the same depth. This routine continues until all scans are made. We opted to write from the rear surface upwards, as the laser beam is not affected by the already modified surface. Using the alternative method, top-to-bottom writing, the laser beam has to cross already modified volume which leads to scattering and distortion of the laser focus, resulting in strong disordering and interruptions in the produced nanostructures [29].

After fabricating the first channel the sample translates a distance 'spacing' along the positive Y axis. This parameter varies between 0μm and 500μm and is defined as the distance between the first scan position of each channel. Then the speed is increased by a factor 'step' and the second channel is written. This procedure occurs until all the speeds are used. Then the sample translates again, but now a distance of 2$\times$'spacing' and the program asks to change the energy in the Altechna controller. After changing the energy a new channel is written. When all the set of speeds are used, the program asks again to change the energy. After all the combinations of speeds and energies are used, the sample is automatically positioned in the initial position of the first channel and the program ends. The sample coordinates, relative to the position in which the first scan is written, are indicated in the 'Info (Virtual)' panel and it is recommended to keep an eye on this to check if the channels are being written at the right position.

There are a couple of options that can be activated. If the bidirectional writing option is used then after writing the first scan, the sample translates a distance dY and the second scan is written along the negative X axis. This allows to save some time, but may induce a quill effect.

The option access box enables fabrication of multiple channels with the same dimensions and written at same speed and energy. In this case the spacing is defined along the X axis and not along the Y axis. It is also necessary to indicate in 'Number of Accesses' the number of channels to be written. The channel dimensions, the scanning speed and the pulse energy are defined as before.

The smoothing option is used to write the bottom and the top of the channels with different separation along Y. There are two parameters: number of planes and frequency. The first defines the number of planes along Z that are to be smoothed. The parameter dY is divided by the value 'freq', which gives the new separation with which the top and bottom planes are written.

We also define a return velocity to reposition the sample (usually 5000μm/s) which helps in stabilizing the writing system, avoiding writing of undulated lines. On clicking the execute button, the channels are written.

The etching is done in the MNTEC cleanroom facilities by immersing the sample in an HF solution with a concentration of 10%. We opted for this concentration as it allows to obtain high etch rate and high selectivities. In addition, we perform the etching in an ultrasound bath (Branson 2510 Ultrasonic Cleaner) at frequency 40kHz to speed up the etching reaction and to facilitate debris removal. After etching the chemical reaction is stopped by immersing the

sample in deionized water. The sample is then dried with a nitrogen gun. To remove any remaining debris the sample can be rinsed in ultrasonic bath in a solution of isopropanol and then of deionized water.

The microfluidic channels after etching present surface roughness that may disturb fluid flow and integration with optical layers. The channel surface may be smoothed by performing a post-etching procedure with low HF concentration (1-2%) [29] or by performing heat treatment (annealing with oxyhydrogen flame [59, 60] or CO_2 laser reflow [61]), where the glass is almost melted so that the surface tension can level the channel irregularities. However, CO_2 laser reflow can only be employed if the channels are produced at the glass surface and fused silica is annealed at temperatures around 1200°C.

3.5 Polishing

Spherical aberration at the glass-air interface becomes significant at higher scanning depths producing a border effect in which light is scattered at the edge causing a depletion of the laser power delivered to the focus and producing a wider modification volume [62]. This effect is undesired leading to high optical losses. Therefore after laser direct writing the samples are polished. This procedure also enables microscope observation and characterization of the cross-section of the produced structures.

The adopted polishing procedure is as follows:

• Heat a piece of dull glass polished on one side and the sample on a hot plate at 100°C-150°C;

• Spread the bonding wax over the glass and wait until the wax is in liquid state;

• Place the sample over the support glass carefully to avoid bubble formation;

• Align the two borders of the sample with the help of a glass slide;

• Turn off the hot plate and wait until the wax solidifies (after solidification remove the alignment glass);

• Clean the holder in water to remove residuals from former polishing, and place it for around 10 minutes in the first plate with Silicon Carbide;

• Place the sample in the holder and fix it carefully, so that it is not subject to high pressure;

• Clean the holder and the sample with water;

• Make sure that the first polishing plate, with Silicon Carbide, is wet to avoid abrasive polishing;

• Place the support in the rotating plate not letting the glass touch the plate; start the rotating plate with mild speed and slowly release the glass to avoid crack formation;

• Release the spring completely and set the following polishing parameters: plate speed 20rpm and 2 drops of powder per plate cycle; make sure that the support rotates around its axis (the sample movement should be as random as possible to increase polishing uniformity); to increase polishing quality at the glass edges, the plate speed may be lowered;

• Remove the holder, clean the glass surface and observe the edge on the microscope: if the surface is uniform pass on to the following polishing plate;

• Before placing the holder in the second plate, clean the glass surface with water to avoid contamination;

• Repeat the same procedure as before to the second plate; the second powder is aluminum oxide;

• When the glass surface is uniform pass on to the last plate, which is formed by Logitech polishing suspension type SF1;

• The polishing is complete when the glass surface is uniform and crack free;

• Remove the set “support glass + sample” from the holder and place it in the hot plate, at a temperature of 100°C-150°C;

• When the bonding wax is liquid remove the sample from the support glass carefully, to prevent the wax to contaminate the polished edge;

• Remove the wax from the sample with paper, making sure that the glass is at high temperature;

• Clean the sample in piranha solution, and then with ethanol and acetone in ultrasonic bath, and rinse the sample in deionized water.

3.6 Optical layers characterization

3.6.1 Optical waveguides

The produced optical waveguides are characterized by measuring the propagation losses. The propagation loss (PL) inside the waveguide is determined from the formula $PL = IL - 2CL$, where IL is the insertion loss and CL is the coupling loss. The insertion loss can be seen as the total power loss across the system, while propagation losses only account for dispersion and scattering inside the waveguide. Coupling losses are due to differences between the optical fiber and waveguide mode profiles.

The used set-up to measure insertion loss is depicted in figure 3.8. A Santec TLS-120 tunable laser is used as source and the Exfo IQ-1640 is used as a power meter.

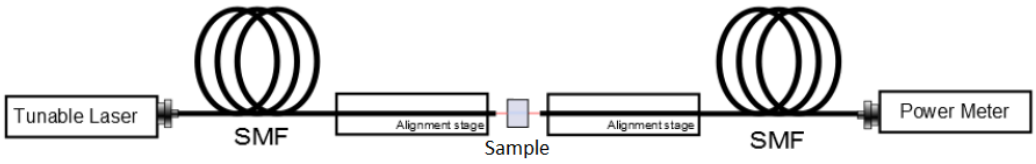

Figure 3.8: Experimental set-up for measuring insertion loss [38].

Laser light propagates across SMF fibers that are butt coupled to the sample by aligning each of the fibers ends, mounted on precision stages (Elliot Scientific E2100), with the respective waveguide facet. The precision stage piezo-controller allows easy, precise, and stable alignment.

The insertion loss is calculated according to the formula $IL = -10log(\frac{P_1}{P_0})$, where P_0 is the tunable laser power (incident power) and P_1 is the power measured in the power meter (transmitted power). To check if the laser power changes over time, it is used a 90-10 coupler

placed after the tunable laser, where 90% of the power is transmitted to the SMF fiber and the remaining 10% are used to guarantee stability.

To measure the waveguide mode profile we use the experimental set-up shown in figure 3.9. From the measured profile we trace the beam intensity profile that can be related to the coupling efficiency and the coupling loss [63].

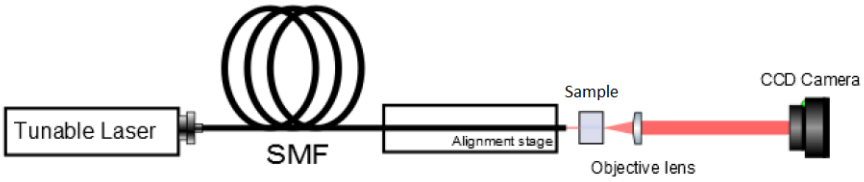

Figure 3.9: Experimental set-up for characterization of waveguide mode profile [38].

During measurements, index matching oil is used at the fiber-waveguide interfaces to decrease Fresnel reflections and improve measurement accuracy.

The protocol used to produce low-loss single-mode optical waveguides with the same fabrication apparatus was defined by a colleague of mine [64]. In order to minimize propagation losses, several waveguides were written by changing the irradiation conditions: beam polarization (parallel and perpendicular to the scanning direction), scanning depth (50μm to 250μm), scanning speed (100μm/s to 500μm/s) and pulse energy (100nJ to 300nJ). The obtained results for perpendicular polarization are presented in figure 3.10.

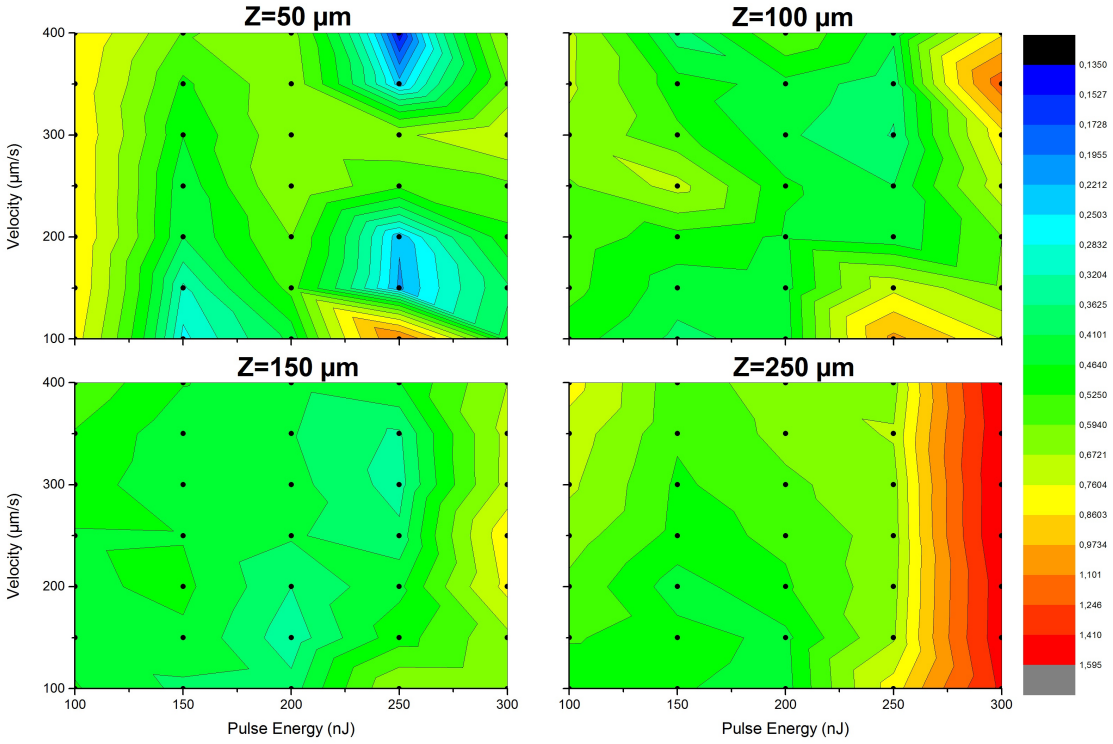

Figure 3.10: Propagation losses (courtesy of Vítor Amorim [64]).

It was determined that waveguides written with perpendicular polarization had higher

propagation losses. In addition increasing the sample depth increased losses, possibly due to spherical aberrations that damage waveguide quality. Scanning speed did not possess a big influence in the waveguide quality, while higher energies yielded lower losses. Waveguides with propagation losses as low as 0.14dB/cm were obtained under the following conditions: parallel polarization, 250nJ pulse energy, 400μm/s scanning speed and 50μm scanning depth.

3.6.2 Bragg Grating waveguides

To characterize the gratings we use the set-up depicted in figure 3.11. The laser broadband source used is an EXFO IQ-2300 ASE and for powermeter it is used an optical spectrum analyzer (OSA). By introducing the circulator we can measure the reflected or the transmitted power spectrum on the OSA. After the laser source, a polarization control unit (Thorlabs ILP1550PM-APC) can be employed that allows measurement with horizontal or vertical laser incident field.

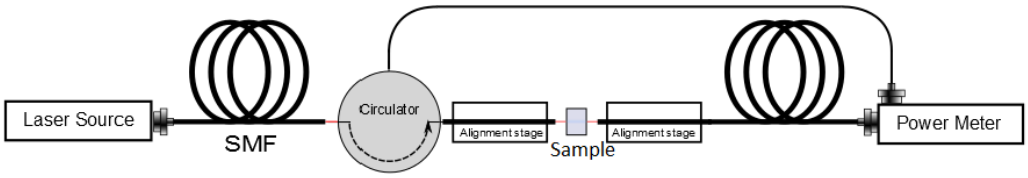

Figure 3.11: Experimental set-up for characterization of Bragg grating waveguides [38].

The reflected Bragg wavelength is determined by reading at the OSA the wavelength at which the maximum/minimum peak power occurs (for reflection and transmission measurements respectively). This allows to calibrate the writing parameters in order to tune the Bragg wavelength.

From the OSA spectrum we can also obtain the grating strength that is defined as the difference between peak power and reference level (power for a wavelength much higher/lower than the reflected wavelength). The grating strength is related to the reflectivity, that should be as high as possible.

To measure birefringence we use the polarization control unit. The birefringence is calculated as the difference between Bragg wavelengths obtained for horizontal and vertical incident field.

The obtained results regarding grating characterization were obtained by Vítor Amorim [64] and are presented in figure 3.12. The gratings were produced under the optimum irradiation conditions obtained for optical waveguides; the square function frequency is 746.129Hz and the duty cycle was varied between 10% and 90%.

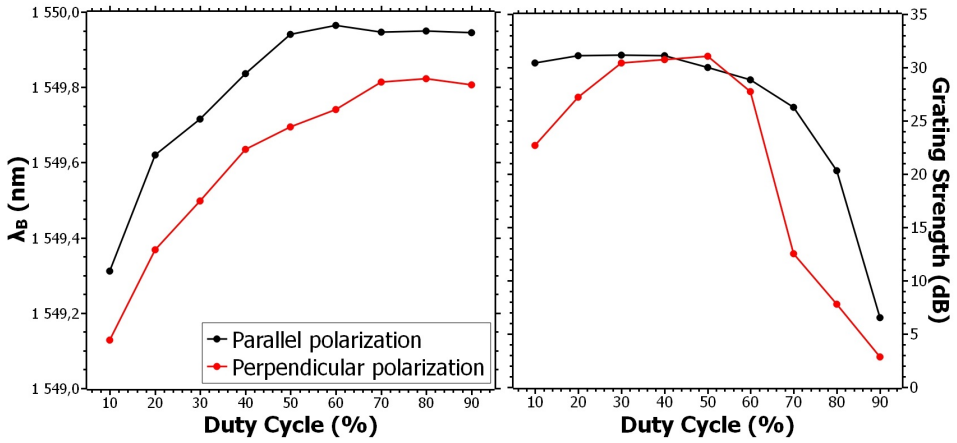

Figure 3.12: Bragg wavelength (left) and grating strength (right) as a function of the duty cycle and the beam polarization (courtesy of Vítor Amorim [64]).

It is observed that the Bragg wavelength depends on both the beam polarization and on the duty cycle. In particular, increasing the duty cycle from 10% to 50% results in a proportional increase of the Bragg wavelength. From 50% upwards the reflected wavelength remains constant. Figure 3.12 left also indicates that varying the duty cycle does not seem to change birefringence. To produce gratings to operate at 1550nm (telecommunications wavelength), the beam polarization should be parallel to the scanning direction and the duty cycle should be at least 50%.

From figure 3.12 right we conclude that the grating strength remains constant at 30dB for duty cycles lower than 60%, and from then on it decreases abruptly. We also observe that the grating strength is usually higher for parallel polarization, except in the range 40% to 60% where the grating strength seems to be independent of the beam polarization.

To obtain strong gratings operating at the telecommunications wavelength, the gratings are produced with parallel polarization and with a duty cycle of 50%.

Chapter 4

Fabrication of Integrated Components and Devices

In this chapter the results obtained during the project are presented. First, we expose the preliminary results obtained in the first semester as a preparation for this work. These results were crucial for testing the writing software and to decide on the most appropriate etching procedure.

Then, we optimize the fabrication process of microfluidic channels in order to obtain channels with high and uniform aspect ratio (length over cross-section dimension) and with smooth sidewalls. The influence of the various irradiation parameters (pulse energy, beam polarization, scanning speed, scanning direction, scanning depth) on the etch rate of single and multi-scan channels is discussed. An analysis of the surface roughness of the channels as function of these parameters is also provided. Problems regarding the fabrication of microfluidic channels, such as tapering, are described and the solutions adopted to solve it are discussed.

After this study, we move on to integration of optical layers and microfluidic channels in the same platform. Two different optical detection schemes are presented and its principle of operation is discussed in detail. Some issues regarding the fabrication of these devices are also analyzed.

The FLICE technique employed to fabricate channels in silica slabs can be also applied to optical fibers, with the purpose of producing fiber-based sensors. Some exploratory work on this subject is presented at the end of the chapter.

4.1 Preliminary results

In these tests we produced several channels, buried in the sample at a depth of 40μm from the sample surface, with dimensions 150x150x20μm^3. The channels were written with perpendicular polarization and at different pulse energies and scanning speeds ranging from 100nJ to 300nJ and 100μm/s to 200μm/s, respectively.

Initially, we performed the etching reaction without ultrasounds. Observations at an optical microscope revealed the existence of bubbles within the channel as seen in figure 4.1 left. Thus we decided to start performing the etching in an ultrasound bath that proved to fix this issue. In

addition, ultrasounds facilitate debris removal [57].

In the first tests we performed the etching in an HF solution with a concentration of 49%. After the etching reaction, the initially buried channels are now at the silica surface, because the HF acid etches the top pristine layer. Therefore, we are able to measure the channel height at a profilometer (Profilometer Dektak XT from Bruker; stylus with 2μm radius and with 3mg applied force). We observed that after 10 minutes of etching the entire channel had been etched. Despite this high etch rate of the laser-affected zones, we determined the pristine etch rate to be 2μm/min, under these experimental conditions. The pristine high etch rate indicates that with high acid concentrations we can not control the box dimension with sufficient precision. Although increasing fabrication time, lower HF concentrations are therefore desirable. In addition it has been shown that lower acid concentrations enhance etching selectivity [9], and hence we opted for an HF concentration of 10%.

Figure 4.1 left reveals another important feature: the scanned lines are undulated due to XY stages instability. These channels were produced with a stage settling time of 0.1s that does not allow the XY stages to stabilize and thus when a scan is written the stages are still oscillating. To prevent this effect, the stages settling time was increased to 1s.

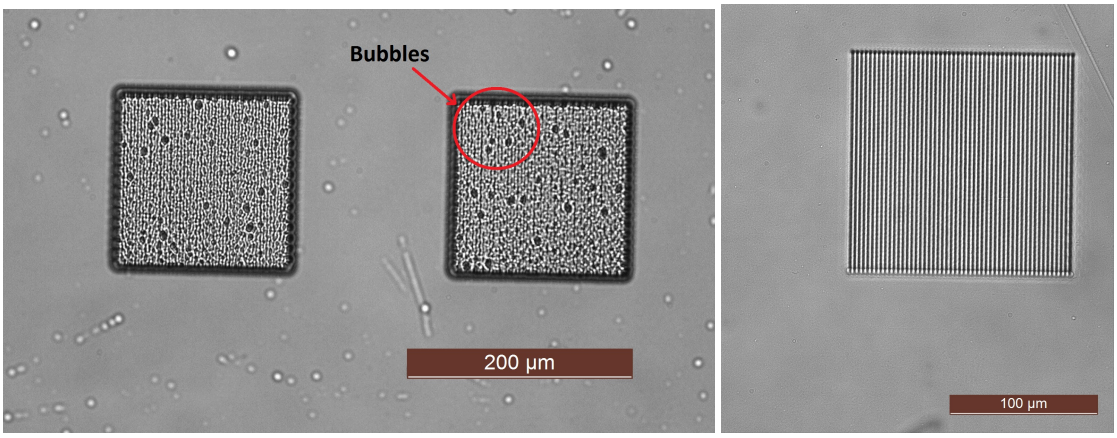

Figure 4.1: Preliminary results: the left picture depicts an open channel (at the sample surface) with bubbles and with undulated scanned lines; the right picture depicts a channel with the XY stages stable.

The approach presented above for calculating the etch rate by measuring the channel height on a profilometer presented some issues. First, an acid concentration of 10% only etches the pristine at 0.13μm/min and thus the time necessary for the acid to reach the channel is of hours. Second, this approach would not allow to infer the scanning depth influence on the etch rate. Third, the etched length would be measured in a profilometer which restrains the channel dimensions: channels with dimension around 150μm needed to be produced which significantly increasing fabrication time. Given these problems we opted to write channels starting at one of the glass facets, thus enabling acid diffusion; this way we could measure the etch rate by direct observation on a microscope.

The channels may be fabricated directly buried on the glass or at its surface. In the latter, no practical limitations exist on the channel length and on the design geometry, but the sample has to be subject to an additional sealing process [65]. Fused silica can be sealed against a

PDMS slab as described previously or by anodic or fusion bonding which requires application of high pressures, temperatures and voltages and may damage the channel structure. It may also be sealed against a glass slab by femtosecond laser welding [66].

Directly buried channels however are more appealing since it avoids sealing and exploits the three-dimensional capabilities of the FLICE method. This approach, however, is faced with limitations in channel length and aspect ratio, since in the etching reaction the HF acid is unable to reach the channels end, generating a tapered channel. To overcome this issue we use a writing technique proposed by Ho et al [25] where we fabricate access holes connecting the buried channel to the sample surface, as will be discussed later.

These results were important as it proved that the writing software was working correctly and it allowed us to determine the right geometry for etch rate measurements and the right etching conditions (HF concentration of 10% and etching in ultrasounds).

4.2 Etch rate

The FLICE technique allows fabrication of microfluidic channels directly buried in the glass substrate with flexible geometry. The first step towards this end is in understanding the etching process and how it is influenced by the exposure conditions (pulse energy, scanning speed, beam polarization, scanning depth and scanning direction), as it is the etch rate that defines the aspect ratio [25]. Therefore, single-scan channels were produced in fused silica by varying the irradiation conditions, polished and etched for 8 non-consecutive minutes in an ultrasonic bath with HF10%. The channels were written by scanning outside to the inside of the glass and were formed with perpendicular and parallel polarization, with pulse energies between 60nJ and 300nJ, scanning speeds between 100μm/s and 500μm/s and scanning depths between 50μm and 150μm. The effect the line-to-line separation has on etching of multiscanned channels was also examined. A typical example of a sample is shown in figure 4.2.

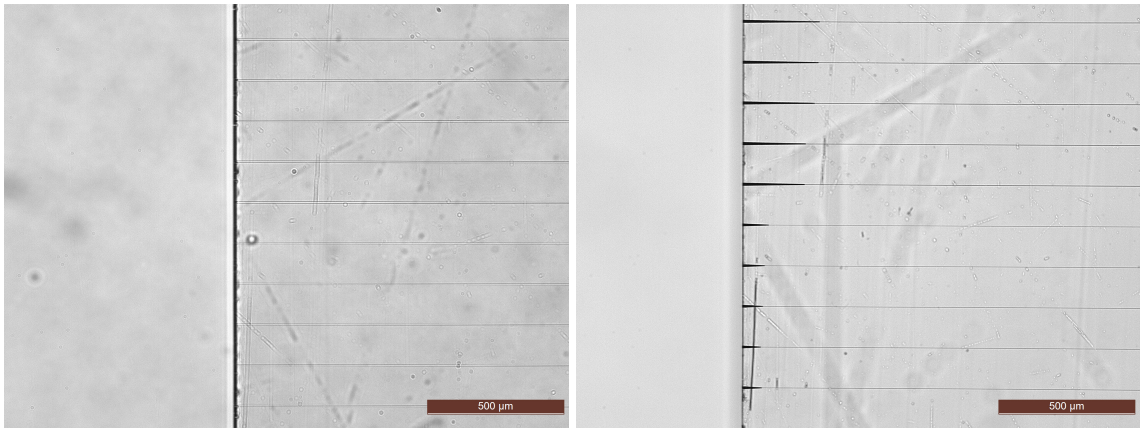

Figure 4.2: Top view of single-scan channels after laser direct writing (left) and after 60 minutes of etching (right).

The etch rate is measured by observation on an optical microscope. Prior to etching, when observed at the microscope the channel consists of a white line. If the channel is formed in depth with its entrance only in one of the glass facets, than the HF acid diffuses only through this facet.

Observing the etched channel on the microscope it appears now as a dark line, corresponding to a hollow cavity. The etch rate is then calculated by dividing the dark line length by the etching time. In practice the etching is done in small steps of two minutes, after each the etched line length is measured, and the etch rate is obtained by performing a linear fit. This way a much more accurate representation is obtained and tapering and saturation effects can be analyzed.

Energy

For single-scan channels written with perpendicular polarization (scanning direction orthogonal to the beam polarization) we observed two distinct features. At scanning depths of 100μm and 150μm, the etch rate was practically constant (equal to 18μm/min) throughout the pulse energy range tested, figures 4.4 and 4.5.

At a depth of 50μm, figure 4.3, the damage tracks are not well defined for a pulse energy of 60nJ resulting in a low etch rate around 6μm/min. Increasing the pulse energy to 100nJ results in an increase of the etch rate up to 16μm/min. Continuing increasing the pulse energy does not imply a variation in the etch rate, similar to what was observed at higher scanning depths.

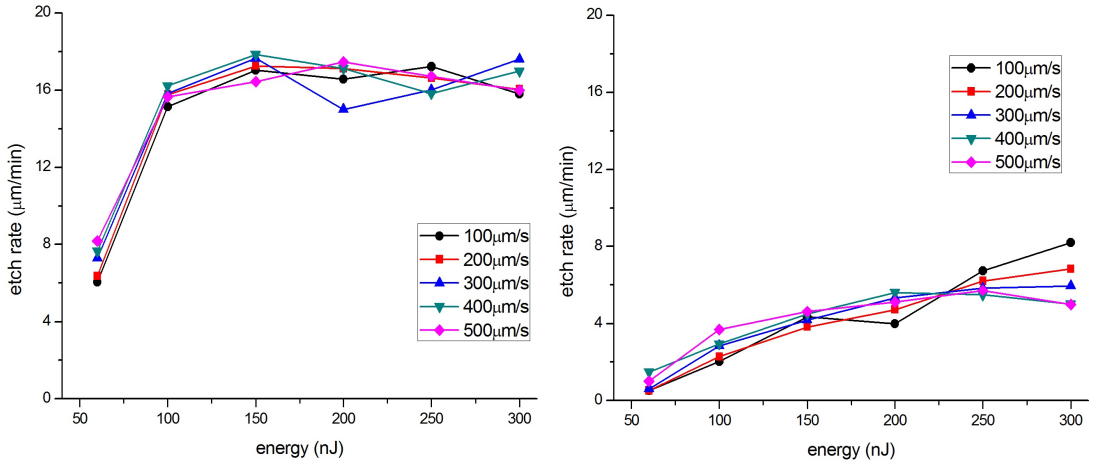

Figure 4.3: Etch rate vs energy of single-scan channels written at depth of 50μm (left - perpendicular polarization; right - parallel polarization).

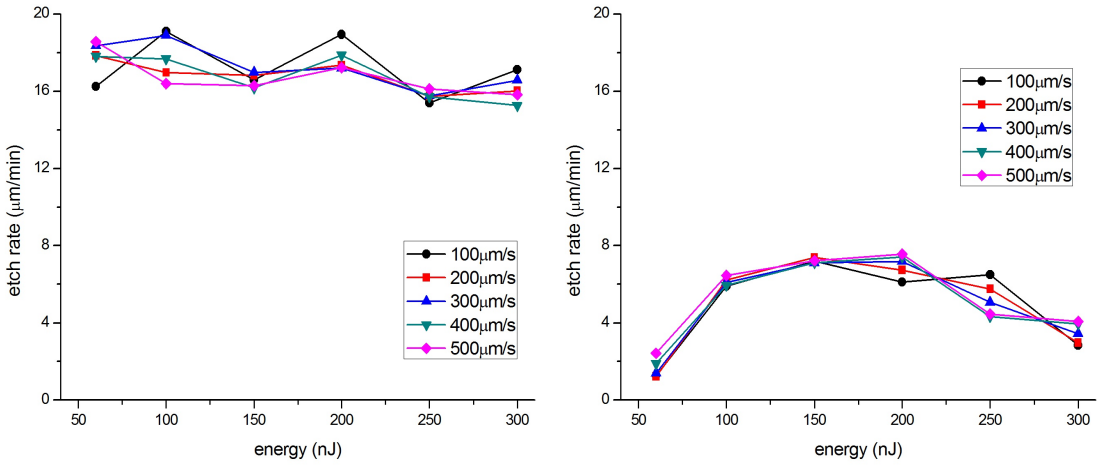

Figure 4.4: Etch rate vs energy of single-scan channels written at depth of 100μm (left - perpendicular polarization; right - parallel polarization).

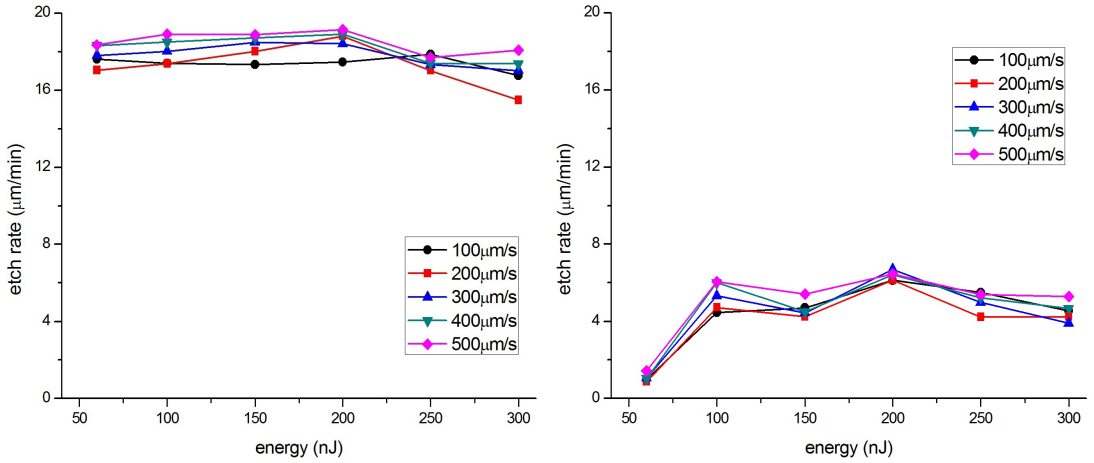

Figure 4.5: Etch rate vs energy of single-scan channels written at depth of 150μm (left - perpendicular polarization; right - parallel polarization).

In the waveguides written with parallel polarization (scanning direction parallel to the beam polarization) we observed different trends depending on both the scanning depth and on the pulse energy. At a depth of 50μm, the etch rate increases linearly with the pulse energy, from 1μm/min to 6μm/min. For a scanning depth of 100μm, the etch rate increases in the range 60nJ to 100nJ. Then it remains constant (approximately 6μm/min) throughout the 100nJ to 200nJ range. Continuing increasing the pulse energy to 300nJ, the etch rate decreases. This decrease is unexpected and may be due to impurities present in the material or due to polishing.

At a higher scanning depth of 150μm, the etch rate increases from 60nJ to 100nJ and then remains constant. Again, at a low pulse energy there is not a high contrast between the exposed and unmodified region. Therefore, a 60nJ pulse energy is our system threshold for formation of nanogratings and generation of selective etching.

The average etch rate for perpendicular polarization is of 18μm/min, while for parallel polarization the etch varies from 0.5μm/min to 8μm/min. Thus we obtain a considerable contrast of 36:1. This result follows from the nanogratings formation model. For perpendicular

polarization the nanogratings align with the channel axis facilitating acid diffusion, while for parallel polarization they form stop layers blocking the etching reaction. Higher differential rates may however be obtained by changing the etching conditions and irradiation conditions (repetition rate).

Comparing the maximum etch rate obtained (18μm/min) to the etch rate of unmodified glass (0.13μm/min) we obtain a selectivity of 140:1, indicating that channels with high aspect ratio may be produced.

Speed

Examining the etch rate as a function of the scanning speed we do not observe any significant change in the range tested (100μm/s to 500μm/s) for both parallel and perpendicular polarizations and at different scanning depths. It is expected that at higher speeds (above 500μm/s) the etch rate decreases, because the contrast between nanogratings and pristine is not as strong.

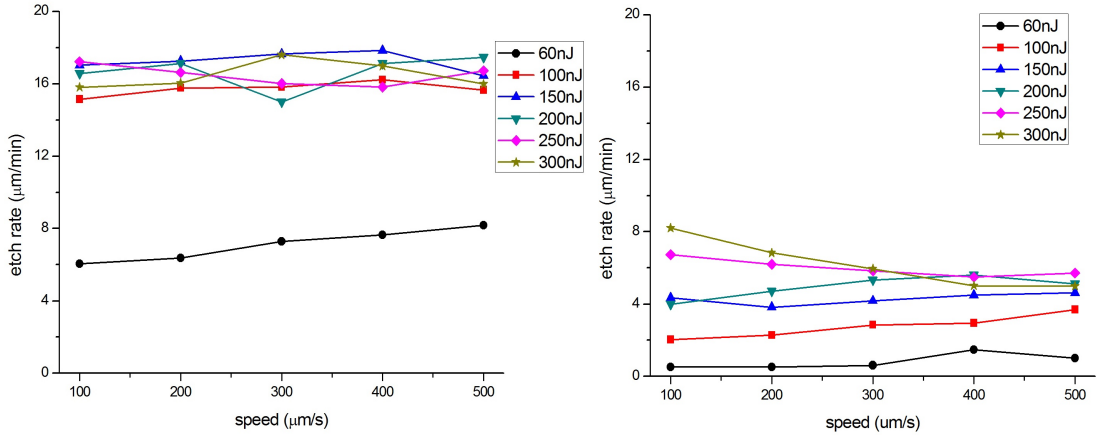

Figure 4.6: Etch rate vs speed of single-scan channels written at depth of 50μm (left - perpendicular polarization; right - parallel polarization).

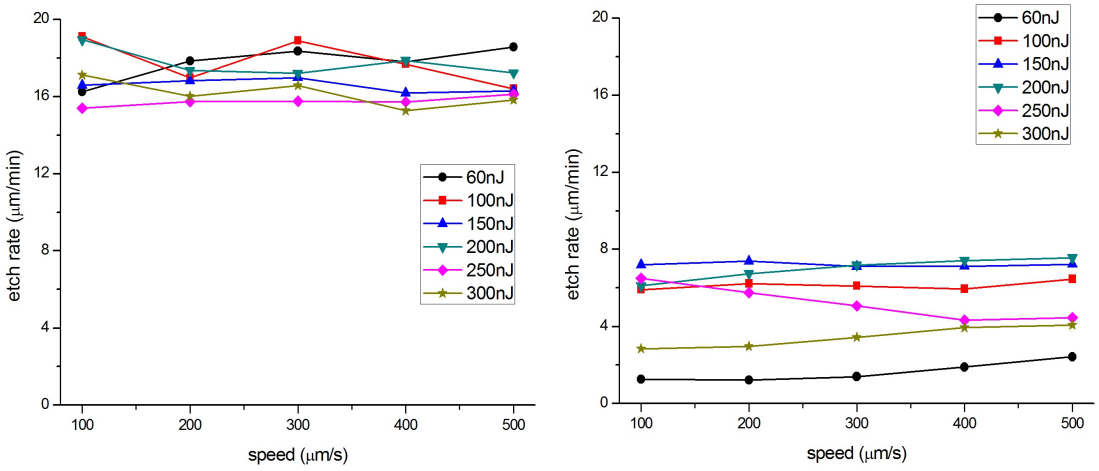

Figure 4.7: Etch rate vs speed of single-scan channels written at depth of 100μm (left - perpendicular polarization; right - parallel polarization).

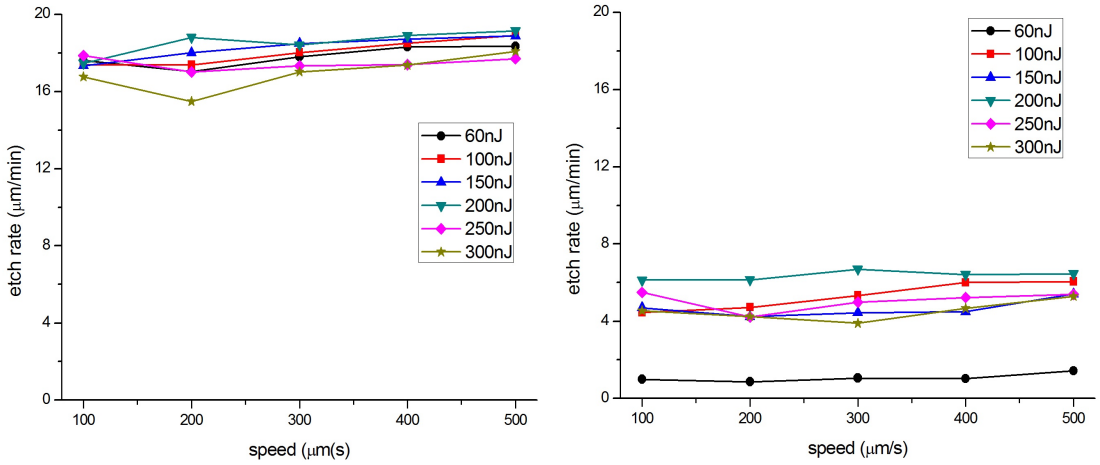

Figure 4.8: Etch rate vs speed of single-scan channels written at depth of 150μm (left - perpendicular polarization; right - parallel polarization).

Polarization angle

To examine the influence of the angle between beam polarization and scanning direction, we wrote single-scan channels changing the scanning direction from -45° to 45° relative to the glass facet and with beam perpendicular and parallel polarization. This way, we can determine the etch rate as function of the polarization angle (0° and 180° corresponds to parallel polarization and 90° to perpendicular polarization, as defined previously). The waveguides were written at 500μm/s with 60nJ pulse energy and at depths of 100μm and 150μm.

The results are shown in figure 4.9. We conclude that the etch rate is strongly dependent on the polarization angle, increasing abruptly at around 70° and peaking at 90°, when the nanogratings are aligned with the channel axis. In addition, there is a strong contrast between the etch rate obtained at 90° and 82° of almost 10:1. Thus to take advantage of a maximum etch rate, the polarization angle has to be accurately oriented normal to the scanning direction.

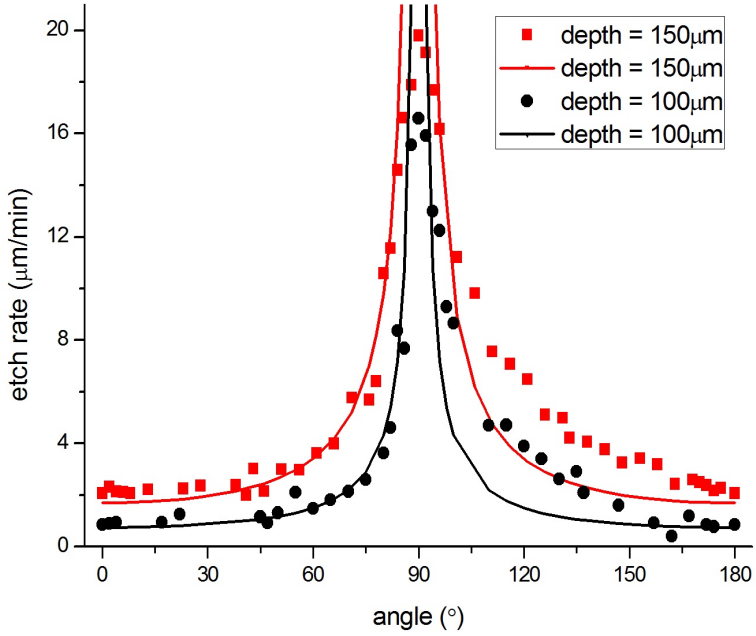

Figure 4.9: Etch rate vs polarization angle of single-scan channels.

Theoretically the etch rate (R) should change with the nanogratings orientation according to the relation $R = R_{\parallel} sec(\theta)$ [25] , where $R_{\parallel}$ is the etch rate at parallel polarization and θ is the angle between scanning direction and beam polarization. The predicted secant lines shown in figure 4.9 closely match the experimental data in the 0° to 90° range. As for the 90° to 180° range we observe an increase in the etch rate. Due to the symmetry of nanogratings alignment this results are not expected, and may be owed to the etching set-up.

Increasing the scanning depth seems to increase the etch rate for channels written with parallel polarization. This is due to a spherical aberration effect that is enhanced at higher depths and decreases the contrast between irradiated and non-irradiated zones. Therefore the less well-defined nanogratings, orthogonal to the channel axis, are not as effective in blocking HF propagation causing an increase in the etch rate.

The channels may also be produced with circular polarization, which was not tested in our system. Although it produces disordered nanostructures, this approach is important to produce curved channels [29].

Scanning direction

The quill effect can be described as a tilt in the pulse front wave that changes the morphology of the volume irradiated by the femtosecond laser. Experimentally this effect can be observed when changing the scanning direction (writing towards the glass or away from the glass) by SEM microscopy. When writing an optical waveguide away from the glass, the surface of the exposed volume appears more damaged and the formed waveguide has higher transmission losses than when written in the opposite direction.

Here, we fabricated single-scan channels changing the scanning direction, the beam polarization (parallel or perpendicular to the scanning direction), and the pulse energy from 60 to 300nJ. The scanning depth and speed were 100μm and 500μm/s, respectively. Then, the

facet containing the waveguides was polished and the sample was etched for 10 minutes with HF10% in an ultrasonic bath.

We observed at an optical microscope that the channel's etched length was the same for channels written with the same irradiation conditions but with opposite scanning directions. Thus quill effect was not observed in the tested conditions. Other groups [67] showed that this effect is only observable at higher pulse energies thus validating our findings.

These results are important for fabrication of channels using bidirectional writing, thus reducing fabrication time.

Etching saturation

If we continue the etching reaction for longer than 8 minutes we start observing a saturation effect, meaning that the etch rate starts decreasing with time. As the channel etched length grows, the HF acid can not reach the channel's end as easily and thus the etch rate decreases. This effect depends on the channel length; hence the saturation effect happens first and is more significant for channels written with perpendicular polarization. Figure 4.10 left shows the etched length as a function of time for single-scan channels written with perpendicular and parallel polarization.

We calculated the derivative of the etched channel length results as function of time, thus determining the etch rate. The results obtained are depicted in figure 4.10 right. Clearly it is seen that for perpendicular polarization the etch rate decreases from 35μm/min to almost 6μm/min after just 20 minutes of etching. At this time the channel length is 250μm, thus this effect hampers the fabrication of long microfluidic channels.

For parallel polarization, we calculate an etch rate of 3.88μm/min throughout the entire etching reaction. Although the etch rate is constant during the entire process, the final channel length is 200μm, hence the fabrication time severely increases. In addition the etching selectivity between channels written with parallel polarization and pristine is as high as 10:1.

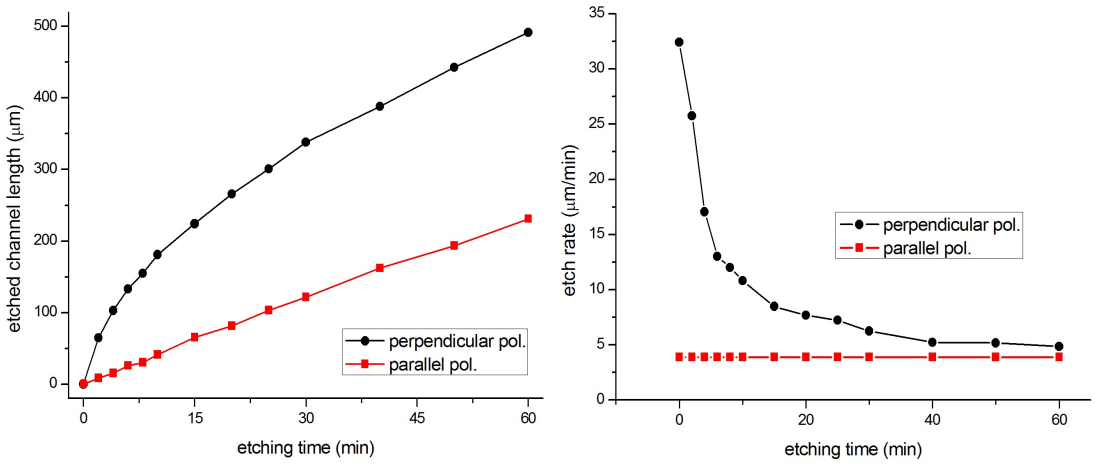

Figure 4.10: Etch rate saturation. The left picture shows the etched length of single-scan channels produced at a depth of 150μm with perpendicular polarization at 500μm/s and with 100nJ pulse energy (black), and with parallel polarization at 300μm/s and 300nJ (red). The right picture is the time derivative of the etched channels length.

Although the pristine etch rate is much slower (0.13μm/min in HF10% solution and in ultrasonic bath), it has an important effect for longer etching times, as it increases the channel dimensions. This process, alongside the saturation effect contributes to producing tapered channels which are undesirable as they damage the aspect ratio. In figure 4.11 we show an example of such a channel, where the apex angle (angle formed by the channel end, as seen from top) is measured to be 0.75°. Although this value is small, the presented channel has a length of 400μm and for many applications the channel length needs to be 1-2cm, thus higher tapering angles are easily obtained.

Therefore this effect hampers the fabrication of long microfluidic channels with high aspect ratio. Solutions to this problem include: (i) use of KOH at 80°C as an etchant, (ii) design of a structure compensating and balancing the etching effect and (iii) fabrication of access holes for acid diffusion connecting the channel to the sample surface. In this project we opted for the third solution as it will be shown later [25].

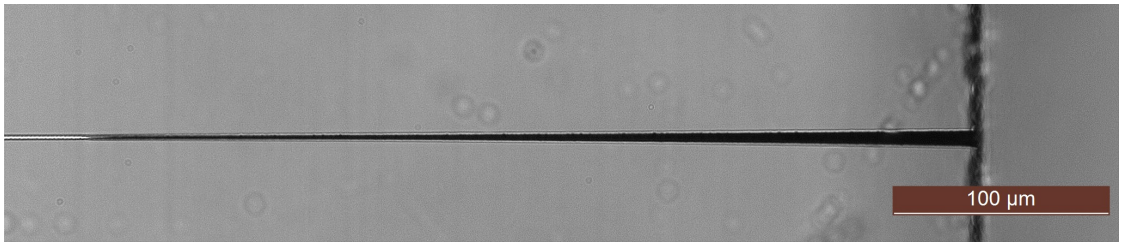

Figure 4.11: Tapered single-scan channel fabricated with perpendicular polarization at a depth of 50μm, with a pulse energy of 60nJ and scanning speed of 500μm/s.

Multiscanning - fabrication of wider channels

While the fabrication of single-scan channels was useful to give some insight into the etching process and for calibration purposes, real channels require multiscanning, which was the next step. In particular, it was necessary to study the influence of scan separation as adjacent multiple laser affected zones can affect the etching process, by modifying the stress field and the density profile of the irradiated volume.

When fabricating channels with parallel polarization, 50μm below the surface at 200μm/s and with line-to-line separations of 1μm along Y and 2μm along Z, we observed an increase in the etch rate from 2.5μm/min at 100nJ to 13μm/min at 300nJ. A similar result had been observed for single scans. Although we were able to obtain an etch rate of 13μm/min similar to what is determined for perpendicular polarization, the resulting channel presented cracks, hindering the use of parallel polarization for channel fabrication.

We also measured the etch rate for channels written with perpendicular polarization, 150μm below the sample surface at 500μm/s and with 60nJ pulse energy. For separations of 1μm along Y we measured a maximum etch rate of 24μm/min, that decreased to 18μm/min when increasing the distance between Z scans from 2 to 5μm. For higher separations along Y the etch rate remained constant at 18μm/min. This indicates that the etching process differs when the scans have a great degree of overlap. For small overlap and higher separations, the scans do not interact with one another and the etch rate obtained is similar to the one measured for

single-scan channels. However, increasing the overlap increases the etch rate. This result may be a consequence of the higher stress fields that, as shown by Agarwal [44], affects the etch rate.

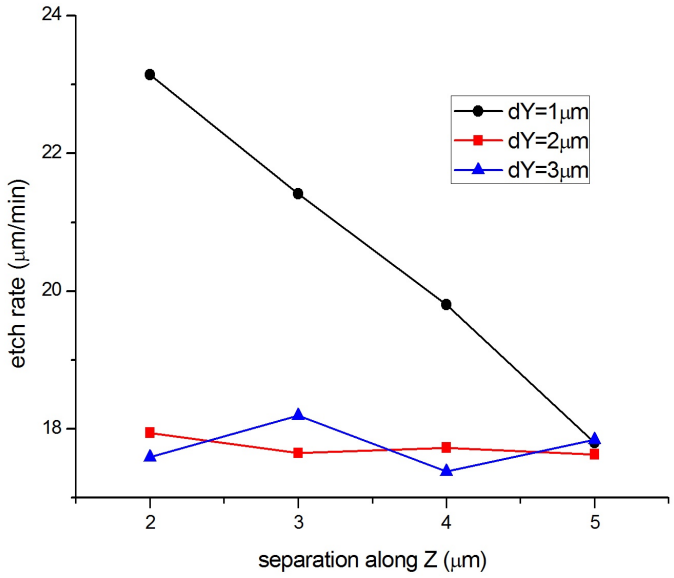

Figure 4.12: Etch rate of channels as function of the separation between scans. The channels were written 150μm below the surface with perpendicular polarization, with 60nJ pulse energy and at 500μm/s.

Lastly, in figure 4.13 it is shown a top-view image of multi-scanned channels. Unlike in single-scans, these present different colours along the channel. At its entrance it appears bright, indicating that the etching reaction is complete and that all the debris is removed. It then starts looking darker showing that etching has already begun, but the HF still did not dissolve all the glass. This feature is particularly important because if this debris is not removed it can clog the channel. For this reason we perform the etching in an ultrasonic bath, which breaks and helps removing the debris. The end of the glass is again bright, because the HF acid still has not reached this zone.

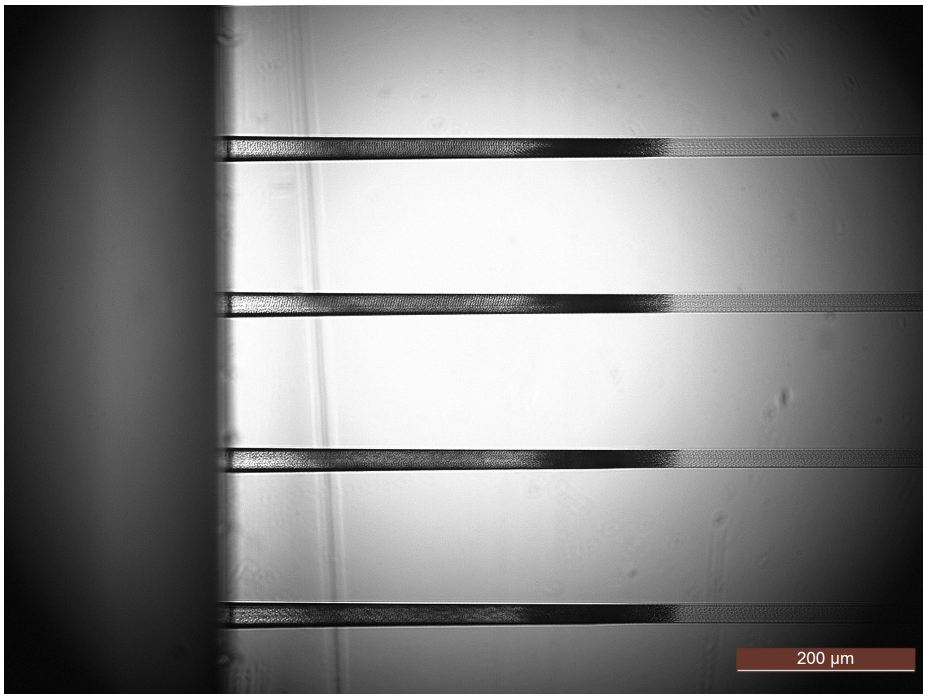

Figure 4.13: Evolution of the etching reaction of channels fabricated at a depth of 140μm at a speed of 500μm/s with 60nJ pulse energy and with perpendicular polarization. The channels were written by multi-scanning and the separation along Y is of 1μm and along Z is of 2 to 5μm (bottom to top in the image, respectively). The image was taken after 60 minutes of etching.

4.3 Surface roughness

The channel sidewalls have to be sufficiently smooth to minimize optical losses due to scattering; thus surface roughness is of huge importance for optofluidic applications [68]. This parameter depends on two contributions: first, the channels are written by scanning multiple lines with well-defined separations in the transverse direction (along Y) and in the vertical direction (along Z). Therefore the line-to-line separation affects the surface roughness as the etched lines may or may not open up to each other, allowing formation of larger channels. Second, the irradiation conditions induce stress fields that deform the channel, and in the limit may induce cracks.

Before characterization, the glass facet that contains the entrance of the channels was polished. The surface roughness was characterized by direct observation on an optical microscope and on a SEM microscope (available at CEMUP facilities). SEM observations were conducted in environmental mode, avoiding the need of deposition of a conductive layer in the fused silica sample. The roughness can also be measured in a profilometer, as long as the channel is at the glass surface and the channel dimensions are appropriate for the measurement conditions. Although not tested, AFM microscopy may also be used for characterization, enabling measurements with high resolution.

Single-scan channels

The single-scan channel cross-section resembles an ellipse with dimensions 2μm by 6μm. After etching for 1 hour, the micro-channel appears dark under backlighting and increased in cross-section area (5μm by 11μm) compared with the original modified volume size. The elliptical cross-section shape approximately follows the laser profile, although we notice that the ellipse is narrower at the bottom than at the top, as shown in figure 4.14.

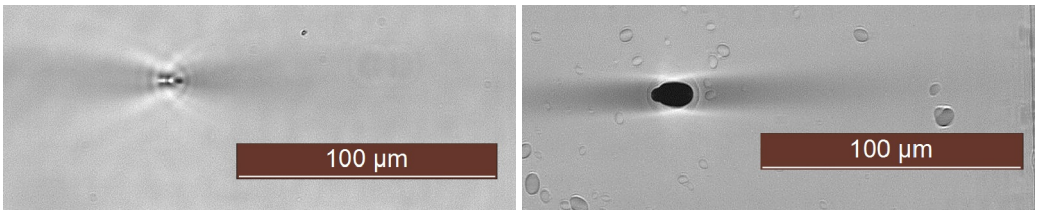

Figure 4.14: Single-scan channel written 150μm below the surface at 500μm/s with 60nJ pulse energy and with perpendicular polarization. The left picture depicts the channel after writing and the right picture shows the channel after etching for 1 hour.

By measuring the width and height of the channel cross-section, before and after etching for 1 hour, we verified that the scanning speed had no influence in these parameters. An optical assessment provided the same conclusion regarding the cross-section surface.

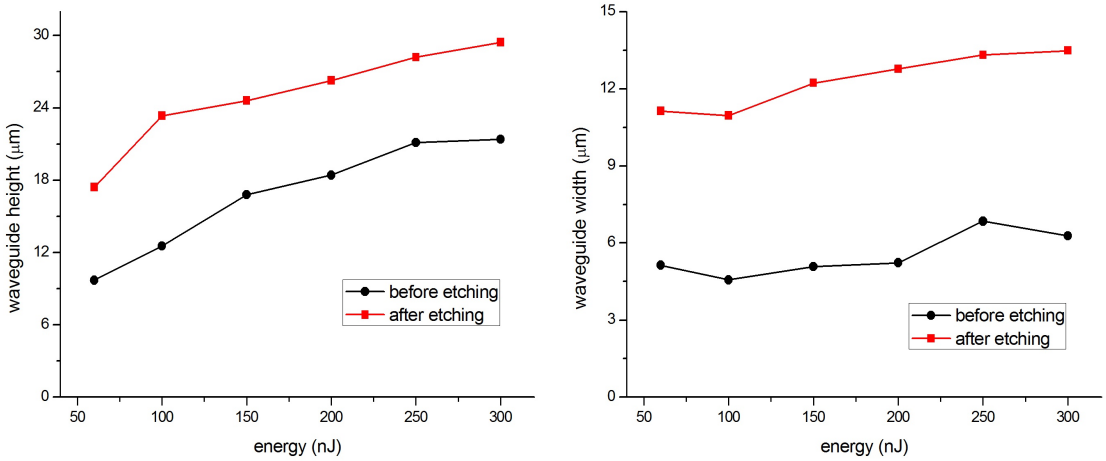

Figure 4.15: Single-scan channel dimensions: height (left) and width (right) after and before etching as a function of the pulse energy. The channels were fabricated with perpendicular polarization, 150μm below surface and at 500μm/s.

However, when changing the pulse energy from 60 to 300nJ we observe an increase of 9μm in height and an increase of 3μm in width, prior and after etching (figure 4.15). These results may be understood as follows: by increasing the pulse energy, the beam intensity increases. Thus a bigger volume is subject to an intensity higher than the threshold level for structural modification.

The relative difference in the width and height dimensions is due to the asymmetrical cross-section of the channel. As mentioned before, this occurs in the transverse configuration and can be corrected by using an objective with higher numerical aperture. The increase in

the channel size is not abrupt enough to suggest that self-focusing is occurring. In addition, the image at figure 4.16 demonstrates that increasing the pulse energy deforms the channel cross-section.

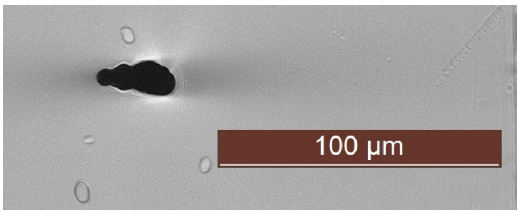

Figure 4.16: Single-scan channel after etching for 1 hour. The channel was produced with perpendicular polarization, 150μm below surface at 400μm /s and with 300nJ pulse energy.

Influence of irradiation conditions

Regarding the channels written by exposing multiple laser-affected zones, we observed that increasing the scanning speed increases the channel surface quality. As the scanning speed decreases, the laser fluence and the number of pulses incident at the same spot increases, thus the induced stress grows deforming the channel walls.

The surface roughness also depends on the pulse energy. Increasing the energy results in irregular and almost irreproducible surface morphologies [56]; in particular at very high energies (300nJ) the channels present cracks, as seen in figure 4.17. The irradiation parameters tested are also used to fabricate low-loss waveguides, which are associated to material densification, that generate stress fields of the order of GPa [62]. The stress fields induce birefringence in transparent materials, that can be measured by passing light through the material [69]. It was observed that the stress decays with increasing line-to-line separation and that the stress field depends on the nanograting orientation. This work also showed that nanograting regularity degrades as the pulse energy increase.

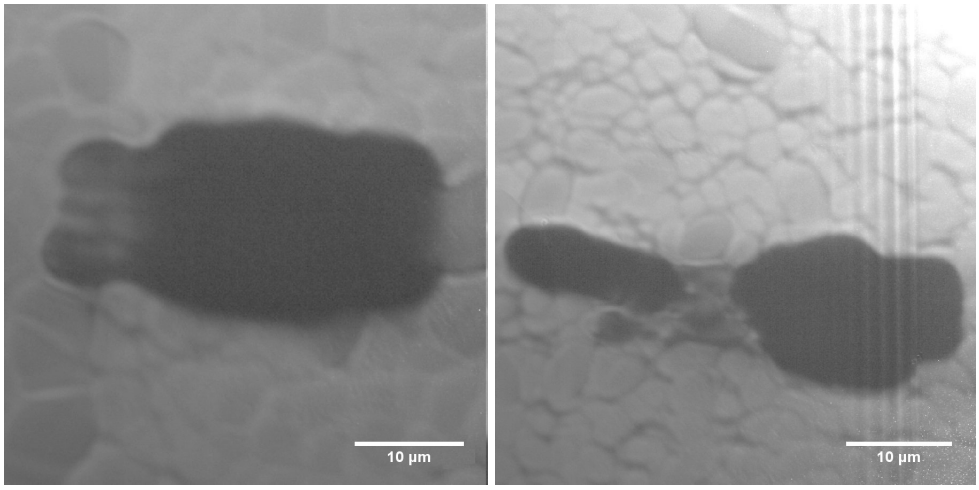

Figure 4.17: Effect of the pulse energy on channels produced 100μm below surface at 100μm/s with perpendicular polarization and line-to-line separation of 1μm along Y and 2μm along Z direction. The left picture shows a channel produced with 100nJ pulse energy, and the right picture a channel with 300nJ.

Stress accumulated in the channel may, under sufficient laser exposure, be released by relaxation processes over a typical range of a few microns as shown in figure 4.18. The resulting cracks form outside the irradiated volume, preferentially at the corners, and tend to propagate towards the region of unmodified material. The cracks affect the wall roughness and the channel fluidic properties, limiting its application. In addition, several groups reported that at high laser fluence, the channel surface became pitted and presented unetched material [56, 68].

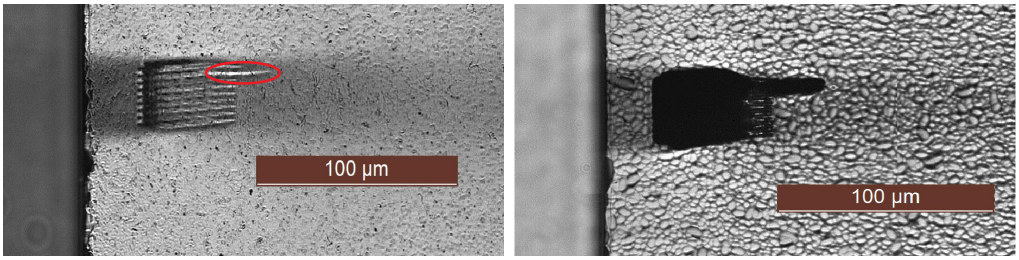

Figure 4.18: Microfluidic channel before (left) and after (right) etching for 50 minutes. The channel was written 50μm below surface at 200μm/s with 300nJ pulse energy and with parallel polarization.

The stress fields depend on the nanograting orientation, having been shown that crack formation is more likely for parallel and circular polarization: the nanogratings form perpendicularly and randomly along the scanning direction, respectively, building up a higher stress along the channel [69]. Increasing pulse duration also favours the formation of cracks [29].

The lowest stress accumulation, which favours smoother channel walls, happens near the threshold for selective etching. Therefore, to obtain crack-free microfluidic channels, they have to be fabricated at low energies near the threshold (60-80nJ) and at high scanning speeds (around 500μm/s). In addition, the laser beam polarization has to be perpendicular to the scanning direction to improve surface quality.

Influence of line-to-line separation

The line-to-line separation, if on the order of tenths of nanometers, increases the stress field in the irradiated volume and may generate cracks [69]. However, it can not be of the order of tenths of microns, as the resulting structure would present unetched material within the channel [62]. Thus, the distance between scans has to be optimized to enable production of channels with smooth walls. As seen before a single-scan channel presents an elliptical cross-section longer along Z. Hence we expect that the optimum separations between scans along the vertical direction (Z) and transversal direction (Y) will be different.

In the following discussion, all the channels were written with perpendicular polarization, 150μm below surface, at 500μm/s and with 60nJ pulse energy. The laser beam was always incident from outside of the glass.

We started by fabricating channels along the Z axis, with separations varying between 1μm and 15μm. The obtained profiles are shown in figure 4.19. Varying the scan separation, we noticed that at separations of 9μm or higher, a layer of unmodified fused silica remained in

between the etched waveguides. Decreasing the scan separation to 1-4μm the channel walls became smoother.

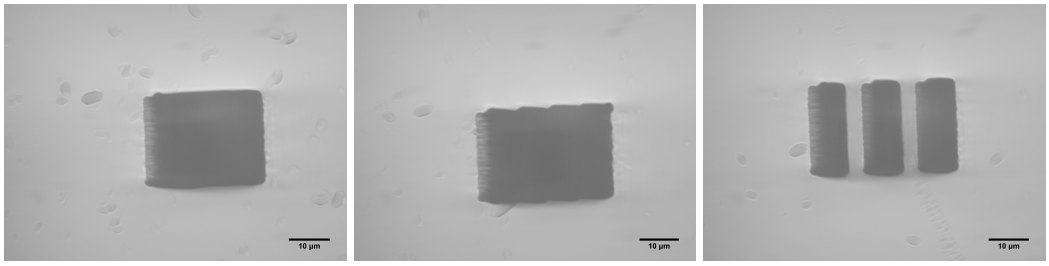

Figure 4.19: Influence of the vertical line-to-line separation on channels etched for 30 minutes and produced with perpendicular polarization, 150μm below surface at 60nJ pulse energy and at 500μm/s. The separation along Y is of 1μm and along Z is of 2μm, 7μm and 12μm (from left to right, respectively).

Regarding the channels produced along Y, the line-to-line distance varied between 0.5μm and 7μm. Figure 4.20 presents the channel profile obtained. We observed that the etched scans would not merge for separations bigger than 6μm. For separations between 3μm to 5μm, the scans merge but the top and bottom walls are strongly corrugated. The channels with smoother walls are obtained for separations in the range 1μm to 2μm.

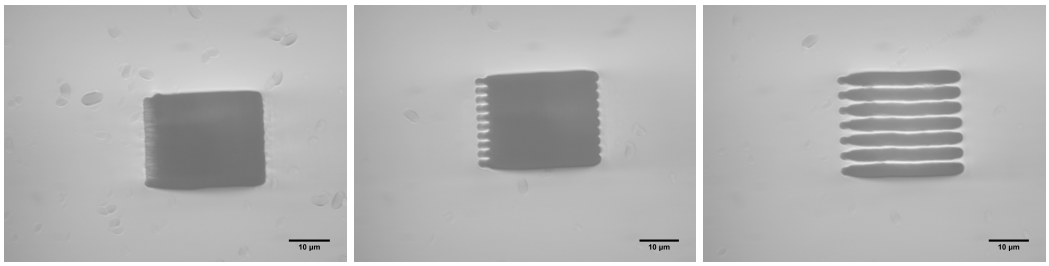

Figure 4.20: Influence of the transverse line-to-line separation on channels etched for 30 minutes and produced with perpendicular polarization, 150μm below surface at 60nJ pulse energy and at 500μm/s. The separation along Z is of 2μm and along Y is of 1μm, 3μm and 5μm (from left to right, respectively).

Many applications, such as filtering and flow cytometry may take advantage of the production of capillaries, that are produced at separations higher than 9μm along Z and higher than 6μm along Y, as shown in figure 4.21.

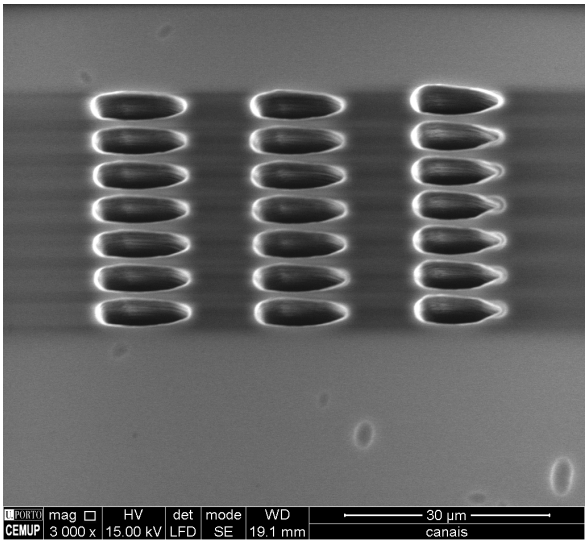

Figure 4.21: Capillaric structures etched for 30 minutes and produced with perpendicular polarization, 150μm below surface at 60nJ pulse energy and at 500μm/s. The separation along Y and Z is 6μm and 15μm, respectively.

The SEM image in figure 4.22 right, shows an etched profile consisting of corrugated structures. These structures are as numerous as the scanned lines and the spacing is identical, thus we conclude that this periodicity corresponds to the number of laser-affected zones written.

By producing channels at the fused silica surface, we were able to measure the surface roughness along Y with a profilometer (we used a stylus with 2μm radius and with 3mg applied force). In average the surface roughness varied between 100-200nm, similar to results obtained by other groups and on the same order as the nanograting separation. This roughness is too high for many optofluidic applications, since it results in scattering of light and in high coupling losses. However, the resolution along Z is better and channels produced under similar conditions have been shown to have a surface roughness of around 20nm along this direction, enabling light coupling with low losses. The 5x smoother sidewalls are attributed to the parallel alignment of nanogratings with the channels sidewalls.

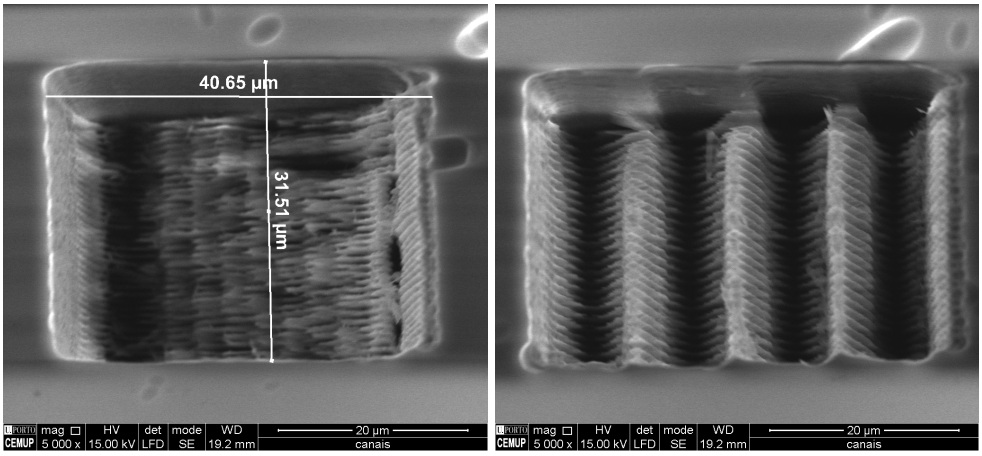

Figure 4.22: SEM images of the cross-section of channels etched for 30 minutes and produced with perpendicular polarization, 150μm below surface at 60nJ pulse energy and at 500μm/s. In the left picture the separation along Y and Z is 0.8μm and 2μm, respectively. In the right picture the separation along Y and Z is 1μm and 7μm, respectively.

In conclusion, this writing technique enables fabrication of crack-free microfluidic channels with submicron roughness and with flexible cross-section. To this end, we found the optimum conditions to be: beam polarization perpendicular to the scanning direction, scanning speed of 500μm/s, pulse energy between 60nJ and 80nJ, scan separation along Y of 1μm to 2μm and along Z of 1μm to 4μm and scanning depth between 50 and 150μm. An example of a channel fabricated with these parameters is depicted in figure 4.23.

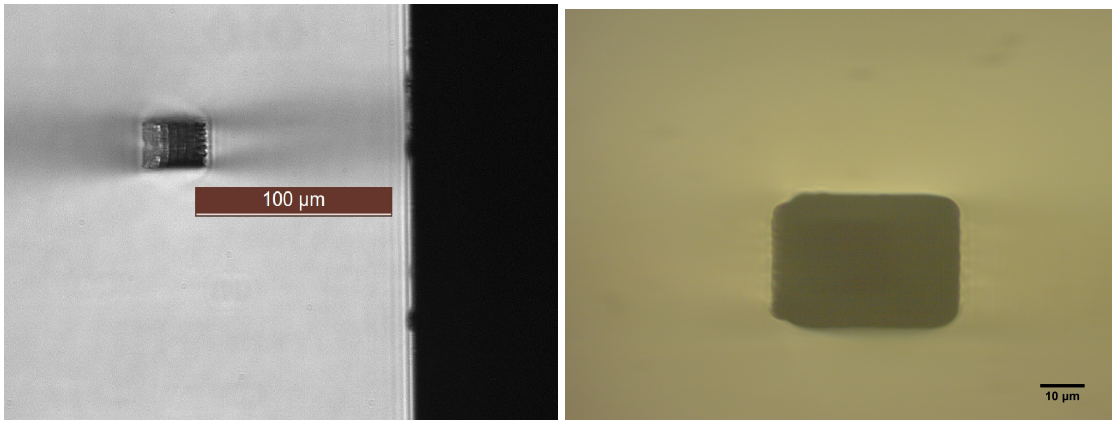

Figure 4.23: Microfluidic channel before (left) and after (right) etching for 60 minutes. The channel was written 150μm below surface at 500μm/s with 60nJ pulse energy and with perpendicular polarization. The separation along Y and Z is 1μm and 2μm, respectively.

4.4 Tapered channels

As mentioned previously, in longer channels two effects (etch rate saturation and lateral etching) contribute to the production of tapered channels. To avoid this, some writing and etching configurations have been proposed: (i) the first approach consists in pre-compensating the tapering effect by suitably wobbling the glass during irradiation, figure 4.24 [70]. This method requires precise control during writing and etching. (ii) Another solution consists in

fabricating access holes that connect the channel to the glass surface, as shown in figure 4.25 [25]. Although simpler, the produced holes may disturb fluid propagation. (iii) Fused silica may also be etched by KOH at 80°C [47]. This etchant, unlike HF acid, eliminates the saturation effect at the expense of lower etch rates. In this project we chose the second described method to produce the buried channels. Potassium hydroxide was not tested in this project.

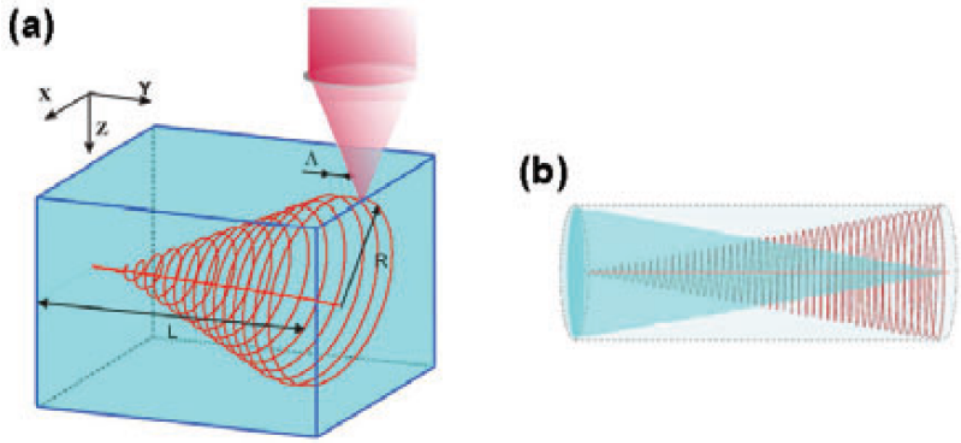

Figure 4.24: Scheme of pre-compensation writing technique for production of long channels with high aspect ratio [39]. The dashed lines correspond to the written structure and the blue cone to the etching effect when the HF acid diffuses in the channel, starting from the left.

The access holes are fabricated following the same procedure as the microfluidic channels. However, some cautions must be taken in the design of these structures.

First, because the access holes have to be at the sample surface, high pulse energies can not be used. The threshold for modification is significantly lower at surface than in-depth, so low pulse energies have to be used to minimize ablation and to avoid damaging optical components, in particular the objective lens.

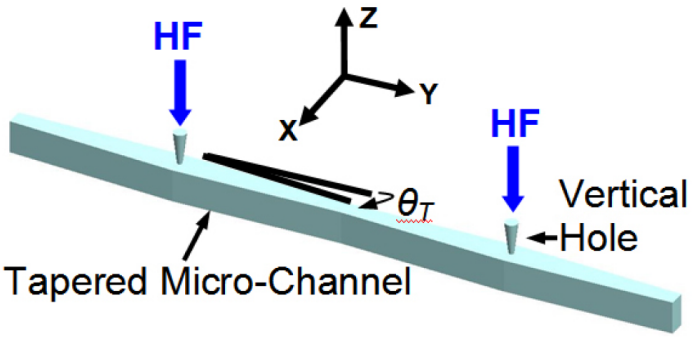

Figure 4.25: Fabrication layout of access holes.

Second, the fabrication of access holes can be seen as stacking of rectangular planes along Z that must be separated by 1μm to 3μm. In case of increasing this separation, we observed at SEM (figure 4.26) that the holes are not fully etched leaving behind thin layers of unexposed glass. In addition, if some of the holes do not allow acid diffusion, some zones of the channel are not etched resulting in deposition of glass fibers at the channel bottom. These fibers can

have lengths of hundredths of microns, can not be removed easily and can clog the channel.

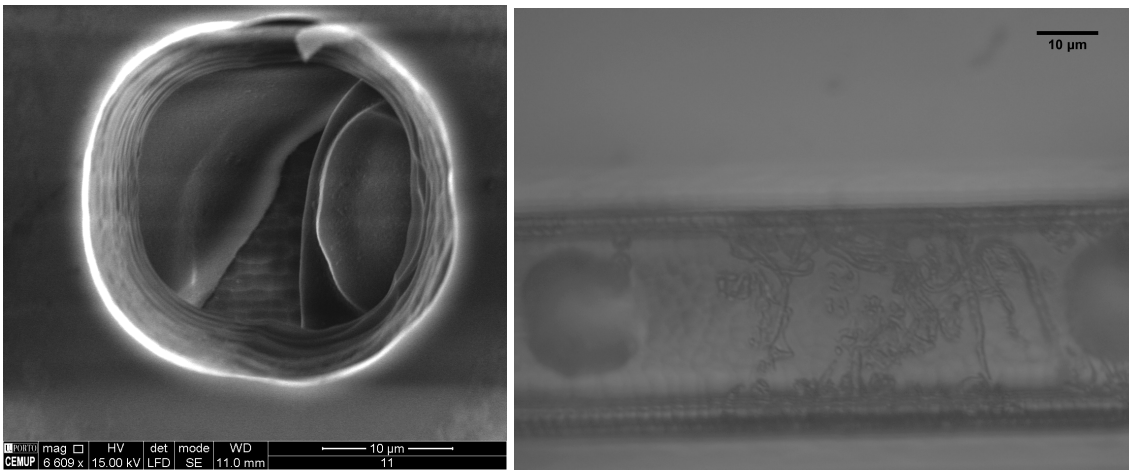

Figure 4.26: Unetched access holes (left) and clogged channel (right). The left picture is a SEM image of an unetched access hole etched for 2 hours and fabricated with perpendicular beam polarization at 100μm/s with 125nJ and with separations along Y and Z equal to 2 and 9μm. The right picture depicts a microfluidic channel with glass fibers of unetched material deposited at the bottom.

Regarding the access hole, initially it has a rectangular cross-section, but after etching it has a circular section due to isotropic etching of the unexposed silica. We also observed that the hole size increased, which can disturb the fluid flow and may demand an additional sealing process. For diameters lower than 5μm, the holes act as sealed due to strong surface tension of the liquid reaching the hole opening.

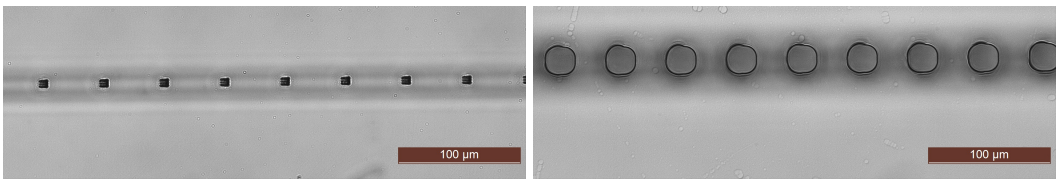

Figure 4.27: Top picture of the access holes after writing (left) and after etching for 90minutes (right). Initially the holes have a rectangular section, but after etching it becomes circular.

To obtain channels with constant aspect ratio through its entire length, we also optimized the separation between access holes. The channels were fabricated with perpendicular polarization at 500μm/s with 60nJ pulse energy, 150μm below the glass surface and with separation of 1μm and 2μm along Y and Z, respectively. The access holes were written at the centre of the channel axis, with perpendicular polarization at 100μm/s with 100nJ pulse energy and with separations along Y and Z equal to 1μm and 2.5μm, respectively. After etching, the channels were first rinsed in deionized water, then cleaned with isopropanol and again rinsed. All these processes were performed in an ultrasonic bath to facilitate removal of any debris left. Lastly, the sample was heated in a hot plate at 100°C.

We tested separations between holes of 50, 100 and 200μm (figure 4.28). We observe that as the acid reaches the channel it propagates faster along the channel axis, due to the favourable alignment of the nanogratings. In addition, the channel is etched faster for low

separations as is expected, since there is an increase in entrances for acid diffusion. However, for a separation of 200μm, the end result is very similar to the one obtained for a separation of 50μm. Thus separations of 200μm can be used to produce centimeter long microfluidic channels with uniform aspect ratio.

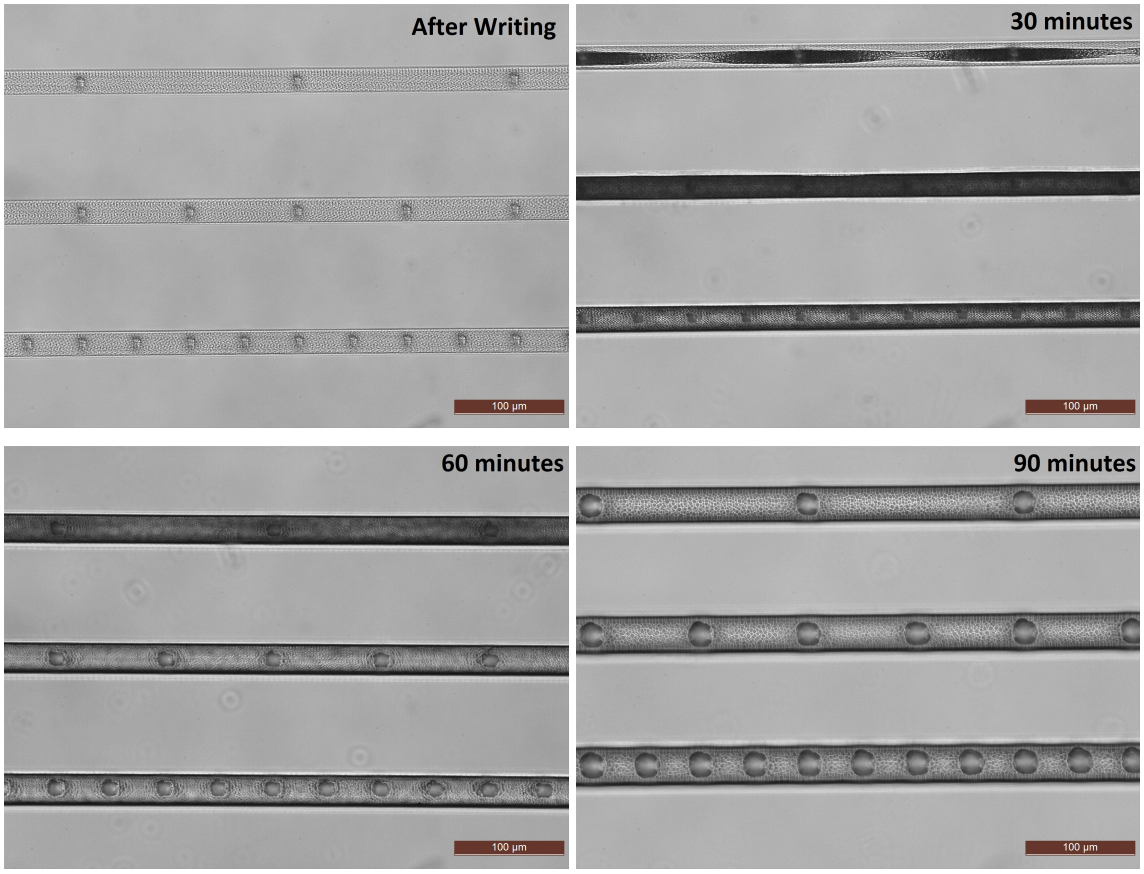

Figure 4.28: Comparison of the etching reaction in channels fabricated with access holes separated by 50, 100 and 200μm. The channels were fabricated 150μm below surface with perpendicular polarization, at 500μm/s, with 60nJ pulse energy and with scan separations of 1μm and 2μm along Y and Z respectively. The access holes were fabricated with perpendicular polarization, at 100μm/s, with 125nJ pulse energy and with scan separations of 2μm and 6μm along Y and Z direction, respectively. The top left picture was taken before etching, the top right after 30 minutes of etching, the bottom left after 60 minutes and the bottom right after 90 minutes.

Lastly, we were able to observe through the access holes the channel bottom at SEM microscopy. The channel, depicted in figure 4.29, has the same profile as the one obtained by other groups [62, 68].

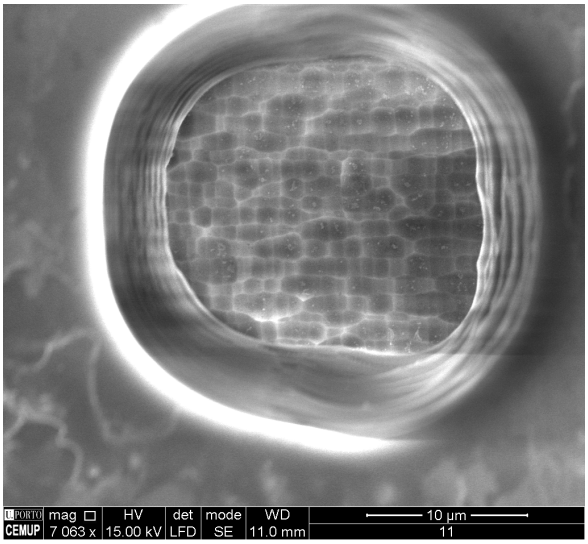

Figure 4.29: SEM image of the bottom of a microfluidic channel fabricated 150μm below the glass surface, with perpendicular polarization at 500μm/s and with 60nJ pulse energy.

4.5 Integration of optical layers with microfluidic channels

The fabricated microfluidic channels present roughness of around 100 to 200nm in the Y direction and of around 20nm in the Z direction, as seen already. The wall roughness of the microfluidic channels creates some scattering resulting in additional optical loss, though a wall roughness below 100nm avoids excessive loss [43]. Thus, the channels produced may be integrated with photonic components for cell manipulation and biosensing applications. Several optical detection schemes have been proposed from which we highlight: evanescent coupling between Bragg grating waveguides (BGW) and microfluidic channels [71], and direct excitation of waveguides crossing the channel [11, 72]. Both schemes are depicted in figure 4.30 .

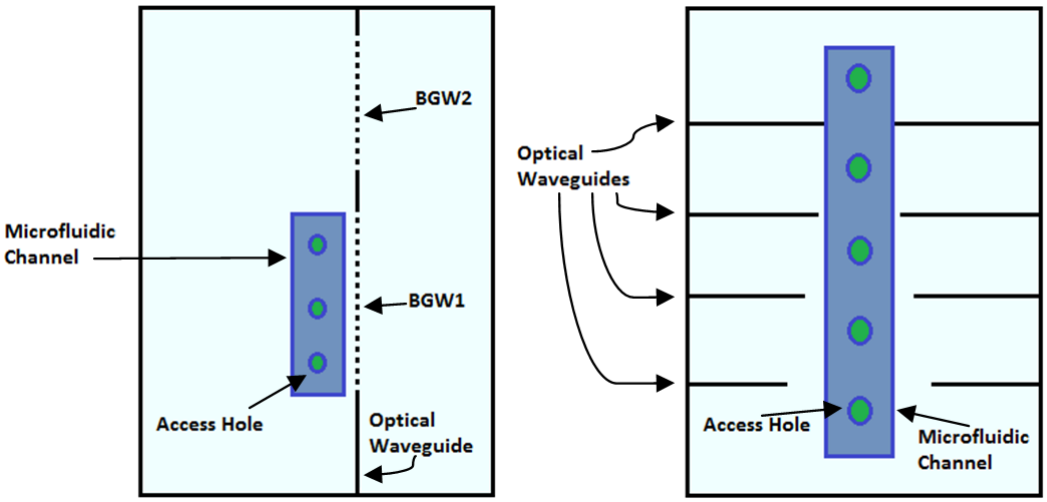

Figure 4.30: Optical detection schemes. The left picture is an example of an evanescent coupling detection scheme and the right picture an example of direct excitation scheme.

Before presenting the obtained results, we present the key concepts of waveguide and

grating theory necessary to understand this work. Further details can be found elsewhere [73, 74].

A waveguide may be considered as a medium with a core with refractive index higher than its surroundings. This structure confines light propagation to its core due to total internal reflection at the boundaries. The boundary conditions depend on the polarization of the incident laser field on the waveguiding structure.

Depending on the index contrast and on the core dimensions, the waveguide structure can support single or multimode propagation. For this work, the focus is on fabricating single mode waveguides, thus avoiding interaction between different modes.

While for a waveguide the core refractive index is constant along its length, in a Bragg grating waveguide the core refractive index is a periodic function. The modulation affects the mode propagation, leading to light reflection in a narrow range of wavelengths. The mode propagation is described by the coupled mode theory.

The Bragg reflected wavelength is given by the Bragg condition $\lambda_B = 2n_{eff}\Lambda$, where n_{eff} is the effective refractive index and Λ the modulation period. This states that the grating wavenumber matches the difference between the reflected and incident wavevectors, thus it is a relation of conservation of momentum. Light at a wavelength different than the Bragg wavelength continues its propagation unperturbed.

In the Bragg condition, the reflected wavelength depends on the effective refractive index, which in turns depends on the cladding material as well as temperature and applied strain. This feature is particularly useful to produce sensors.

Optimum conditions to produce optical waveguides and Bragg grating waveguides were determined by Vítor Amorim and can be found in chapter 3.

Scheme I - Evanescent Coupling

The proposed optical detection scheme works as follows: in a Bragg grating waveguide (and in a single waveguide), light is confined to the medium with higher refractive index. However, there is an evanescent tail that propagates in the waveguide surroundings. Thus by placing the Bragg grating waveguide (BGW1) close to the channel we are able to sense the fluid that is circulating in the channel. As mentioned before, the reflected Bragg wavelength depends, among other factors, in the medium effective refractive index. Thus, changing the fluid present in the channel or its temperature will change the reflected wavelength. This change can be monitored in an OSA, where a correlation function between Bragg wavelength and temperature or refractive index can be produced. Given that the effective index depends on external factors, such as temperature, we also produce a second grating (BGW2) that is used as a reference: because the grating is surrounded by pristine, any change in the refractive index is due only to external conditions.

Some issues regarding the channel and grating properties that affect the device performance are now discussed. First, the channel has to be long, at least 1cm in length, in order to obtain a strong grating with high reflectivity. Second, positioning of the grating relative to the channel is critical to obtain good evanescent coupling (the two elements must be distanced less than half of the waveguide mode field diameter), because the propagating mode has a Gaussian profile

and the intensity decays abruptly at the wings.

Regarding the first point, long channels with high aspect ratio are attained as shown previously. The second point is more challenging given that it requires a fine control of the etching process. Given that unmodified silica is also etched by HF, the acid may carve into the grating, destroying the device as seen in figure 4.31. It has been suggested that one could avoid this issue by manufacturing the gratings after etching [43]. This approach would however disrupt the manufacturing flow and requires highly accurate repositioning of the sample.

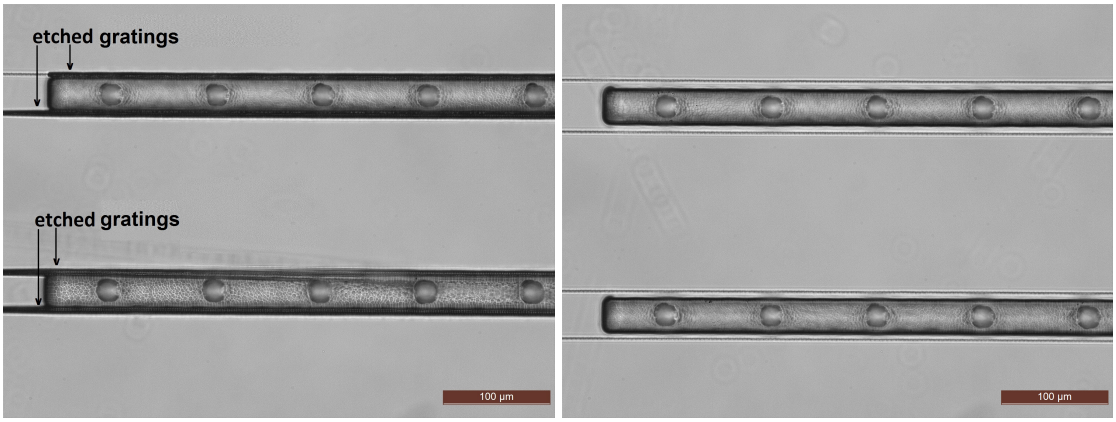

Figure 4.31: Top images of integrated Bragg grating waveguides with microfluidic channels. In the left picture, the HF acid also etched the grating. In the right picture, there is a pristine layer between the grating and the channel.

Our solution was to design channels with BGW placed at increasing distances from the channel. The microfluidic channels were 1.1 cm long, designed 100μm below the glass surface with perpendicular polarization at 500μm/s with 60nJ pulse energy and with scan separation along Y and Z equal to 1μm and 2μm, respectively. The access holes were fabricated with perpendicular polarization, at 100μm/s with 250nJ pulse energy and with scan separation equal to 1μm and 2.5μm along Y and Z, respectively. The access holes were separated by 200μm. The Bragg grating waveguides were produced with parallel polarization, 125μm below surface at 400μm/s and with 250nJ pulse energy. Two gratings were produced, one to sense the channel and designed to operate at 1550nm and another to operate at 1558nm and to serve as a reference. The gratings were fabricated with 50% duty cycle, to maximize grating strength. After writing, the two glass facets containing the gratings were polished. The etching reaction lasted 90 minutes. The devices were characterized without polarization control.

After etching we obtained 4 gratings separated 3, 4, 5 and 7μm distanced from the channel sidewall. Table 4.1 shows the Bragg wavelength for each of the gratings when the channels were empty (filled with air).

separation BGW-channel	**3μm**	**4μm**	**5μm**	**7μm**
reference ($\pm$0.05nm)	1550,48	1550,47	1550,47	1550,45
air ($\pm$0.05nm)	1550,18	1550,24	1550,26	1550,39
wavelength shift ($\pm$0.05nm)	0,30	0,23	0,21	0,06

Table 4.1: Measured Bragg wavelength for increasing separation between BGW and microfluidic channel.

We observe that the wavelength shift is higher for the grating separated 3μm from the channel. In addition increasing the separation decreases the wavelength shift validating our assumption that the gratings and the channels have to be placed as close as possible to maximize sensitivity. For a separation of 7μm the wavelength shift is practically indistinguishable from the reference wavelength, again suggesting that a fine control of the etching procedure is needed.

We then filled the channels with water and measured the Bragg wavelength only for the grating distanced 3μm from the channel. Water has a refractive index of 1.33, air of 1 and fused silica of 1.5; these kind of devices have higher sensitivity for refractive indexes closer to 1.5, explaining the small shift (0.03nm) detected when filling the channel with water. The results obtained are shown in figure 4.32.

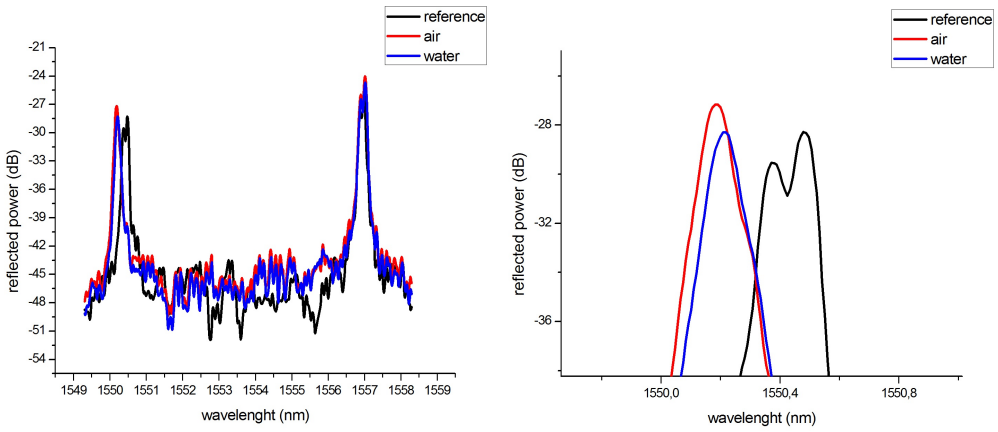

Figure 4.32: OSA measurements of a BGW placed 3μm from the microfluidic channel, when the channel is filled with air and with water. The left picture is a zoom image of the right one.

Scheme II - Direct Excitation

In this scheme, the produced optical waveguides cross the microfluidic channel. The two waveguide ends are butt-coupled to single-mode fibers. One of the fibers is connected to a laser source, while the other is connected to a powermeter. This way we can measure the power loss across the system. Applications of this scheme include cell counting experiments by production of an interferometer, particle detection by fluorescent excitation [11, 72], and optical trapping [18].

In this case, the power loss is due to three contributions: intrinsic losses of the optical waveguide and excess losses due to propagation across channel (related to channel width) and pristine layer (related to separation between waveguide and channel). Intrinsic losses were not considered, because all the waveguides were fabricated at the same conditions.

Regarding the separation waveguide-channel, we started by fabricating interrupted waveguides as shown in figure 4.33, where the waveguides are separated by a pristine layer. All the waveguides were written at a depth of 100μm, at scanning speed of 400μm/s, with parallel polarization and with 250nJ pulse energy. The separation between waveguides varied between 10μm and 140μm. An uninterrupted waveguide served as reference.

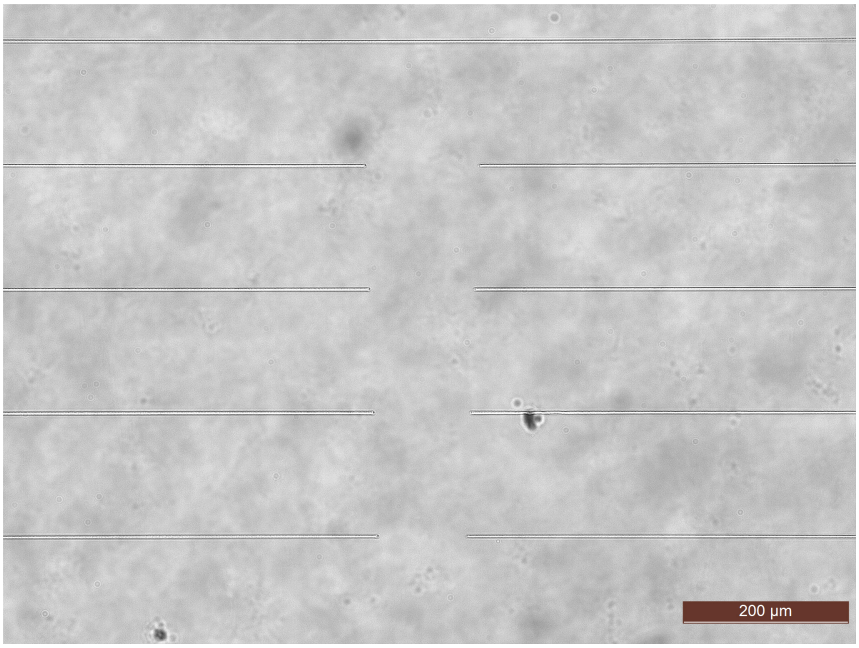

Figure 4.33: Top view of written waveguides separated by pristine glass. The waveguides were written at a depth of 100μm, at scanning speed of 400μm/s, with parallel polarization and with 250nJ pulse energy. The separation between waveguides varies between 110μm and 140μm, from bottom to top and in steps of 10μm.On top, the waveguide was written without interruptions, to serve as reference.

The obtained results are depicted in figure 4.34 left; these results only account for the power loss due to the gap between waveguides. As expected, increasing the separation between waveguides increases optical losses. Because the waveguide refractive index is higher than the pristine glass, when the light goes through the pristine it is no longer confined resulting in optical divergence. This way the light collected by the second waveguide and the power measured tend to decrease with higher separations. The losses increase linearly at a rate of 0.0129dB/μm.

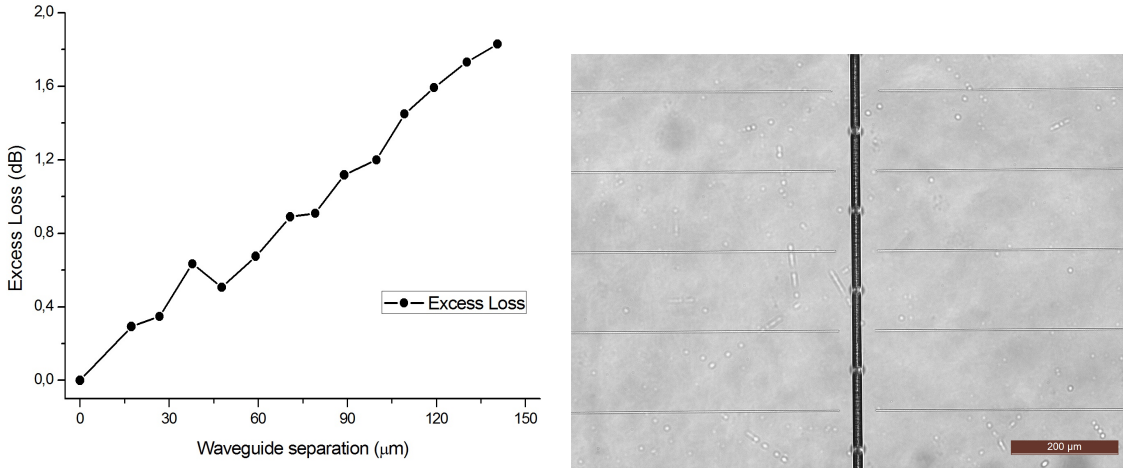

Figure 4.34: Excess loss for interrupted waveguides (left) and layout of the device (right).

We then proceeded to fabricate waveguides crossing microfluidic channels while changing

the channel width and the separation between the channel walls and the waveguide. A layout of this device is presented in figure 4.34 right. The waveguides were written at a depth of 100μm, at scanning speed of 400μm/s, with parallel polarization and with 250nJ pulse energy. The microfluidic channels were 1.5cm long, designed 100μm below the glass surface with perpendicular polarization at 500μm/s with 60nJ pulse energy and with scan separation along Y and Z equal to 1μm and 2μm, respectively. The access holes were fabricated with perpendicular polarization, at 100μm/s with 250nJ pulse energy and with scan separation equal to 1μm and 2.5μm along Y and Z, respectively. The access holes were separated by 150μm each. The etching reaction lasted 120 minutes. After etching, the two glass facets containing the waveguides were polished.

The results obtained are depicted in figure 4.35 left for different channel widths (with air inside the channel) and in figure 4.35 right for different fluids inside the channel (with channel width equal to 30μm).

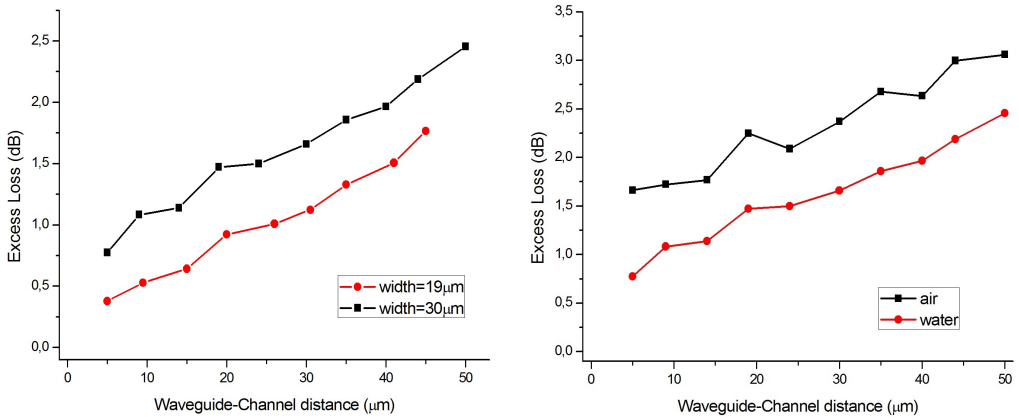

Figure 4.35: Excess loss as a function of the waveguide-channel distance for different channel widths (left) and for different fluids inside the channel (right).

We again observe that the excess losses increase linearly with the separation waveguide-channel. For the channel with width equal to 19μm the losses increase at a rate of 0.0329dm/μm, while for the channel with width equal to 30μm the losses increase at a rate of 0.0339dB/μm. To minimize these additional losses, the waveguides should end at the channel walls. However this is difficult to achieve in practice as the HF acid may carve to the waveguide, similarly to what as observed for the previous scheme.

We also conclude that the excess losses are always higher in the wider channel. Again, because air (refractive index of 1) is circulating inside the channel, the optical divergence is higher for the wider channel which leads to higher losses. Comparing the obtained losses to the previous case (interrupted waveguides, without channel) the losses are now higher due to the same fact: pristine has an higher refractive index than air.

For wider channels, over the tested range, light divergence results in excessive loss. A possible solution to avoid this effect is the fabrication of collimators [43], which correspond to a tapered waveguide. The taper presents an initially wide cross-section, to capture more light, that gradually decreases to the dimension of a standard waveguide.

With the channel with 30μm width, we tested this device for two different fluids: air and water

(refractive index of 1.33). The same conclusions regarding the excess loss as a function of the fluid refractive index apply in this case: the losses are higher for air than for water.

The results shown are promising, in that we were able to successfully integrate optical layers with microfluidic channels in the same platform and in the same writing step. In addition, with the two detection schemes we were able to differentiate two different fluids present in the channels. Still, a lot is to be done in this area; in particular precise control of the waveguide/grating-channel distance is needed.

4.6 Optical Fibers

The FLICE technique may also be applied to optical fibers to produce lab-in-a-fiber systems [75], promising to solve an important issue regarding coupling between the light propagating in the core with the cladding where reagents can be introduced [76].

Although these devices are not the main focus of this work, some tests regarding the production of cavities at the fiber tip were done. These devices would work as follows: light propagating in the fiber would reflect at the cavity walls and interfere. The resulting interference pattern would allow two kinds of measurements: (i) refractive index or temperature measurements if the fiber cavity was immersed in a liquid solution [77], and (ii) strain measurements if the tip was deformed [78]. The cavity walls, again, have to be smooth to avoid light scattering.

We observed that the etching mechanism is significantly different for fibers and for slabs. First, the fiber has a cylindrical geometry and is formed by two different materials for core and cladding. Therefore, the etch rate is intrinsically different [78]. In addition the cladding diameter is equal to 125μm for typical SMF fibers, enhancing border effects and decreasing the etch rate, relatively to what is observed in slabs.

Second, we observed that the threshold for structural change is different in fibers. For pulse energies higher than 100nJ, the cavity would always crack at its bottom, which can potentially break the fiber.

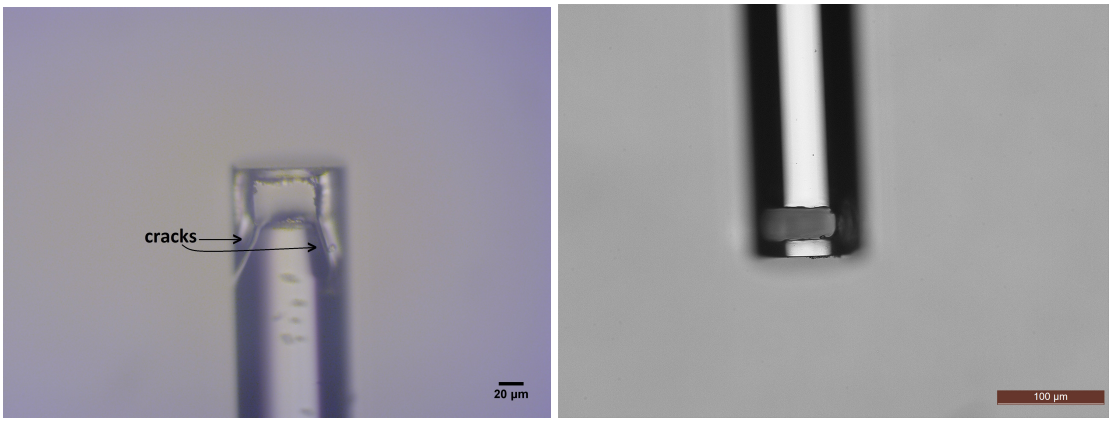

Figure 4.36: Micromachined fiber tip. In the left picture, a cavity was written in an optical fiber with perpendicular polarization with 250nJ pulse energy at 100μm/s and etched for 30 minutes. In the right picture, a cavity was written in an optical fiber with perpendicular polarization with 100nJ pulse energy at 500μm/s and etched for 90 minutes. The fiber, depicted in the left, presents two cracks and high surface roughness, while the fiber at the right does not present cracks and has smoother walls.

Also, for many applications a cavity height of around 20-30μm is enough to achieve good performance. Thus, the writing technique involves irradiation of multiple scans only along Y. In addition, and unlike in slabs, the fiber can be subject to annealing by fusion splicing, which lowers surface roughness and removes any existent debris [79].

To conclude, to fabricate fiber-based devices an optimization of the irradiation conditions (pulse energy, scanning speed, scanning separation) is still needed to obtain structures with small roughness. However, the production of cavities in fibers using this methodology has been demonstrated in this project.

Chapter 5

Conclusion and Future Work

In this project we employed the FLICE technique to study and fabricate crack-free microfluidic channels with smooth walls and uniform aspect ratio. To fabricate large channels with flexible cross-section we adopted a multiscanning writing technique.

By varying the irradiation conditions we were able to characterize the etch rate, that defines the channel aspect ratio. We concluded that the beam polarization has a significant role in the etching process: with perpendicular polarization the nanogratings are aligned with the channel axis allowing fast acid diffusion, while for parallel polarization the nanogratings block the etchant diffusion. Regarding writing with perpendicular polarization we also observed that speed and energy did not have a significant influence in the etch rate, that remained constant within the tested range. Increasing the scanning depth, we observed an increase in the etch rate due to spherical aberrations. A maximum etching selectivity of 140:1 was obtained.

Regarding the channel surface, with the adopted writing technique we verified two different features. First, the line-to-line separation, alongside pulse energy and scanning speed, originate stress fields around the microfluidic channel that, at sufficient exposure conditions, can deform the channel. In particular, for a pulse energy of 300nJ or for line-to-line separations of hundredths of nanometers, the channel presented cracks. Second, for high separations between exposed lines, a thin layer of unmodified material remains in between the laser affected zones. Therefore to obtain microfluidic channels with good surface quality we found the optimum conditions to be: beam polarization perpendicular to scanning direction, pulse energy close to the threshold level (60-80nJ), scanning speed of 500μm/s, scanning depth between 50μm and 150μm, and line-to-line separations of 1μm to 2μm in the transverse direction and 1μm to 4μm in the vertical direction.

Upon fabricating microfluidic channels we also observed a saturation effect that limits the obtained aspect ratio. To surpass this problem, we adopted the technique proposed by Ho et al [25], in which holes connecting the buried channel to the sample surface are made, allowing etchant diffusion. In our system, we conclude that a separation of 100μm to 200μm between holes is sufficient to fabricate 1.5cm channels with uniform aspect ratio.

Due to the elliptical cross-section of a single modification track, we obtained different surface roughness for the transverse and vertical direction. Under optimum conditions, we estimate the roughness to be of tenths of nanometers in the vertical direction and of hundredths of nanometers in the transverse direction. The former result highlights one of the advantages

of the FLICE technique: it can be used to integrate optical layers with microfluidic channels in the same platform. Following from the study conducted by Vítor Amorim [64] regarding the fabrication of optical waveguides and Bragg grating waveguides, we were able to demonstrate the integration of optical and fluidic components.

In a first test we produced Bragg grating waveguides separated less than 5μm from a microfluidic channel and, through evanescent coupling, were able to measure different Bragg wavelengths for different fluids present in the channel. The device production still lacks control of the distance between channel and optical layer: as shown only separations below 5μm allow measurements with high sensitivity. To achieve the required dimensional etching control, we propose attaching an optical fiber to one end of the chip; therefore the etching can be controlled in real time by monitoring the reflected optical signal of a grating.

For the second detection scheme we fabricated optical waveguides crossing the microfluidic channel and verified that by increasing channel width or waveguide-channel distance the power lost across the entire system increased. Although we have obtained promising results, the device production still lacks control of the etching process and further experiments need to be conducted.

The FLICE technique can also be applied to optical fibers, which offer a straightforward means to interconnect numerous types of sensing elements. Some exploratory work towards the production of cavities at the fiber tip was performed, but a full optimization of the fabrication parameters has yet to be conducted.

Recapitulating, the main achievement of this work was the optimization of the fabrication process of microfluidic channels, where crack free channels with smooth sidewalls of submicron roughness and with constant aspect ratio through the entire channel length were obtained. These structures are essential for fabrication of high-quality optofluidic devices and following this initial work it is expected to: (i) develop new optical detection schemes, (ii) combine these components with polymeric microstructures constructed by two-photon polymerization and (iii) study the FLICE fabrication process in optical fibers.

Bibliography

[1] Petra S. Dittrich and Andreas Manz. Lab-on-a-chip: microfluidics in drug discovery. *Nature reviews. Drug discovery*, 5(3):210–218, 2006.

[2] Terence G. Henares, Fumio Mizutani, and Hideaki Hisamoto. Current development in microfluidic immunosensing chip. *Analytica Chimica Acta*, 611(1):17–30, 2008.

[3] George M. Whitesides. The origins and the future of microfluidics. *Nature*, 442, 2006.

[4] Katrien De Vos, Irene Bartolozzi, Etienne Schacht, Peter Bienstman, and Roel Baets. Silicon-on-Insulator microring resonator for sensitive and label-free biosensing. *Optics Express*, 15(12):7610–7615, 2007.

[5] Hongkai Wu, Aaron Wheeler, and Richard N. Zare. Chemical cytometry on a picoliterscale integrated microfluidic chip. *Proceedings of the National Academy of Sciences of the United States of America*, 101(35), 2004.

[6] Bib-Bin Xu, Yong-Lai Zhang, Hong Xia, Wen-Fei Dong, Hong Ding, and Hong-Bo Sun. Fabrication and multifunction integration of microfluidic chips by femtosecond laser direct writing. *Lab on a chip*, 13:1677–1690, 2013.

[7] Keyin Liu, Qing Yang, Shengguan He, Feng Chen, Yulong Zhao, Xiaole Fan, Lei Li, Chao Shan, and Hao Bian. A high-efficiency three-dimensional helical micromixer in fused silica. *Microsystem Technologies*, 19(7):1033–1040, 2013.

[8] David J. Hwang, Moosung Kim, Kuniaki Hiromatsu, Hojeong Jeon, and Costas P. Grigoropoulos. Three-dimensional opto-fluidic devices fabricated by ultrashort laser pulses for high throughput single cell detection and processing. *Applied Physics A: Materials Science and Processing*, 96(2):385–390, 2009.

[9] K. Sugioka, Y. Cheng, and K. Midorikawa. Three-dimensional micromachining of glass using femtosecond laser for lab-on-a-chip device manufacture. *Applied Physics A: Materials Science and Processing*, 81(1):1–10, 2005.

[10] Roberto Osellame, Giulio Cerullo, and Roberta Ramponi. Femtosecond Laser Micromachining. *Springer*, 2012.

[11] Rebeca Martinez Vazquez, Roberto Osellame, Daniela Nolli, Chaitanya Dongre, Hans van den Vlekkert, Roberta Ramponi, Markus Pollnau, and Giulio Cerullo. Integration of femtosecond laser written optical waveguides in a lab-on-chip. *Lab on a chip*, 9(1):91– 96, 2009.

[12] Ya Cheng, Koji Sugioka, Masashi Masuda, Koichi Toyoda, and Masako Kawachi. 3D microstructuring inside Foturan glass by femtosecond laser. *Proceedings of SPIE - The International Society for Optical Engineering*, 50(50):101–106, 2003.

[13] Dezhi Tan, Kaniyarakkal N. Sharafudeen, Yuanzheng Yue, and Jianrong Qiu. Femtosecond laser induced phenomena in transparent solid materials: Fundamentals and applications. *Progress in Materials Science*, 76(September 2015):154–228, 2016.

[14] Peter Zeil, Christian Voigtländer, Jens Thomas, Daniel Richter, and Stefan Nolte. Femtosecond laser-induced apodized Bragg grating waveguides. *Optics Letters*, 38(13):2354–6, 2013.

[15] K. M. Davis, K. Miura, N. Sugimoto, and K. Hirao. Writing waveguides in glass with a femtosecond laser. *Optics Letters*, 21(21):1729, 1996.

[16] Andrius Marcinkevicius, Saulius Juodkazis, Mitsuru Watanabe, Masafumi Miwa, Shigeki Matsuo, Hiroaki Misawa, and Junji Nishii. Femtosecond laser-assisted threedimensional microfabrication in silica. *Optics Letters*, 26(5):277–279, 2001.

[17] N. Bellini, K. C. Vishnubhatla, F. Bragheri, L. Ferrara, P. Minzioni, R. Ramponi, I. Cristiani, and R. Osellame. Femtosecond laser fabricated monolithic chip for optical trapping and stretching of single cells. *Optics Express*, 18(5):4679–4688, 2010.

[18] Robert W. Applegate, Jeff Squier, Tor Vestad, John Oakey, David W. M. Marr, Philippe Bado, Mark A. Dugan, and Ali A. Said. Microfluidic sorting system based on optical waveguide integration and diode laser bar trapping. *Lab on a chip*, 6(3):422–426, 2006.

[19] Yeshaiahu Fainman, Luke P. Lee, Demetri Psaltis, and Changhuei Yang. Optofluidics Fundamentals, Devices, and Applications. *McGraw-Hill*, 2010.

[20] H. A. Stone, A. D. Stroock, and A. Ajdari. Engineering Flows in Small Devices: Microfluidics Toward a Lab-on-a-Chip. *Annual Review of Fluid Mechanics*, 36(1):381–411, 2004.

[21] Koji Sugioka and Ya Cheng. Femtosecond Laser 3D Micromachining for Microfluidic and Optofluidic Applications. *Springer*.

[22] Holger Becker and Laurie E. Locascio. Polymer microfluidic devices. *Talanta*, 56(2):267–287, 2002.

[23] D. J. Lipomi, R. V. Martinez, L. Cademartiri, and G. M. Whitesides. Soft Lithographic Approaches to Nanofabrication, volume 7. *Elsevier B.V.*, 2012.

[24] Rafael R. Gattass and Eric Mazur. Femtosecond laser micromachining in transparent materials. *Nature Photonics*, 2(4):219–225, 2008.

[25] S. P. Ho. Femtosecond Laser Microfabrication of Optofluidic Lab-on-a-Chip with Selective Chemical Etching. *PhD thesis*, 2013.

[26] Fei He, Yang Liao, Jintian Lin, Jiangxin Song, Lingling Qiao, Ya Cheng, Fei He, and Koji Sugioka. Femtosecond laser fabrication of monolithically integrated microfluidic sensors in glass. *Sensors (Switzerland)*, 14(10):19402–19440, 2014.

[27] Yuki Kondo, Jianrong Qiu, Tsuneo Mitsuyu, Kazuyuki Hirao, and Toshinobu Yoko. Three-dimensional microdrilling of glass by multiphoton process and chemical etching. *Japanese Journal of Applied Physics, Part 2: Letters*, 38(10 A):1146–1148, 1999.

[28] Luís André Fernandes. Birefringence and Bragg grating control in femtosecond laser written optical circuits. *PhD Thesis*, 2012.

[29] C. Hnatovsky, R. S. Taylor, E. Simova, P. P. Rajeev, D. M. Rayner, V. R. Bhardwaj, and P. B. Corkum. Fabrication of microchannels in glass using focused femtosecond laser radiation and selective chemical etching. *Applied Physics A - Materials Science & Processing*, 84(1-2):47–61, 2006.

[30] Minwei Yang. Optical Fiber Devices Fabricated by Femtosecond Laser Micromachining for Sensing Applications. *PhD thesis*, 2011.

[31] William Shieh and Ivan Djordjevic. *OFDM for Optical Communications*. 27(3), 2009.

[32] Jesper B. Jensen, Lars H. Pedersen, Poul E. Hoiby, Lars B. Nielsen, T. P. Hansen, J. R. Folkenberg, J. Riishede, Danny Noordegraaf, Kristian Nielsen, A. Carlsen, and A. Bjarklev. Photonic crystal fiber based evanescent-wave sensor for detection of biomolecules in aqueous solutions. *Optics Letters*, 29(17):1974–1976, 2004.

[33] Marc J. Madou. Fundamentals of microfabrication and nanotechnology, volume 2. *CRC Press*, 3 edition, 2011.

[34] J .Cooper McDonald and George M. Whitesides. Poly(dimethylsiloxane) as a Material for Fabricating Microfluidic Devices. *Accounts of Chemical Research*, 35(7):491–499, 2002.

[35] Y. N. Xia and G. M. Whitesides. Soft lithography. *Annual Review Of Materials Science*, 37(5):551–575, 1998.

[36] David C. Duffy, J. Cooper McDonald, Olivier J. A. Schueller, and George M. Whitesides. Rapid prototyping of microfluidic systems in poly(dimethylsiloxane). *Analytical Chemistry*, 70(23):4974–4984, 1998.

[37] David A. Chang-Yen, Richard K. Eich, and Bruce K. Gale. A monolithic PDMS waveguide system fabricated using soft-lithography techniques. *Journal of Lightwave Technology*, 23(6):2088–2093, 2005.

[38] Diogo Lopes. Femtosecond laser direct writing: Fabrication and characterization of waveguides and gratings. *Master's thesis*, 2014.

[39] R. Osellame, H. J. W. M. Hoekstra, G. Cerullo, and M. Pollnau. Femtosecond laser microstructuring: An enabling tool for optofluidic lab-on-chips. *Laser and Photonics Reviews*, 5(3):442–463, 2011.

[40] Rod Taylor, Cyril Hnatovsky, and Eli Simova. Applications of femtosecond laser induced self-organized planar nanocracks inside fused silica glass. *Laser and Photonics Reviews*, 2(1-2):26–46, 2008.

[41] Yan Li, Kazuyoshi Itoh, Wataru Watanabe, Kazuhiro Yamada, Daisuke Kuroda, Junji Nishii, and Yongyuan Jiang. Three-dimensional hole drilling of silica glass from the rear surface with femtosecond laser pulses. *Optics Letters*, 26(23):1912–1914, 2001.

[42] Costantino Corbari, Audrey Champion, Mindaugas Gecevicius, Martynas Beresna, Yves Bellouard, and Peter G. Kazansky. Femtosecond versus picosecond laser machining of nano-gratings and micro-channels in silica glass. *Optics Express*, 21(4), 2013.

[43] Ali A. Said, Mark Dugan, Philippe Bado, Yves Bellouard, Andrew Scott, and Jose R. Mabesa Jr. Manufacturing by laser direct-write of three-dimensional devices containing optical and microfluidic networks. *Proceedings of SPIE*, 5339:194–204, 2004.

[44] A. Agarwal and M. Tomozawa. Correlation of silica glass properties with the infrared spectra. *Journal of Non-Crystalline Solids*, 209(1-2):166–174, 1997.

[45] C. Hnatovsky, R. S. Taylor, E. Simova, V. R. Bhardwaj, D. M. Rayner, and P. B. Corkum. Polarization-selective etching in femtosecond laser-assisted microfluidic channel fabrication in fused silica. *Optics Letters*, 30(14):1867–1869, 2005.

[46] K. R. Williams and R. S. Muller. Etch Rates for Micromachining Processing. *Journal of Microelectromechanical Systems*, 7157(December), 1996.

[47] Satoshi Kiyama, Shigeki Matsuo, Shuichi Hashimoto, and Yasushi Morihira. Examination of etching agent and etching mechanism on femotosecond laser microfabrication of channels inside vitreous silica substrates. *Journal of Physical Chemistry C*, 113(27):11560–11566, 2009.

[48] P. D. Fuqua, D. P. Taylor, H. Helvajian, W. W. Hansen, and M. H. Abraham. A UV direct-write approach for formation of embedded structures in photostructurable glassceramics. *Materials Research Society Symposium - Proceedings*, 624:79–86, 2000.

[49] Kwang Sup Lee, Ran Hee Kim, Dong Yol Yang, and Sang Hu Park. Advances in 3D nano/microfabrication using two-photon initiated polymerization. *Progress in Polymer Science (Oxford)*, 33(6):631–681, 2008.

[50] Kwang Sup Lee, Dong Yol Yang, Sang Hu Park, and Ran Hee Kim. Recent developments in the use of two-photon polymerization in precise 2D and 3D microfabrications. *Polymers for Advanced Technologies*, 17(2):72–82, 2006.

[51] Sang Hu Park, Dong Yol Yang, and Kwang Sup Lee. Two-photon stereolithography for realizing ultraprecise three-dimensional nano/microdevices. *Laser and Photonics Reviews*, 3(1-2):1–11, 2009.

[52] Mangirdas Malinauskas, Albertas Zukauskas, Vytautas Purlys, Kastytis Belazaras, Andrej Momot, Domas Paipulas, Roaldas Gadonas, Algis Piskarskas, Holger Gilbergs, Arune Gaidukeviciute, Ioanna Sakellari, Maria Farsari, and Saulius Juodkazis. Femtosecond laser polymerization of hybrid/integrated micro-optical elements and their characterization. *Journal of Optics*, 12(12):124010, 2010.

[53] Safi Jradi, Olivier Soppera, Daniel J. Lougnot, Renaud Bachelot, and Pascal Royer. Tailoring the geometry of polymer tips on the end of optical fibers via control of physicochemical parameters. *Optical Materials*, 31(4):640–646, 2009.

[54] Yan Li and Shiliang Qu. Water-assisted femtosecond laser ablation for fabricating threedimensional microfluidic chips. *Current Applied Physics*, 13(7):1292–1295, 2013.

[55] A. Dostovalov, S. Babin, M. Dubov, M. Baregheh, and V. Mezentsev. Comparative numerical study of energy deposition in femtosecond laser microfabrication with fundamental and second harmonics of Yb-doped laser. *Laser Physics*, 22(5):930–936, 2012.

[56] Yves Bellouard, Ali A. Said, Mark Dugan, and Philippe Bado. Investigation of Femtosecond Laser Irradiation on Fused Silica Etching Selectivity. *MRS Online Proceedings Library*, 850, 2004.

[57] Valeria Maselli, Roberto Osellame, Giulio Cerullo, Roberta Ramponi, Paolo Laporta, Luca Magagnin, and Pietro Luigi Cavallotti. Fabrication of long microchannels with circular cross section using astigmatically shaped femtosecond laser pulses and chemical etching. *Applied Physics Letters*, 88(19):86–89, 2006.

[58] Yves Bellouard, Ali Said, Mark Dugan, and Philippe Bado. Fabrication of high-aspect ratio, micro-fluidic channels and tunnels using femtosecond laser pulses and chemical etching. *Optics Express*, 12(10):2120, 2004.

[59] Francesca Bragheri, Lorenzo Ferrara, Nicola Bellini, Krishna C. Vishnubhatla, Paolo Minzioni, Roberta Ramponi, Roberto Osellame, and Ilaria Cristiani. Optofluidic chip for single cell trapping and stretching fabricated by a femtosecond laser. *Journal of Biophotonics*, 3(4):234–243, 2010.

[60] Lingling Qiao, Fei He, Chen Wang, Ya Cheng, Koji Sugioka, and Katsumi Midorikawa. A microfluidic chip integrated with a microoptical lens fabricated by femtosecond laser micromachining. *Applied Physics A: Materials Science and Processing*, 102(1):179– 183, 2011.

[61] Fei He, Ya Cheng, Zhizhan Xu, Yang Liao, Jian Xu, Haiyi Sun, Chen Wang, Zenghui Zhou, Koji Sugioka, Katsumi Midorikawa, Yonghao Xu, and Xianfeng Chen. Direct fabrication of homogeneous microfluidic channels embedded in fused silica using a femtosecond laser. *Optics Letters*, 35(3):282–284, 2010.

[62] Kazunari Tada, Gregory A. Cohoon, Khanh Kieu, Masud Mansuripur, and Robert A. Norwood. Fabrication of High-Q Microresonators by Femtosecond Laser Micromachining of Optical Fiber. *Photonics Technology Letters*, 25(5):430, 2013.

[63] Govind P. Agrawal. Fiber-Optic Communications Systems. *John Wiley & Sons*, 3 edition, 2002.

[64] Vítor Amorim. Fabrication of Integrated Optical Devices in Fused Silica by Femtosecond Laser Direct Writing. *Master's thesis*, *University of Porto*, 2016.

[65] Yuksel Temiz, Robert D. Lovchik, Govind V. Kaigala, and Emmanuel Delamarche. Lab-on-a-chip devices: How to close and plug the lab? *Microelectronic Engineering*, 132:156–175, 2015.

[66] M. J. Wild, A. Gillner, and R. Poprawe. Locally selective bonding of silicon and glass with laser. *Sensors and Actuators, A: Physical*, 93(1):63–69, 2001.

[67] Martin Hermans, Jens Gottmann, and Frank Riedel. Selective, laser-induced etching of fused silica at high scan-speeds using KOH. *Journal of Laser Micro/Nanoengineering*, 9(2):126–131, 2014.

[68] Y. Sikorski, C. Rablau, M. Dugan, Ali A. Said, P. Bado, and L. G. Beholz. Fabrication and characterization of microstructures with optical quality surfaces in fused silica glass using femtosecond laser pulses and chemical etching. *Applied Optics*, 45(28):7519– 7523, 2006.

[69] Audrey Champion, Martynas Beresna, Peter Kazansky, and Yves Bellouard. Stress distribution around femtosecond laser affected zones: effect of nanogratings orientation. *Optics express*, 21(21):24942–51, 2013.

[70] Krishna Chaitanya Vishnubhatla, Nicola Bellini, Roberta Ramponi, Giulio Cerullo, and Roberto Osellame. Shape control of microchannels fabricated in fused silica by femtosecond laser irradiation and chemical etching. *Optics Express*, 17(10):8685–8695, 2009.

[71] Valeria Maselli, Jason R. Grenier, Stephen Ho, and Peter R. Herman. Femtosecond laser written optofluidic sensor: Bragg grating waveguide evanescent probing of microfluidic channel. *Optics Express*, 17(14), 2009.

[72] Moosung Kim, David J. Hwang, Hojeong Jeon, Kuniaki Hiromatsu, and Costas P. Grigoropoulos. Single cell detection using a glass-based optofluidic device fabricated by femtosecond laser pulses. *Lab on a chip*, 9(2):311–8, 2009.

[73] R. Kashyap. Fiber Bragg Gratings. *Elsevier*, 2nd edition, 2010.

[74] K. Okamoto. Fundamentals of Optical Waveguides. *Elsevier*, 2nd edition, 2006.

[75] Robert Blue and Deepak Uttamchandani. Recent advances in optical fiber devices for microfluidics integration. *Journal of Biophotonics*, 9(1-2):13–25, 2016.

[76] Moez Haque, Kenneth K. C. Lee, Stephen Ho, Luís A. Fernandes, and Peter R. Herman. Chemical-assisted femtosecond laser writing of lab-in-fibers. *Lab on a chip*, 14(19):3817–29, 2014.

[77] Chengbo Mou, Kaiming Zhou, Edward Davies, Lin Zhang, and Ian Bennion. Fiber laser incorporating an intracavity microchannel for refractive index and temperature sensing. *IEEE Photonics Technology Letters*, 21(20):1559–1561, 2009.

[78] Christopher J. Tuck, Richard Hague, and Crispin Doyle. Low cost optical fibre based Fabry-Perot strain sensor production. *Measurement Science and Technology*, 17(8):2206, 2006.

[79] C. R. Liao, T. Y. Hu, and D. N. Wang. Optical fiber Fabry-Perot interferometer cavity fabricated by femtosecond laser micromachining and fusion splicing for refractive index sensing. *Optics Express*, 20(20):22813, 2012.